A numerical approach into new designs for SPR sensors in D-type optical fibers

DOCTORAL THESIS

Diego Felipe De Nóbrega Dos Santos
DOCTORATE IN AUTOMATION AND INSTRUMENTATION

UNIVERSIDADE da MADEIRA
A Nossa Universidade
www.uma.pt

July | 2017

FCT Fundação para a Ciência e a Tecnologia
MINISTÉRIO DA EDUCAÇÃO E CIÊNCIA

A numerical approach into new designs for SPR sensors in D-type optical fibers

DOCTORAL THESIS

Diego Felipe De Nóbrega Dos Santos
DOCTORATE IN AUTOMATION AND INSTRUMENTATION

SUPERVISOR
José Manuel Rocha Teixeira Baptista

CO-SUPERVISOR
Ariel Ricardo Negrão Silva Guerreiro

Acknowledgements

First, I am thankful to Prof. Dr. José Manuel Baptista and Prof. Dr. Ariel Guerreiro, for supervising me in the past years during my Ph.D. thesis. José Manuel had always asked for new scientific possibilities and looking for error in the results making me to understand completely the results, before continuing to other problems. Ariel gave me a lot advice about the simulation, how to solve the problems and suggesting from time to time a crazy idea.

Also, I am thankful to all the group of the department of physics of the University of Madeira in special to Prof. Dr. Pedro Almeida and Prof. Dr. Mikhail Benilov for advice about COMSOL Multiphysics and show me that there are more than SPR sensors in optical fibers.

I am also thankful to Prof. Dr. Markus Schmidt, Prof. Dr Kay Schuster and Prof. Dr. Patrick Uebel, that welcomed in Institute for Photonic Technology (IPHT) and let me understand the theoretical and experimental physics difficulties of working with optical fibers.

I also would like to thank to Dr. Nunzio Cennamo and Prof. Dr. Luigi Zeni from the Second University of Naples and Dr. Luis Coelho and Dr. Pedro A. S. Jorge from Institute for Systems and Computer Engineering, Technology and Science (INESC-TEC former INESCPorto) for allowing me to validate the experimental and theoretical results.

To the University of Madeira and to INESC-TEC friends, teachers and staff for the companionship and professionalism shown over the years.

I also like to acknowledge the Portuguese funding institution (FCT - Fundação para a Ciência e a Tecnologia) for supporting their program under Grant SFRH/BD/85068/2012.

Finally, I thank all my family, for understanding, for caring, for motivation and for being always present.

Abstract

This thesis investigates how to improve the performance of current designs of optical fiber sensors based on Surface Plasmon Resonance, and how to use a better understanding of the physical and sensing principles behind them to propose new sensing concepts and ideas. We adopt a methodology based on numerical simulations because they provide a better insight onto the operation of these sensors and because they allow an easy and quick way of testing new designs and concepts without the need to fabricate the sensors. We also show that these simulations have a good agreement with experimental results.

We adopt a systematic approach to investigate the various parameters that influence the sensor performance, and present different sensors designs, where we study the localization, optical properties, shape and size of the metal components, combined with different type of fibers, resulting in the coupling between the plasmon and optical modes. Furthermore, we verify that choosing the optical modes used in sensing in multimode fibers can also have advantages. We investigate the use of modern artificial materials, such as metamaterials, as well as the inclusion of multiple wires in the fiber to enhance the performance of the SPR sensor. At a more fundamental level, we show that the control of the coupling between multiple plasmon modes in metal components and the optical modes in the fiber constitutes a new way to improve the performance of the sensor and can be inclusively used to develop a new type of SPR sensors capable of measuring simultaneously two variables, such as the external refractive index and temperature

Keywords: Optical fiber sensor, Surface plasmon resonance, Numerical simulation, Metamaterials, Nanoplasmonics, Multiparameter sensing

Resumo

Esta tese investiga como é possível melhorar o desempenho das estruturas atuais dos sensores de fibra ótica baseados em Ressonância Plasmónica de Superfície (SPR), bem como compreender melhor os princípios físicos e de sensorização na base do seu funcionamento, permitindo propor novos conceitos de sensores. Foi utilizada uma metodologia baseada em simulações numéricas, pois proporcionam um melhor entendimento do funcionamento desses sensores, constituindo uma maneira simples e rápida de testar novas estruturas e conceitos, sem a necessidade de fabricar os sensores. Mostra-se também que essas simulações têm uma boa concordância com os resultados experimentais.

Foi adotada uma abordagem em que se investiga sistematicamente os diversos parâmetros que influenciam o desempenho do sensor e se apresentam diferentes estruturas de sensores onde foram estudadas a localização, propriedades óticas, forma e tamanho dos componentes metálicos, combinados com diferentes tipos de fibras, resultando no acoplamento entre os modos plasmónicos e os modos óticos. Também foi verificado que a escolha dos modos óticos utilizados na deteção em fibras multimodo pode apresentar vantagens. Foi investigado ainda o uso de materiais artificiais recentemente desenvolvidos, de que são exemplo os metamateriais, bem como, a inclusão de múltiplos fios metálicos na fibra, de forma a melhorar o desempenho dos sensores SPR. A um nível mais fundamental, foi demonstrado que o controlo do acoplamento entre os múltiplos modos plasmónicos gerados nos componentes metálicos e os modos óticos propagados na fibra constitui uma nova forma de melhorar o desempenho do sensor. Tal pode ser inclusivamente utilizado para desenvolver um novo tipo de sensores SPR capazes de medir simultaneamente duas variáveis, como por exemplo o índice de refração externo e a temperatura.

Palavras chave: Sensores de fibra ótica, Ressonância plasmónica de superfície, Simulação numérica, Meta-materiais, Nano-plasmões, deteção multi-parâmetro

Resumen

Esta tesis investiga cómo es posible mejorar el desempeño de los diseños actuales de sensores de fibra óptica basados en la Resonancia Plasmónica de Superficie (SPR) y permitir un mejor entendimiento de los principios físicos y sensores que luego permitirá proponer nuevos conceptos e ideas. Fue utilizada una metodología basada en simulaciones numéricas, ya que esta proporciona una mejor comprensión sobre el funcionamiento de estos sensores y porque permiten una manera simple y rápida de probar nuevos diseños y conceptos sin necesidad de fabricar los sensores. También fue verificado que estas simulaciones son una buena aproximación a los resultados experimentales.

Se adoptó un enfoque sistemático para investigar los diversos parámetros que influyen en el desempeño del sensor y se presentan diferentes diseños de sensores, donde estudiamos la localización, las propiedades ópticas, la forma y el tamaño de los componentes metálicos, combinados con diferentes tipos de fibras, resultando en el acoplamiento entre los modos plasmónicos y los modos ópticos. También se verifico que la elección de los modos ópticos utilizados en la detección en fibras multimodo ofrece otras ventajas. Fue investigado el uso de materiales artificiales recientemente desenvuelto, como son los metamateriales, así como la inclusión de múltiples hilos de metal en la fibra óptica para mejorar el rendimiento del sensor SPR. En un nivel más fundamental, se demuestra que el control del acoplamiento entre múltiples modos plasmónicos criados por la componente metálica y los modos ópticos en la fibra constituye es una nueva forma de mejorar el rendimiento del sensor. Esto incluso se puede utilizar para desarrollar un nuevo tipo de sensores basados en SPR capaces de medir simultáneamente dos variables, tales como el índice de refracción externa y la temperatura.

Palabras clave: Sensores de fibra óptica, Resonancia plasmónica de superficie, Simulación numérica, Metamateriales, Nano-plasmones, Detección de multiparámetros.

Contents

Contents

Contents

List of Figures

List of Figures

List of Tables

Publications in Refereed Journals and Conferences

Journals

1 D. Santos, A. Guerreiro and J. M. Baptista, "SPR Microstructured D-Type Optical Fiber Sensor Configuration for Refractive Index Measurement", IEEE Sensors Journal, 5472 – 5477, 15 (2015). DOI: 10.1109/JSEN.2015.2442335

2 N. Cennamo, L. Coelho, D. F. Santos, J. M. Baptista, A. Guerreiro, P. A. S. Jorge and L. Zeni, "Modal Filtering for Optimized Surface Plasmon Resonance Sensing in Multimode Plastic Optical Fibers", IEEE Sensors Journal, 6306-6312, 15 (2015). DOI: 10.1109/JSEN.2015.2450991

3 D. Santos, A. Guerreiro and J. M. Baptista. "SPR optimization using metamaterials in a D-type PCF refractive index sensor", Optical Fiber Technology, 83-88, 33 (2017) DOI: 10.1016/j.yofte.2016.11.010.

4 D. Santos, A. Guerreiro and J. M. Baptista. "Surface plasmon resonance sensor based on D-type fiber with a gold wire", Optik - International Journal for Light and Electron Optics, 244-249, 139 (2017) DOI: 10.1016/j.ijleo.2017.03.035.

5 D. Santos, A. Guerreiro and J. M. Baptista. "Simultaneous plasmonic measurement of refractive index and temperature based on a D-type fiber sensor with gold wires", IEEE Sensors Journal, 2439-2446, 17 (2017) DOI: 10.1109/JSEN.2017.2674522.

Conference Proceedings

1 D. Santos, A. Guerreiro and J. M. Baptista, "Performance analysis simulation of new SPR microstructured D-type optical fiber sensor configurations for refractive index measurement", 23rd International Conference on Optical Fibre Sensors, 1-4, 91579O (2014).

2 D. Santos, A. Guerreiro and J. M. Baptista, "New SPR PCF D-type optical fiber sensor configuration for refractive index", 24th International Conference on Optical Fibre Sensors, 1-4, 96346 (2015).

3 D. Santos, A. Guerreiro and J. M. Baptista, "Optimization of modal sensitivity in nanowire SPR multimode sensor", 25th International Conference on Optical Fibre Sensors, accepted (2017).

4 D. Santos, A. Guerreiro and J. M. Baptista, "SPR based PCF D-type sensor based on a metamaterial composed of planar metals for refractive index sensing", 6th European Workshop on Optical Fibre Sensors, 1-4, 991619 (2016).

Chapter 1 Introduction and motivation

Sensors are a technology component that play a critical role in the modern world in improving the quality of life, either as part of information and monitoring systems or integrated in different types of devices. They are found in applications ranging from infrastructure and industrial monitoring to environmental control, among others. Indeed they can be found measuring many distinct parameters, from pH, temperature, humidity, pressure and voltage, to refractive index, carbon dioxide (CO_2) concentration and many other physical, chemical and biological parameters. The use of sensors is today generalized, and they play a crucial role in obtaining relevant information.

In particular, fiber optic sensors have the advantage of allowing their integration in vast numbers in the existing network of optical fibers, an infrastructure that covers almost the entire world. Due to their intrinsic characteristics, a single optical fiber can support a high number of sensors, operating remotely and having immunity to electromagnetic and radiofrequency interference [1]. In addition to some external refractive index detection fiber optic systems already available commercially, there has been considerable scientific interest in the technology of surface plasmon resonance (SPR), sensors associated with photonic crystal fiber (PCF), nanoscale structures and metamaterials. This new type of sensors, based on micro-layers of material deposited on nano- and micro-structured fibers, have been attracting the attention of researchers [2].

The operation of surface plasmon resonance sensors as bio sensing has been demonstrated by Liedberg *et al.* [3] in 1983. In his study, the authors used a practical and commonly used method to excite surface plasma, which was originally suggested by Kretschmann in 1971. It is a method in which light propagates through a prism in the configuration of attenuated total reflection (ATR), depositing a metal film by evaporation at the base of this prism [4].

In 1993, Jorgenson and Yee [5] constructed the first fiber-based SPR sensor. This work demonstrated that the optical fiber can replace the prism, in the configuration of Kretschmann, allowing also generate the resonance of surface plasmons. The fiber used was chemically treated to remove almost the entire sheath and thereby increased the sensitivity of the sensor. This type of fiber optic sensor based on SPR is able to present a very high sensitivity to the refractive index, a short response time and still have all the advantages of using optical fiber [6].

SPR sensors in optical fibers have a large variety of classification, depending on: the type of fiber, the geometry of the sensor, the number, form and size of the

coatings, the excitation techniques, the detection or interrogation method and the application.

The performance enhancement of SPR sensors is focused on improving the operating wavelength range, refractive index detection range, sensitivity, and resolution, to obtain the best configuration SPR sensor for a given application. Due to the different types of SPR sensors, their actual construction and testing is very expensive and time consuming, making simulation programs important tools to obtain a first and fast approximation of the behavior of the final sensor. These tools should allow analyzing parameters such as: the intensity of the electric and magnetic field, the effective index of refraction, among others, permitting to innovate SPR sensors and understand phenomena not previously observed.

There are several difficulties to develop a good simulation program, including those found when writing the code for 2D and 3D designs [1]. When the structure of the sensor is too complex, the calculations become rather elaborate, being necessary to use more simplified numerical analysis methods such as: the expansion and propagation method (MEP) [7], the method for multilayer structure transfer matrix modeling [8], the optical fiber multilayer cylindrical structure [9] and the rigorous couple wave analysis (RCWA) [10]. However, these methods have some limitations in analyzing structures with nanostructured irregularities [11]. The finite-difference time domain (FDTD) method and the finite element method (FEM) allow calculate the electric and magnetic fields in these structures, but require high computational memory capacities [12]. Therefore, it is a challenge to work with this type of structures.

1.1 Motivation

One of the main reasons for this thesis was the need to have tools to simulate the behavior of SPR fiber sensors for the measurement of external refractive index. Due to the different types of optical fibers and sensor configurations associated with SPR, their actual construction and testing is very expensive and time consuming, making simulation programs important tools to obtain a first and fast approximation of the behavior of the final sensor. With such a tool, it is possible to solve problems that arise during the study and at the same time optimize the project to be carried out. The possibility of having a single tool to simulate the performance of fiber optic sensors was the objective in this thesis in the field of optical fiber sensors based on SPR.

The work of this thesis is therefore motivated by the following questions:

- Is this simulation approach effective in modelling different SPR D-Type fiber configurations?
- How do the results of the simulations compare with the experimental data?
- How can we engineer the interactions between light and plasmons to improve sensing performance?
- What kind of microstructures and new materials can be incorporated in the sensors to help boost sensing performance?
- Can we integrate the characteristics of different SPR sensors measuring distinct quantities in a single sensor?

The main objective of this thesis is the numerical simulation analysis of new SPR sensor configurations using the same simulation tool, focusing on the optimization of different parameters in SPR sensors (see chapter 4-9). Therefore, we compare the numerical results with experimental results (see chapter 5). We study the effect of replacing a conventional film metal with a metamaterial (see chapter 6). We proposed an SPR sensor based in wires where a single and multimode fibers are used (see chapters 7-8). And finally, we propose and analyze an SPR sensor configuration for the simultaneous measurement of the external refractive index and the temperature (see chapter 9).

1.2 Supporting Research collaborations

The realization of this Ph.D. thesis included periods as visiting researcher and collaborations with several institutions: University of Porto, Portugal, Institute for Photonic Technology, in Jena, Germany, Second University of Naples, Italy, and the host institutions, the Institute for Systems and Computer Engineering, Technology and Science (INESC-TEC former INESCPorto) and the University of Madeira. Each of these periods had a direct impact in one or more chapters of this thesis, as well as, the publication of different scientific articles.

In particular, the period between the 2nd and 3rd year was spent at the Institute for Photonic Technology (IPHT), under the local supervision of Dr. Kay Schuster and Prof. Markus A. Schmidt, investigating the interaction between light, plasmonic and high refractive index microstructures in optical fibers.

Another collaboration included Prof. Dr. Luigi Zeni, Dr. Nunzio Cennamo (from the University of Naples), and Dr. Pedro Jorge and Dr. Luis Coelho (from INESC-TEC), and resulted in a study of multimode optical fiber sensor, discussed in chapter 5.

1.3 Structure of the thesis

This thesis is organized in ten chapters, including this introduction. In the second chapter a definition of SPR is presented, a current state of the art of the SPR sensor configurations found in literature and how the SPR sensors can be classified. In addition, we described the characteristics of an SPR sensor, completed in chapter three. In the third chapter, we describe Maxwell's equations and the wave equation to study the behavior of the electromagnetic wave (light) inside the optical fiber. We also study the optical properties of the materials used in this thesis and we analyze guided modes in planar and cylindrical structures.

Chapter 4 presents the conventional SPR D-type fiber sensor and we analyze the behavior of the different SPR sensor parameters. We also analyze and compare the SPR sensor based on a conventional D-type fiber and on a D-type photonics crystal fiber. From this chapter resulted two publications, one in a journal (1) and another one in a conference (1).

In Chapter 5 we study the modal effects on a SPR D-type plastic optical fiber comprehending a theoretical and an experimental part. A journal paper was published in conjunction with the University of Naples and the University of Porto (2).

In Chapter 6 we address an SPR D-type PCF with a metamaterial and we propose a method to manufacture a SPR fiber sensor with a metamaterial with specific characteristics. Two publications resulted from this chapter, one in a journal (3) and another one in a conference (2).

In Chapter 7 and 8 we study a SPR D-type with two different types of fiber, singlemode and multimode, respectively, where we study the effects of the multiple modes that propagate in the fiber and in the metal. From this chapter resulted three publications, one in journal (**Erro! A origem da referência não foi encontrada.**) and another two in conferences (3 and 4).

Chapter 9 proposes a sensor with simultaneous measurement of the refractive index and temperature. Another journal paper was published (4).

Finally, in chapter 10 we summarize the work performed and highlight the main conclusions of the thesis.

Chapter 2 State of the art

The phenomenon of surface plasmon resonance (SPR) has been studied since the beginning of the 20th century, and since then the basic principles of operation of SPR have become well known. The quantity of work in literature about SPR sensors is so large that any review is necessarily incomplete, therefore, in this chapter we shall focus on the main results relevant to the central problem of this dissertation.

In this chapter, we explore the nature of surface plasmons and the different ways to excite optically surface plasmons, starting with the prism configurations by Otto and Kretschmann, and then moving into other configurations in different types of optical fibers, such as cladding-off fiber, D-type fiber, microstructured fiber, plastic optical fiber, among others. We also describe how SPR sensors are classified and characterized. The large quantities of configurations found in literature justify the need to have a simulation tool that is able to completely understand, optimize and choose the more appropriated SPR sensor.

2.1 What are Surface Plasmons

Surface plasmons are excitons that are sometimes described as a type of polaritons, resulting from a strong coupling of the electromagnetic waves that propagate along the boundary between a dielectric medium and a metal, with the oscillations of the density of free electrons in the metal. Plasmons are strongly affected by electric resistance and other dissipative processes in the materials and typically have short propagation lengths after which they decay rapidly. At certain optical wavelengths, electromagnetic waves can couple resonantly with the plasmons resulting in an enhancement of the optical loss. This mechanism translates into a strong reduction of transmission power of light for certain wavelengths in optical waveguides coated with metals. The conditions of occurrence of this resonance can be affected by the optical properties of the media surrounding the metal, namely the refractive index of the medium in the exterior of the fibre, which causes several optical parameters (such as the resonant wavelength and the level of loss) to change. This principle is the corner stone of most of the SPR based sensors in optical fibres.

2.2 Optical Excitation of Surface Plasmon

A light wave can couple to a surface plasmon at a metal-dielectric interface if the component of light's waveguide is parallel to the interface and matches the propagation constant of the surface plasmon. The most common couplers used in SPR sensors include a prism coupler, a grating coupler , and a waveguide coupler, as shown in Figure 2.1a, Figure 2.1b and Figure 2.2, respectively [13].

The phenomena of surface plasmon resonance has been studied since the beginning of the 20th century, although the greatest progress on SPR was achieved in the late 60s with the development of bulk configurations [14], [15]. The first two bulk configurations are the Otto [14], (dielectric-metal interface) and the Kretschmann [15] (metal-dielectric interface), as shown in Figure 2.1a and Figure 2.1b, respectively. The first SPR sensor based on a light prism was developed in 1983 by Liedberg *et al.* [3]. Another SPR configuration based on a prism uses a corrugated interface to form a grating coupler, as shown in Figure 2.2 [16]. Nowadays SPR sensors are the most sensitive optical refractometric configurations.

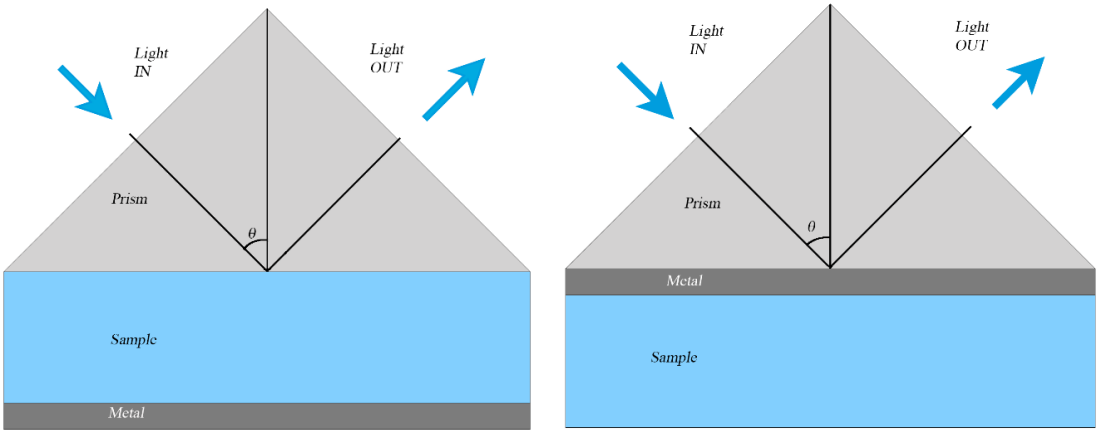

(a) (b)

Figure 2.1 Basic schemes for SPR sensors with (a) Otto configuration based coupling; (b) Kretschmann configuration based coupling.

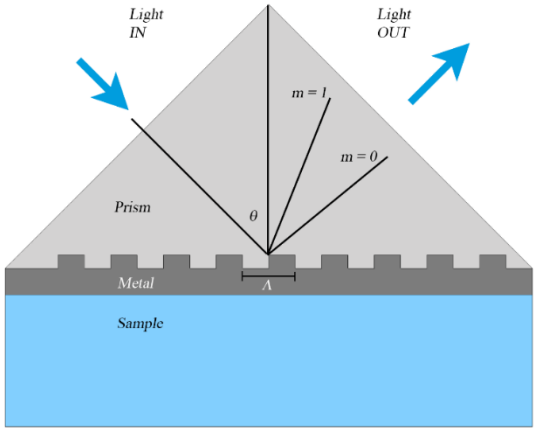

Figure 2.2 Basic scheme for SPR sensors with grating coupling.

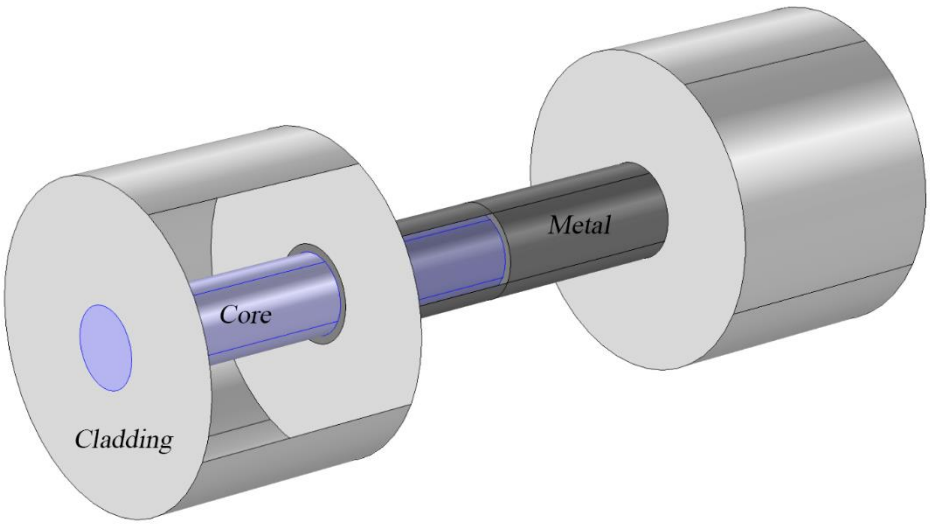

Figure 2.3 Configuration of SPR sensor using an optical fiber where the fiber cladding is removed (cladding-off fiber).

Optical fiber sensors are also a very interesting solution for environmental monitoring, due to their intrinsic characteristics such as high sensor count multiplexing, remote sensing, miniaturization capability and immunity to electromagnetic and radiofrequency interferences [1]. The first configuration of a SPR sensor in an optical fiber was first proposed in 1990 [17], but only Jorgenson and Yee in 1993 [5] fabricated the first optical fiber SPR sensor. In this work, SPR in an optical fiber was generated by removing the fiber cladding (cladding-off fiber), where a metal layer was deposited, allowing the excitation of the SPR, as shown in Figure 2.3.

2.3 Evaluation of the performance of the SPR sensors

The performance of an SPR sensor is evaluated based on certain characteristic properties, such as sensitivity, resolution, linearity, accuracy, reproducibility, dynamic range and limit of detection [18]. Nevertheless, published works focus more on the sensitivity and resolution. In SPR sensors based in the prism configuration the focus is normally on the angular modulation or on the wavelength modulation, as shown in Figure 2.4. The resonance angle θ_{res} or the resonance wavelength λ_{res} is determined by the refractive index of the sensing medium. Thus, when the refractive index of the sensing medium is changed by δn, the resonant angle of the incidence light θ_{res} is changed by $\delta\theta$ or the resonant wavelength λ_{res} is changed by $\delta\lambda$, as shown in Figure 2.4 [19].

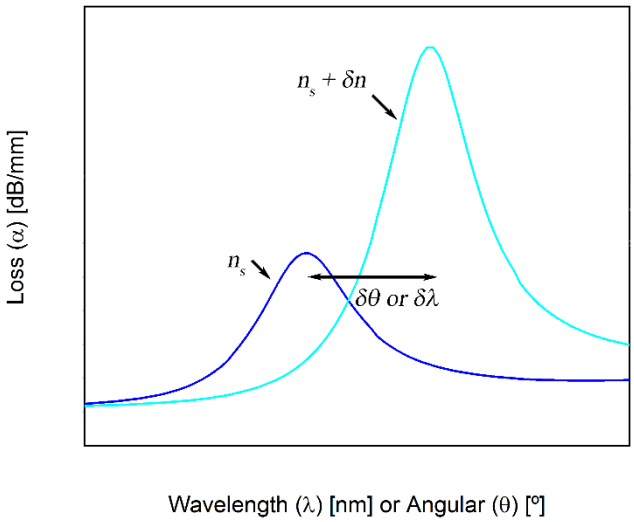

Figure 2.4 Attenuation of light due to SPR with angular modulation or wavelength modulation [2].

The variation of the δn can be observed trough the reflection (Figure 2.4), loss [20] or transmission. For example, Jorgenson and Yee [5] measured the variation of the transmission when some important parameters were changed (film thickness, film refractive index, external refractive index, waveguide refractive index). The sensitivity of an SPR sensor is defined as the ratio between the change in sensor output and the change in the quantity to be measured. Homola in [21] calculated the sensitivity of a SPR sensor using perturbation theory. This theory consists in studying the relation between the change in the propagation constant of the surface plasmon (SP) and the refractive index. In other work, the author uses another interrogation technique based on the optical excitation and interrogation of a surface plasmon, which consisted in the analysis of the state of polarization of the reflected wave in presence of the excited plasmon [22].

The resolution of a refractive index SPR sensor defines the smallest variation in the refractive index which produces a variation in the sensor output. This parameter of performance is related to the limit of detection and the intensity noise [19].

The sensitivity and the resolution of an SPR sensor is dependent on three parameters, according to Homola: the variation of the refractive index of the external medium; the method of excitation of the SPR and the modulation approach used in the SPR sensor.

2.4 SPR sensor classification

SPR sensor classification in literature depends on multiple parameters: the method of guiding the light (fiber or prism) and the respective material (different types of glass, like silica, BK7, among others and plastic), the geometry that allows the coupling between the surface plasmon and the waveguide, the structure of the metal on which depends the surface plasmon behavior, the method of surface plasmon excitation, the type of detection that permits the measurement of the refractive index, and finally the application the SPR sensor is used for. Figure 2.5 represents a flowchart where SPR sensor classification is represented, based in the model used by Klantsataya in [23].

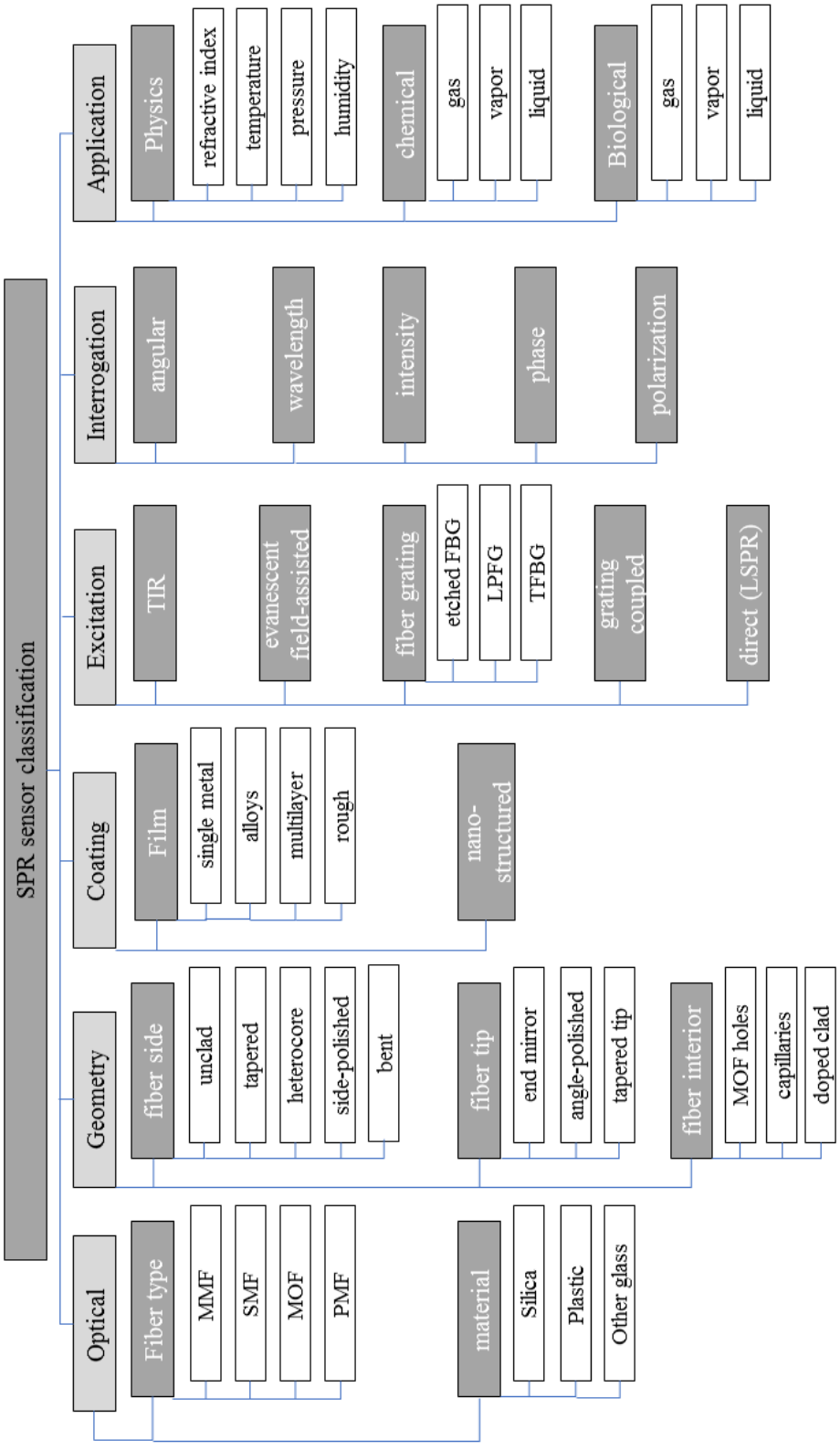

Figure 2.5 Classification of SPR fiber sensors. MMF: Multi Mode Fiber; SMF: Single Mode Fiber; MOF: Microstructured Optical Fiber; PMF: Polarization Maintaining Fiber; FBG: Fiber Bragg Grating, LPG: Long Period Fiber Grating; TFBG: Tilted Fiber Bragg Grating; LSPR: Localized Surface Plasmon Resonance [23].

2.4.1 Optical configurations

SPR sensors can be categorized by the type of optics (prism or fiber). The two first configurations of SPR prims sensors are based in the Otto [14] and Kretschmann [15] configurations. The appearance of the optical fiber permitted another method of propagation of the light, and at the same time the possibility of the creation of another kind of SPR sensor. The optical fiber can be: multimode fiber (MMF), singlemode fiber (SMF), microstructured optical fiber (MOF), polarization maintaining fiber (PMF), or multiple-core fiber.

The first SPR fiber sensor was made using a multimode fiber in which a part of the fiber was removed and then was placed the metal [5]. This configuration is one of the most common type used for SPR fiber sensors, due to the abundance and relative simplicity of sensor fabrication. The problem with this configuration is the large number of modes that propagate in the fiber, producing a lot of resonance modes and a lot of signal noise in the sensor, resulting in a decreased sensor performance. The use of a singlemode fiber is the solution for the problem of multiple modes that propagate in the fiber but, when part of the fiber is removed to place the metal, the SPR fiber sensor becomes extremely fragile.

The microstructured optical fiber (MOF) is another recent possibility in the creation of a SPR fiber sensor. The MOF D-type or D-shape is a simple sensor configuration used for fabrication of a SPR sensor [24]–[26]. Theoretically MOF SPR sensors are constructed with a different size, structure of the metal, localization of the metal, among other differences, when compared with SPR fiber sensors based on conventional optical fibers [27]–[29].

2.4.2 Interrogation of the SPR sensor

Although the sensing principle of SPR sensors is simple, several interrogation approaches have been applied in these sensors. Today SPR sensors can be classified based on the type of sensor interrogation:

SPR sensor with angular modulation: in this case the measurement is obtained by analyzing the angles of coupling incident light as function of the excitation of the surface plasmon. The angle of incident light that produces the strongest coupling is used as a sensor output [30], [31]. In this type of interrogation, the optimization of the sensing parameter is obtained by using the Fresnel's formulas and multiple-reflectance theory.

SPR sensor with wavelength modulation: for this type of classification many wavelengths are used to excite the surface plasmon and normally is measured the wavelength with the strongest coupling and used as a sensor output. In this case the angle of incident is the same and only the wavelength is changed [32]. This kind of modulation also permits multiplexing on wavelength using different materials or different sizes to change the resonance of the plasmon [33].

The most used sensors based in SPR are based on angular or on wavelength modulation [28], [34], [35].

SPR sensor with intensity modulation: in this case the wavelength and the angle of incident is kept constant and only the loss intensity is measured as function of the

light interaction with the surface plasmon. The loss intensity is used as a sensor output [36]. The advantages of this configuration is its simplicity and low cost, but it is necessary the complete control the wavelength resonance of the sensor which, is controlled by the materials that constitute the sensor [23]. Moreover, this interrogation scheme requires intensity referencing.

SPR sensor with phase modulation: in this case is used the phase of the light wave as the sensor output, being observed the interaction of the light with the surface plasmon as function of the light phase modulation [37]. The SPR sensor based in phase modulation has better resolution, but there are some difficulties to build high precision and real-time wave front phase detection [38], [39].

SPR sensor with polarization modulation: changes in the polarization of the light wave interacting with a surface plasmon are measured [40].

Finally, it is possible to combing two types of modulation, for example, phase modulation and polarization modulation, as proposed by Xiangliang in [41].

In this thesis, we considered SPR sensors with wavelength modulation because is relatively easy to interrogate, presents a good sensitivity and resolution, and does not require referencing [1].

2.4.3 Geometry design of the SPR fiber sensor

The geometry design of the SPR fiber sensor can be classified in three ways, depending on the localization of the metal with respect of the fiber:

Side fiber SPR sensor: In this case, the localization of the metal is on one side of the fiber. The metal cladding-off fiber (also denominated unclad fiber) was the first configuration to be studied for SPR sensors in an optical fiber, as shown in Figure 2.3 [5]. This configuration has been very studied with a good sensitivity when using MMFs, but with the noise problem. The metal cladding-off using SMF has a good sensitivity with low noise since only one mode is studied, but the fragility of the SPR sensor is increased. To solve this problem another configuration was proposed. In 1994 Bender *et al*. [42] demonstrated another configuration, the side-polished fiber. This sensing configuration is formed by an optical fiber where the cladding is polished, only on one face, where the metal is deposited. In this case the fiber is bent, as shown in Figure 2.6. This type of configuration demonstrated the same sensitivity, being more robust in comparison with the cladding-off SMF [43].

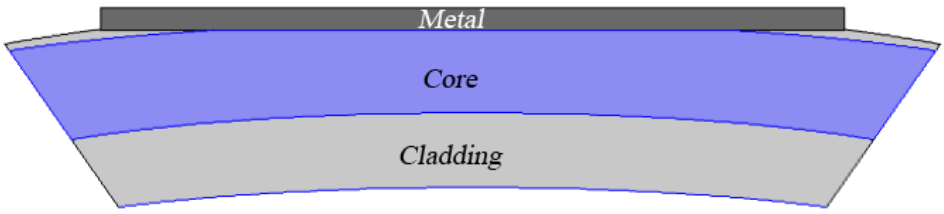

Figure 2.6 SPR fiber-optic sensor with a side-polished configuration.

The evolution and appearance of new fiber manufacturing techniques allowed the creation of the other SPR sensor designs like the D-type or D-shape fiber, as shown in Figure 2.7. The D-type fiber (without SPR) allowed to study the sensitivity of the external refractive index as function of the phase difference variation [44], and the

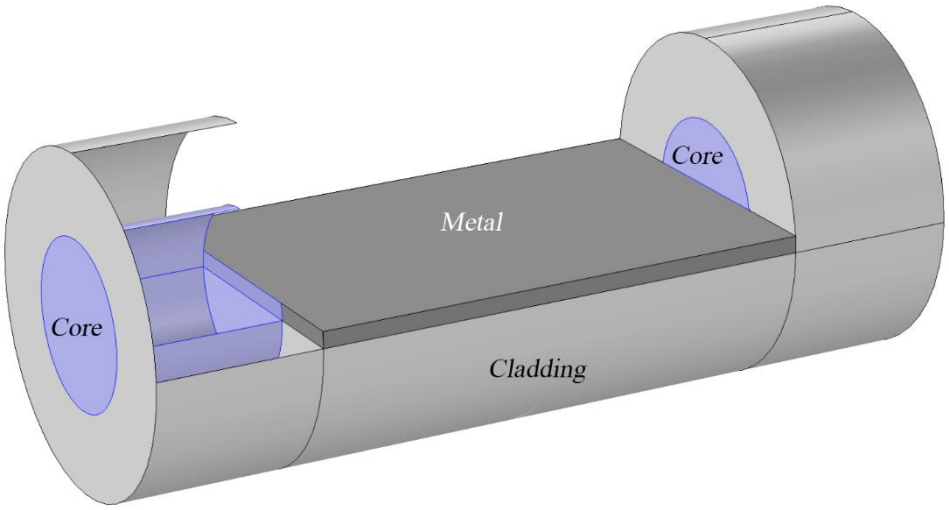

Figure 2.7 SPR fiber optic sensor with a D-shape or D-type fiber configuration.

combination with SPR technology, the sensitivity of the external refractive index is obtained using the wavelength [45], intensity [46] or phase variations [47] and with better results. This configuration is very used in the literature because of the robustness and availability of the fiber and can use other types of fiber, films, or metal configurations, like multimode plastic fiber [48], microstructured fiber [12], metamaterial films and metallic wires studied in this thesis.

Figure 2.8 shows different schematics of the SPR fiber optic sensor design. In 1997 Tubb *et al*. [49] used other configuration, a tapered fiber, as shown in Figure 2.8a. This type of configuration is able to generate multiple SPR wavelength peaks [50]. The SPR tapered fiber can reach high sensitivity (11800 nm/RIU) when combined with a

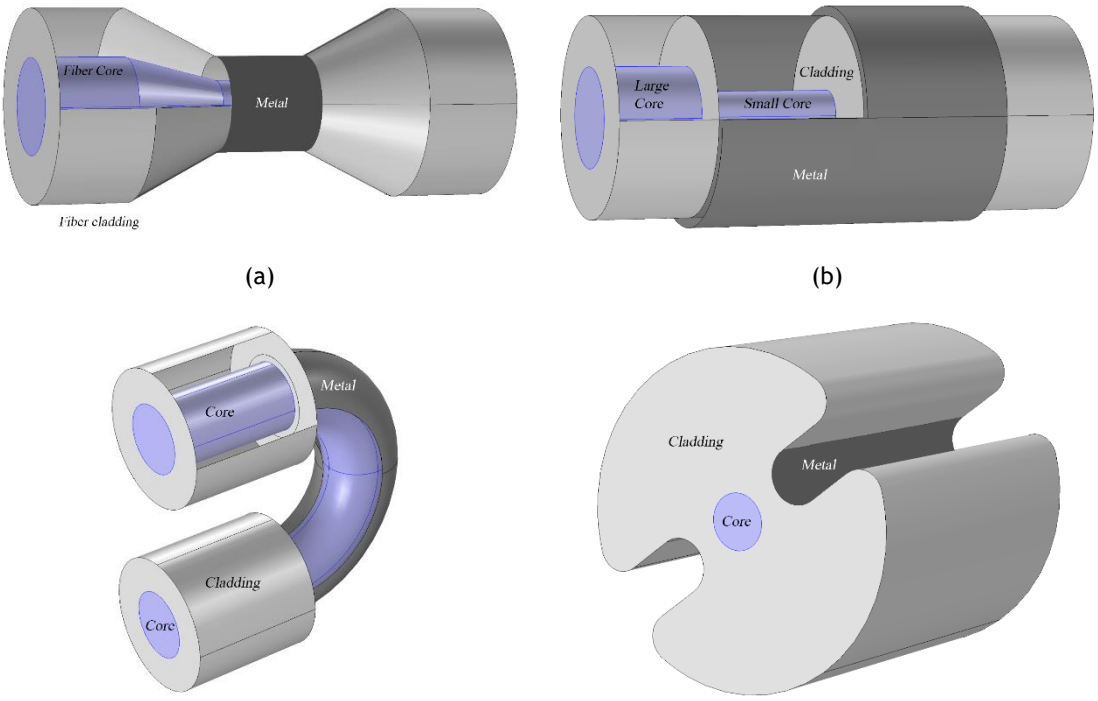

Figure 2.8 Schematics of the SPR fiber-optic sensor design with (a) tapered fiber; (b) hetero-core fiber; (c) U-shape fiber; d) H-shaper fiber.

high dielectric overlay like Indium Nitride [51], but again with the cost of an increased fragility of the SPR sensor.

There are more fiber configurations of the SPR sensor based in optical fibers: Hetero-core fiber, that consists in two fibers with different sizes of the cores (one large and one small). The main characteristic of this sensor is that the modes leak into the cladding layer and then the SPR occurs between the metal and the external medium. This can be used for the measurement of the variation of the refractive external medium (Figure 2.8b) [52]. U-shape fiber, like in the previous designs, the aim is to allow the modes to propagate in the cladding through the bend of the fiber, and replacing the cladding by the metal layer we can create SPR (Figure 2.8c) [34]. H-shape fiber design is a fiber where the cladding is partial removed, and replaced by a metal film, resulting in a fiber with the form of an "H", as shown in Figure 2.8d. In this fiber the modes that propagate in the core can couple into the plasmonic mode, similar to a D-type fiber [53].

Fiber tip SPR sensor: in this case the localization of the metal is at the end of the fiber. The schematic of the sensor is shown in Figure 2.9, and consists in an optical fiber where the end of the cladding is removed and then a thin film is deposited in the side of fiber. Finally in the tip of the fiber is deposited a mirror that reflects the wave and then interrogation is performed through analyzing light back-reflected from the mirrored fiber tip. The characteristics of the sensor are similar to the unclad sensor, but increase dips, because the wave travels two times in the metal [54].

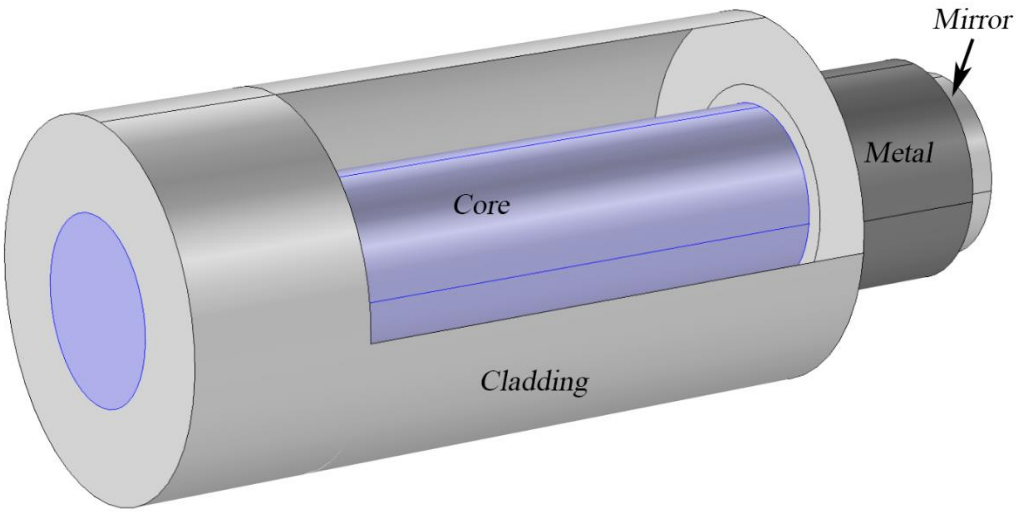

Figure 2.9 Schematic of an optical fiber SPR sensor implemented on the tip of an optical fiber with a mirror in the end.

Interior fiber SPR sensor: in this kind of design the metal is deposited in the interior of the fiber through the holes of a microstructured optical fiber, by the micro capillaries. Not only metal can be deposited inside of the fiber. In some configurations, can be use the MOF to deposit also the sample in the interior of the fiber. This new type of sensors, based on micro and nano material layers deposited on MOF, have also been attracting the attention of researchers [2]. The optical fiber community has been continuously engaged on research and development activity around these new fibers. Indeed, the fiber structure with a lattice of air holes running along its length shows remarkable properties that support a large variety of novel optical fiber devices, which

can be used both in communication and sensing systems. Some of the designs of SPR sensors found in literature are: MOF with crescent-shape holes, PCF with circular holes [55], MOF with three structured holes (also called wagon wheel fiber) [12] and microcapillary fiber SPR sensors [56], as shown in Figure 2.10.

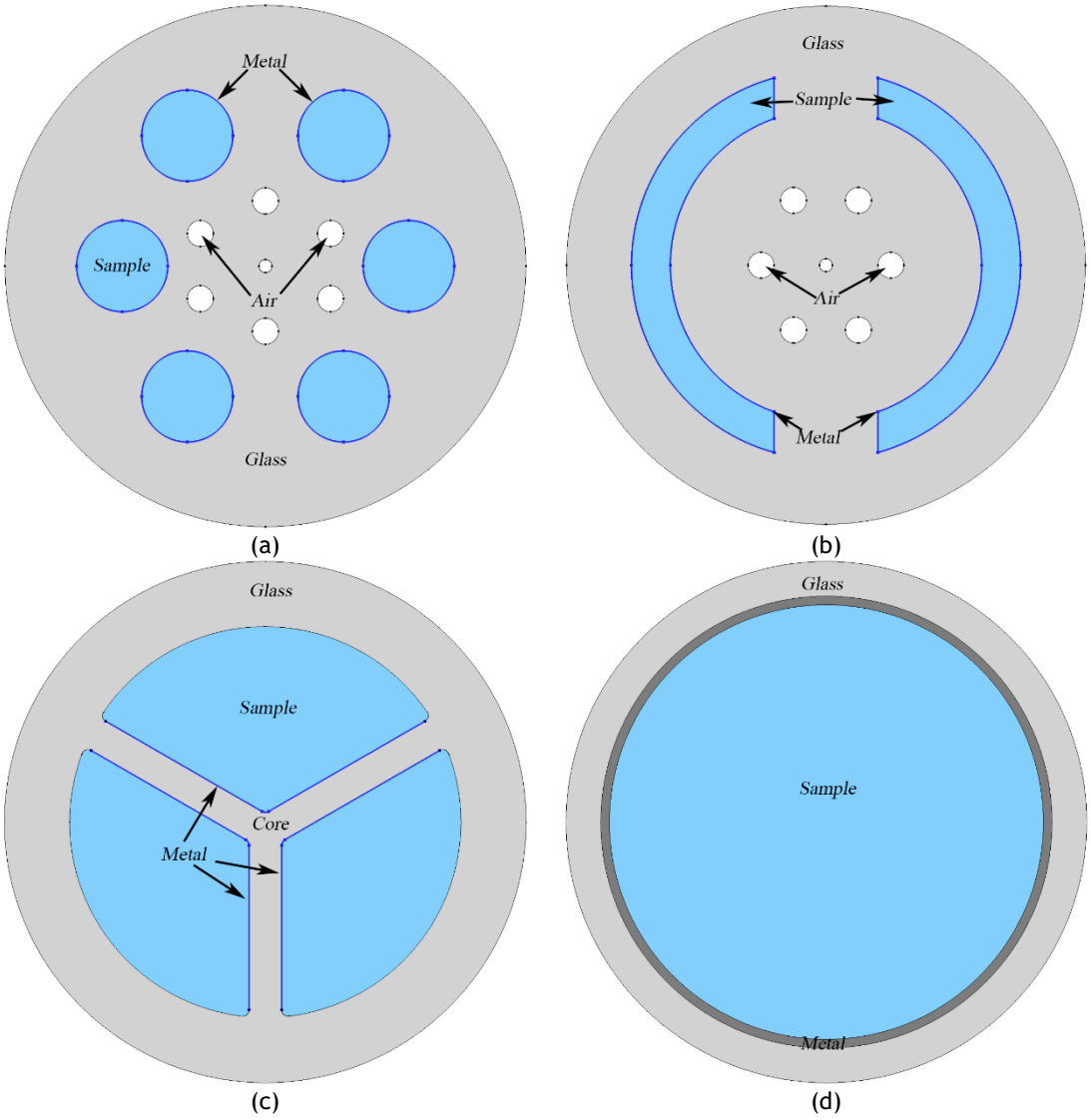

Figure 2.10 SPR fiber optic sensors based in photonic crystal fibers with; (a) with circular holes [55], (b) with crescent-shape holes, (c) MOF three structured holes (also called wagon wheel fiber) [12] and d) microcapillary fiber SPR sensor [56].

Figure 2.10a and Figure 2.10b show two types of MOF SPR sensors where the fundamental mode propagates in the region confined between the different air holes. In that process, light can couple with the multiple plasmonic modes supported by the circular metal, resulting in multiple peaks in the loss curve of the device. These MOF SPR sensors report a sensitivity in wavelength of 800 nm/RIU and 3000 nm/RIU, respectively, in the range of the external refractive index (sample) between 1.33 and 1.34 RI. The problem with these designs is the size of the circular hole and the consequent deposition of a thin layer of metal in these holes [55]. One solution for this problem is to use a fiber with larger holes, like the fibers depicted in Figure 2.10c and Figure 2.10d. Figure 2.10c shows a MOF with three holes. In this case the light is propagated in the center of the fiber, but results of the sensor show a low sensitivity

to refractive index in wavelength. Figure 2.10d illustrates the microcapillary fiber SPR sensor and the characteristic of this SPR sensor is that light travels in the medium with the highest refractive index (sample). This design reached a sensitivity of 6607 nm/RIU for a large high refractive index (>1.5 RI). In these configurations one of the main difficulties is the deposition of the metal inside the fiber.

Table 2.1 shows some parameters that characterize SPR sensors' performance, namely, sensitivity, resolution, wavelength operation, refractive index (RI) range of detection for different fiber optical structures [57]. Table 2.1 addresses SPR fiber structures with different geometrical configurations and coatings [18].

Table 2.1 Characteristics of general SPR-based fiber-optic sensors [1].

Optical structure	Characteristics	Detection RI range	Wavelength operation	Sensitivity/ Resolution	Ref.
Cladding-off cylindrical fiber					
Single metal coating	MMF, *Au-Ag* alloy nanoparticle.	1.342~1.346	400~800 nm	~3000 nm/RIU	[58]
	MMF, *Au*, surface roughness.	1.3335~ 1.4018	550~1000 nm	1600~3000 nm/RIU	[59]
	MMF, *Au*.	1.33~1.40	670 nm	2.5 x 10^{-4} RIU	[60]
	MMF, parameter analysis.	1.333 e 1.339	400~900 nm	2266.7~2780.1 nm/RIU	[61]
Multi-metal coating	*Au*, *Ag* double layer, *Au-Ag* alloy nanoparticle.			2500~3000 nm/RIU	[62]
With multi-layer	MMF, *Au*, dielectric multilayer. (SIO_2, TiO_2)	1.333 e 1.336 1.001~1.313	450~950 nm	10^{-5} RIU	[63]
Tapered fiber					
Off Cladding	MMF, *Au*, tapering ratio.	1.333 e 1.335		2700~4900 nm/RIU	[64]
	MMF, *Au*.	1.333~1.343	600~700 nm	2750~15000nm/RIU	[65]
With Cladding	SMF, *Au*, semi-cylindrical, multiple peaks.	1.440~1.454	400~1700 nm	7 x 10^{-7} RIU	[50]
D-Type fiber					
Single metal coating	SMF, cut core	1.33~1.40	632.8 nm	8 x 10^{-5} RIU	[66]
With overlayer	SMF, half of core polished, *Au*, Overlayer SiO_2	1.332~1.40	632.8 nm	2.5 x 10^{-6} RIU (phase)	[67]
	SMF, half of core polished, *Au*, Overlayer SiO_2	1.33~1.40	632.8 nm	2.5 x 10^{-5} RIU	[46]
	SMF, remained thin clad, Au, overlayer Ta_2O_5	1.329~1.393	760~940 nm	5 x 10^{-7} RIU	[68]
	SMF, *Au*, *Al* mirror, overlayer Ta_2O_5	1.32~1.42	825 nm	4 x 10^{-5} RIU	[69]
With thin cladding	PMF, polarization alignment.	1.33~1.339	700~900 nm	4 x 10^{-6} RIU	[70]
Modified fiber end					
Flat fiber tip	MMF, end mirror *Ag* and metal coating, *Au*.	1.333~1.346	400~840 nm	1557 nm/RIU	[54]

2.4.4 Plasmonic coating

The most simple designs of SPR sensor found in literature consist in a material that guides the light and a metal film, normally gold (Au), silver (Ag), copper (Cu) or alumina (Al), but there are countless possibilities to combine multiple metal coatings to improve the sensitivity, resolution and spectral operation region of the SPR sensor. Sharma in [71] studied different combinations of two metallic layers and these bi-metallic layers have a better performance that only one layer. We can also use a thin high refractive index overlayer after the metallic layer to shift the spectral operation sensing region [72]. We can also use metamaterials instead of pure metallic layers and improve the operational characteristics of the sensor [73]. The shape of the metallic layer is also studied to improve the sensor. The use of metallic wires permit an increase in the number of modes that couple with the fundamental mode and increase the performance of the sensor [74].

2.4.5 Fiber Grating SPR sensor

Until now, the most common mechanism of SPR excitation in an optical fiber is total internal reflection (TIR), where a part of the evanescent field that penetrates through the interface no ordinary total reflection can excite SPs. The evanescent field is increased by reducing the distance between the waveguide and the metal, and with that purposed, multiple designs were created (subsection 2.4.3). Another technology used for SPR excitation is fiber grating.

A fiber grating is a periodic structure in the refractive index of the fiber core that couples with a specific wavelength, producing an effective mirror for that wavelength. This technology allows the modes that are propagated in the core to be propagated in the cladding of the fiber and be coupled with the plasmonic modes without change the external geometry of the fiber. These structures are the Long Period Fiber Gratings (LPFGs) and Tilted Fiber Bragg Gratings (TFBGs) permitting the deposition of the metal directly on the fiber cladding. The use of LPFGs as SPR sensors was reported by Nemova *et al.* [75] and the use of TFBGs as SPR sensors was reported by Shevchenko *et al.* [76], as illustrated in Figure 2.11a and b, respectively.

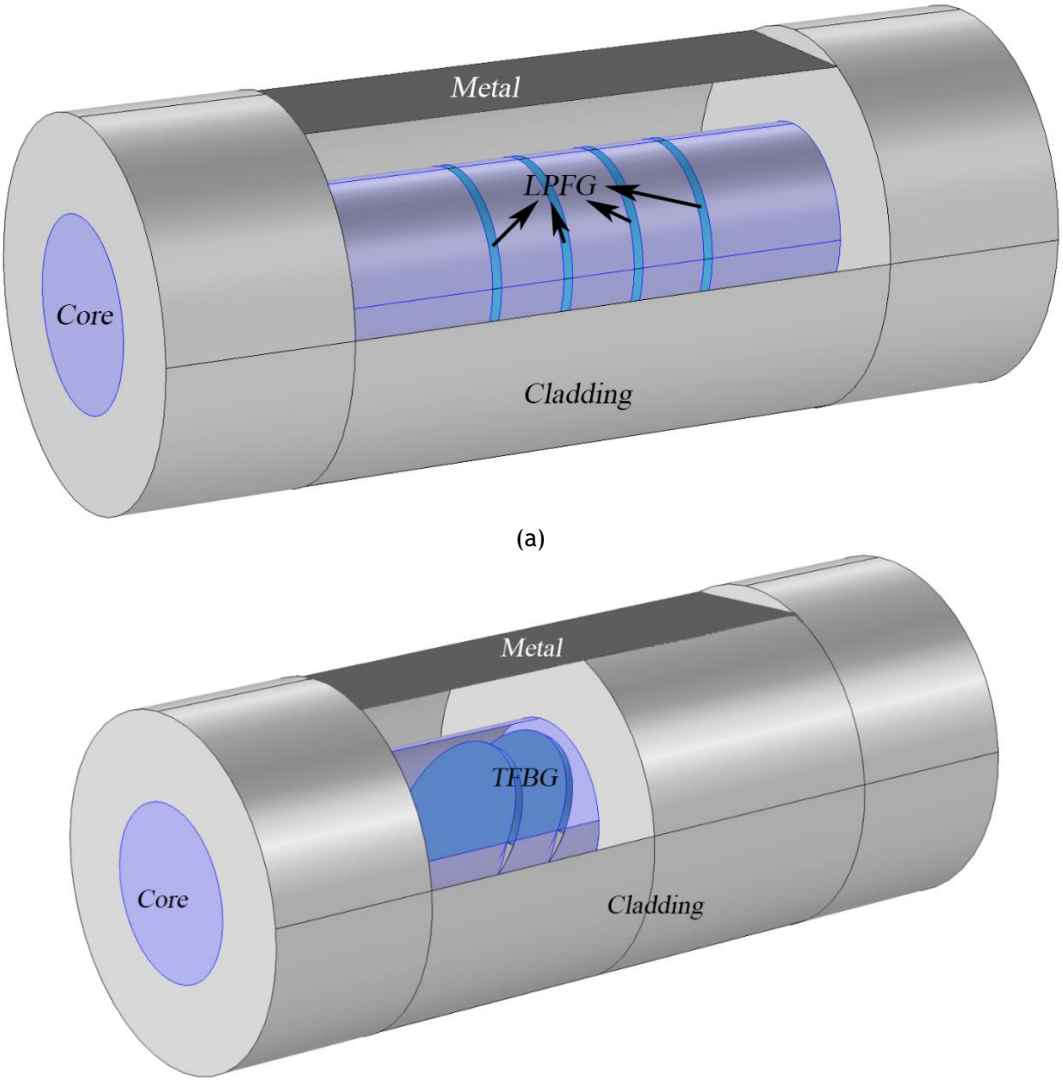

Figure 2.11 Examples of grating SPR sensor (a) with a long period grating (LPG), (b) with a tilted fiber Bragg grating TFBGs [1].

2.4.6 Application of the SPR sensor

SPR sensors are essentially refractive index sensors and the sensitivity and resolution of the sensor (characterization parameters) are calculated through the variation of the refractive index (δn), as shown in section 2.3. We also know the different components of the SPR sensor (thickness and type of metal, composition of the fiber, distance between the core and the metal, external refractive index, among others) change the effective refractive index of the sensor and consequently change the operational characteristics of the SPR sensor. The possibility to change these important parameters of the SPR sensor permits the optimization of the sensor.

The refractive index in a SPR sensor is the basic parameter measured by this sensor, but, with a proper configuration of the sensor, we can detect and analyze chemical, physical and biological values. Some examples of this applications are: Hassani in [77] used a Ferroelectric PVDF in a SPR sensor that allowed to detect values of the refractive index close to 1.00 RI, typically close to the refractive index of the gases.

Luan in [28] used a liquid with large thermo-optic coefficient, ideal for measure of temperature. Saikia in [78] created a pH sensor based on SPR of silver nanostructured film.

As stated before, another area of interest for SPR sensors are biosensors. To build a biosensor, a biorecognition layer has to be used with elements (e.g., antibodies polymeric coating) that recognize and are able to interact with a selected analyte. This element will change the refractive index accordingly in the presence of the analyte. Hence, this change will give rise to a change in the propagation constant of the surface plasmon [19]. Another application of this type of sensor is pH measurement, that used one layer based in the hydrophilic polymers after the layer of metal [79], [80]. Another application is the measurement of urea and glucose in the same fiber, but with different resonance wavelengths for each parameter under analysis [33].

Chapter 3 Models and methodology

In this chapter, we review the concepts of light propagation, addressed by electromagnetic theory. We also discuss the optical properties of dielectrics and metals. Next, we explain optical waveguide theory for a planar step-index and for a circular step-index guide, to understand the behavior of the different materials in these structures and finally the phenomena of SPR in optical fiber sensors is explained [81].

An introduction of the finite element method (FEM), the methods used for the simulation of SPR and the different problems of these methods in the simulations are also addressed.

3.1 Maxwell's equations

The electromagnetic fields in optical fiber waveguides are governed by the macroscopic Maxwell's equations in the absence of external currents or electric charges, say:

$$\nabla \times \boldsymbol{E}(\boldsymbol{r},t) = -\frac{\partial \boldsymbol{B}(\boldsymbol{r},t)}{\partial t} \tag{3.1}$$

$$\nabla \times \boldsymbol{H}(\boldsymbol{r},t) = j(\boldsymbol{r},t) + \frac{\partial \boldsymbol{D}(\boldsymbol{r},t)}{\partial t} \tag{3.2}$$

$$\nabla \cdot \boldsymbol{D}(\boldsymbol{r},t) = \rho(\boldsymbol{r},t) \tag{3.3}$$

$$\nabla \cdot \boldsymbol{B}(\boldsymbol{r},t) = 0 \tag{3.4}$$

where ***E***, ***H***, ***D*** and ***B*** are the electric, the magnetic, the dielectric and the magnetic induction fields, respectively. Also, the term ***j*** is the current density, ρ is the charge density, ***r*** is the spatial coordinate and *t* denotes time.

The dielectric and the magnetic fields are written as [82]

$$\boldsymbol{D}(\boldsymbol{r},t) = \varepsilon_0 \boldsymbol{E}(\boldsymbol{r},t) + \boldsymbol{P}(\boldsymbol{r},t) \tag{3.5}$$

$$\boldsymbol{H}(\boldsymbol{r},t) = \frac{1}{\mu_0}\boldsymbol{B}(\boldsymbol{r},t) - \boldsymbol{M}(\boldsymbol{r},t) \tag{3.6}$$

where ***P*** and ***M*** are the macroscopic polarization and magnetization, respectively, the constants ε_0 and μ_0 are the vacuum permittivity and vacuum permeability, respectively. The equations that relate the material properties with the electromagnetic fields are known as constitutive relations, and specifically relate ***D*** and ***B*** with ***E*** and ***H***.

In a linear, isotropic, nonmagnetic and nondispersive medium they have the form of [83]:

$$\boldsymbol{P} = \varepsilon_0 \chi_e \boldsymbol{E} \Rightarrow \boldsymbol{D} = \varepsilon_0 \varepsilon_r \boldsymbol{E} \tag{3.7}$$

$$\boldsymbol{M} = \chi_m \boldsymbol{H} \Rightarrow \boldsymbol{B} = \mu_0 \mu_r \boldsymbol{H} \tag{3.8}$$

$$\boldsymbol{j}_c = \sigma \boldsymbol{E} \tag{3.9}$$

where χ_e and χ_m are the electric and magnetic susceptibility, $\varepsilon_{\mathrm{r}} \equiv 1 + \chi_e$ and $\mu_{\mathrm{r}} \equiv 1 + \chi_m$ are the relative permittivity and relative permeability of the material, respectively and σ is the conductivity.

Time-harmonic solutions describing strictly monochromatic fields are of the form:

$$\boldsymbol{E}(\boldsymbol{r},t) = \boldsymbol{E}(\boldsymbol{r},\omega)\exp\left(-j\omega t\right) \tag{3.10}$$

$$\boldsymbol{H}(\boldsymbol{r},t) = \boldsymbol{H}(\boldsymbol{r},\omega)\exp(-j\omega t) \tag{3.11}$$

where ω is the angular frequency of light. In this representation, the fields are complex quantities whose real parts correspond to the physical fields [10]. Therefore, the next constitutive relations can be described as:

$$\boldsymbol{D}(\boldsymbol{r},t) = \varepsilon_0 \varepsilon_r \boldsymbol{E}(\boldsymbol{r},\omega)\exp(-j\omega t) \tag{3.12}$$

$$\boldsymbol{B}(\boldsymbol{r},t) = \mu_0 \boldsymbol{H}(\boldsymbol{r},\omega)\exp(-j\omega t) \tag{3.13}$$

$$\boldsymbol{j}_c(\boldsymbol{r},t) = \sigma \boldsymbol{E}(\boldsymbol{r},\omega)\exp(-j\omega t) \tag{3.14}$$

For complex optical structures composed of elements with different materials, these constants include the dielectric, magnetic constant and conductivity, which vary along the system from point to point and therefore can be considered as position dependent functions.

Taking the curl of equation 3.1 and using equations 3.3, 3.12 and 3.13, yields the wave equation for the Fourier components of the electric field, which is the same one that COMSOL Multiphysics uses to determine the eigenvalues and eigenmodes of the electric field:

$$\nabla \times \left[\nabla \times \boldsymbol{E}(\boldsymbol{r},\omega) - k_0^2\left(\tilde{\varepsilon}_r(\boldsymbol{r},\omega)\right)\right]\boldsymbol{E}(\boldsymbol{r},\omega) = 0 \tag{3.15}$$

Applying the same reasoning for the magnetic field, it comes:

$$\nabla \times \left(\tilde{\varepsilon}_r(\boldsymbol{r},\omega)\right)^{-1} \nabla \times \boldsymbol{H}(\boldsymbol{r},\omega) - k_0^2 \boldsymbol{H}(\boldsymbol{r},\omega) \tag{3.16}$$

where $k_0 = \omega / c$ is the wavenumber of the mode of the field and $c = 1/\sqrt{\varepsilon_0 \mu_0}$ is the speed of light in vacuum. In this work the angular frequency ω is replaced by the wavelength λ, where the relation between the two components is $\omega = 2\pi c / \lambda = c k_0$.

The term $\tilde{\boldsymbol{\varepsilon}}_r(\boldsymbol{r},\omega) = \boldsymbol{\varepsilon}_r(\boldsymbol{r},\omega) - j\boldsymbol{\sigma}(r,\omega)/\omega\varepsilon_0$ represents the effective complex relative dielectric function, which includes the contribution of the material-dependent (real valued) relative permittivity $\boldsymbol{\varepsilon}_r(\boldsymbol{r},\omega)$, mostly determined by the bound state of the optical active modes of the material [84], and the contribution of the Ohmic conductivity of the material $\boldsymbol{\sigma}(\boldsymbol{r},\omega)$.

3.2 The Lorentz and the Drude models, and the optical properties of the gold, silver, aluminum and copper

The Lorentz and Drude models are the most basic models to calculate the optical properties of materials in terms of complex index of refraction and of dielectric constant for different wavelengths or frequencies of light [85].

3.2.1 The Lorentz model

The Lorentz model is based on the study of the interaction between the electromagnetic field and the material. When any electromagnetic field is applied to the material, the conduction electrons and other charges in the material react and move away of the is equilibrium position, thus varying the local dipole moment of the material. In a simple way, one may consider that light causes the different charged particles in the material to vibrate, altering their relative separation. The resulting oscillating dipoles work as small antennas that re-emit light and are responsible for the optical properties of the material. The main contribution comes from the electrons, which are the lightest of these particles and therefore are those which vibrate with the largest amplitudes. Their behavior can be described by the following equation [86]:

$$m_e \left(\frac{d^2 \boldsymbol{x}}{dt^2} + \Gamma \frac{d\boldsymbol{x}}{dt} + \omega_0^2 \boldsymbol{x} \right) = -e\boldsymbol{E} \tag{3.17}$$

where m_e is the electron mass, Γ the damping rate, ω_0 is the resonant frequency of the oscillator (undamped), e is the electron charge and $\boldsymbol{x}$ is the time varying electron displacement. Equation 3.17 contains four terms that describe different effects: the Lorentz force associated with the force produced by the electromagnetic field on the electron, the damping force associated with electron collisions and other mechanisms of incoherent losses, the restoring force which traps the electron to the atom and the electric field driving force. Equation 3.17 can be solved in reciprocal space using the Fourier transform, resulting in an amplitude of oscillation given by:

$$\boldsymbol{r}(\omega) = -\frac{e}{m_e}\frac{\boldsymbol{E}(\omega)}{\omega_0^2 - \omega^2 + i\omega\Gamma} \tag{3.18}$$

The Fourier component of the dipole moment, associated with this vibration is defined as:

$$\boldsymbol{p}(\omega) = \frac{e^2}{m_e}\frac{\boldsymbol{E}(\omega)}{\omega_0^2 - \omega^2 + i\omega\Gamma} \tag{3.19}$$

while the polarization for all the atoms per volume (*N*) is defined as:

$$\boldsymbol{P}(\omega) = N\boldsymbol{p}(\omega) = N\frac{e^2}{m_e}\frac{\boldsymbol{E}(\omega)}{\omega_0^2 - \omega^2 + i\omega\Gamma} \tag{3.20}$$

Combining equations 3.20 and 3.7, it is possible to find the value of the susceptibility and the permittivity of the material considering only one oscillator:

$$\chi(\omega) = \left(\frac{Ne^2}{\varepsilon_0 m_e}\right)\frac{1}{\omega_0^2 - \omega^2 - j\omega\Gamma} \Rightarrow \varepsilon_r(\omega) = 1 + \left(\frac{Ne^2}{\varepsilon_0 m_e}\right)\frac{1}{\omega_0^2 - \omega^2 - j\omega\Gamma} \tag{3.21}$$

For real materials, the dielectric function is assumed to be equal to the sum of contributions from individual oscillators. The equation of the permittivity of the multiple oscillator is given by [87]:

$$\varepsilon_r(\omega) = \varepsilon_\infty + \sum_{m=1}^{N}\frac{f_m\omega_p^2}{\omega_{0m}^2 - \omega^2 - j\omega\Gamma_m} \tag{3.22}$$

where ω_p is the plasma frequency, *m is* the number of the oscillator resonant with frequency ω_{0m}, f_m is related to the strength of the oscillator and ε_∞ is the permittivity at the infinite frequency.

3.2.2 The Drude model

This model explains the transport properties of conduction electrons in metals. Electrons in metals with higher energy and near the Fermi level can be excited into other energy and momentum states by photons with very small energies (metals tend to be either highly absorbing or reflecting at visible and infrared wavelengths). If These electrons can be considered “free”, then the Drude oscillator is a simplification of the single Lorentz oscillator where the resonance frequency (ω_{0m}) is equal to 0, because there is no “spring” to connect free electrons with ions. Applying this condition, equation 3.20 yields the Drude model for the optical properties of a free-electron metal [81]:

$$\varepsilon_r(\omega) = 1 - \frac{\omega_p^2}{\omega^2 + j\omega\Gamma} \tag{3.23}$$

where the plasma frequency is stated by $\omega_p^2 = N_e e^2 / m_e\varepsilon_0$, being N_e the density of the electron.

3.2.3 The Sellmeier equation

The electric and magnetic fields are dependent on the angular frequency (equations 3.10 and 3.11), as well as, on the refractive index of the materials. Therefore, it is necessary to calculate the material's index of refraction for all frequencies under study. Typically, in a dielectric layer, the refractive index can be calculated using Sellmeier's equation [88]:

$$n^2(\lambda) = 1 + \sum_{i=1}^{3} \frac{B_i \lambda^2}{\lambda^2 - C_i^2} \tag{3.24}$$

where B_i, C_i are the Sellmeier coefficients, determined experimentally. Table 3.1 presents the Sellmeier coefficients for different materials like the germanium, silica, alumina and plastic (Poly(methyl methacrylate) - PMMA).

Table 3.1 Sellmeier coefficients for germanium, silica, alumina and PMMA

Material	B_1	B_2	B_3	C_1	C_2	C_3	Ref.
SiO_2	0.696166	0.407942	0.897479	0.068404	0.116241	9.896161	[88]
GeO_2	0.8068664	0.7181585	0.8541683	0.06897261	0.1539661	11.84193	[88]
Al_2O_3	1.4313493	0.65054713	5.3414021	0.00726631	0.1193242	18.028251	[89]
PMMA	0.4963	0.6965	0.3223	0.0718	0.1174	0.9237	[90]

The SiO_2 core of the optical fiber is normally doped with a X percentage of GeO_2. The calculation of the refractive index as a function of the wavelength in pure silica and in a glass doped with a X percentage of GeO_2 follows the Sellmeier relation according to:

$$n = \left\{ 1 + \sum_{i=1}^{3} \frac{\left[B_i^S + X(B_i^G - B_i^S) \right] \lambda^2}{\lambda^2 - \left[C_i^S + X(C_i^G - C_i^S) \right]^2} \right\}^{1/2} \tag{3.25}$$

where B_i^S, C_i^S, B_i^G and C_i^G are the Sellmeier coefficients and the superscripts *S* and *G* denote SiO_2 and GeO_2, respectively. The values of these parameters are represented in Table 3.1. However, for some specific dielectric materials the Sellmeier's not provide the best description of the dependency of the refractive index with wavelength and other approximations are used. For example, for Ta_2O_5 the refractive index is calculated as:

$$n = 1.878 + \frac{0.0178}{\lambda^2} + \frac{52.7 \times 10^{-5}}{\lambda^4} \tag{3.26}$$

In this thesis, we have considered that the optical fiber core is composed of pure silica with 16% of germanium (GeO_2-SiO_2) and the optical fiber cladding is composed of pure silica. The refractive index of the core and cladding as a function of the wavelength is shown in Figure 3.1.

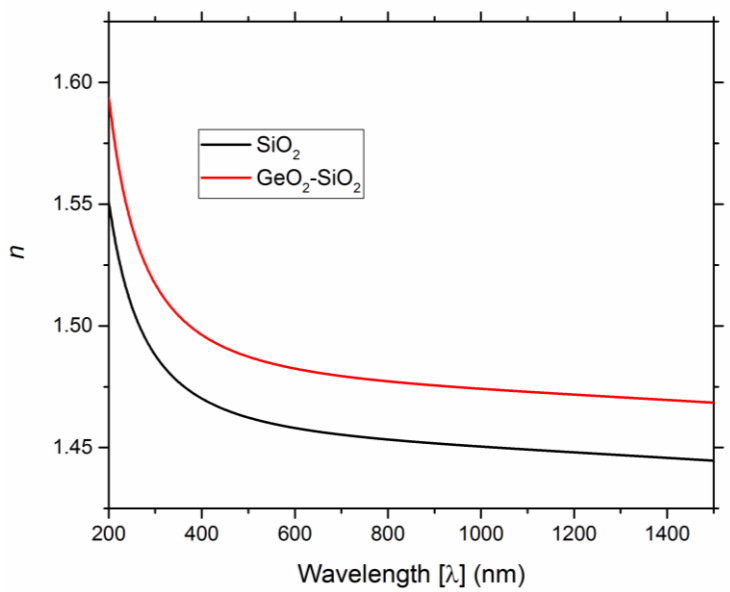

Figure 3.1 Refractive index of the core (GeO_2-SiO_2) and of the cladding (SiO_2).

3.2.4 Optical properties of gold, silver, aluminum and copper

The optical properties of a metal can be obtained through equation 3.23. Also, the permittivity and the refractive index can be obtained from the Drude model as function of wavelength as:

$$\varepsilon_m(\lambda) = 1 + \frac{\lambda^2 \lambda_c}{\lambda_P{}^2 (\lambda_c + j\lambda)} \tag{3.27}$$

where the permittivity is defined through the refractive index as:

$$\sqrt{\varepsilon_m(\lambda)} = n_m(\lambda) + jk_m(\lambda) \tag{3.28}$$

n_m and k_m are the real and imaginary parts of the index of refraction for the metal, respectively, ε_m is the complex permittivity of the metal and λ_p and λ_c denote the plasma wavelength ($\lambda_P = 2\pi c/\omega_p$) and the collision wavelength ($\lambda_c = 2\pi c/\Gamma$), respectively. Typical values of the plasma and collision wavelengths are shown in Table 3.2 [71] for Ag, Au, Cu and Al.

Table 3.2 Plasma and collision wavelengths used for different metals [71].

Metal	Plasma wavelength (λ_P) (m)	Collision wavelength (λ_c) (m)
Silver (Ag)	1.4541×10^{-7}	1.7614×10^{-5}
Gold (Au)	1.6826×10^{-7}	8.9342×10^{-6}
Aluminum (Al)	1.0657×10^{-7}	2.4511×10^{-5}
Copper (Cu)	1.3617×10^{-7}	4.0852×10^{-5}

The Drude model presented in equation 3.27 is valid to study the behavior of the optical properties in the visible/near-ultraviolet (*uv*) region for the most of the metals mentioned in Table 3.2 (not considering Au) [71]. In the particular case of Au, it is not

so effective in the violet/near-uv region (wavelengths < 400 nm). The reason for that is the more important role played by interband transitions in the violet/near-uv region. For this reason, Etchegoin in [85] considered the two interband transitions in gold and determined the full mode permittivity relation of Au as function of the frequency as:

$$\varepsilon_{Au}(\omega) = \varepsilon_{\infty} - \frac{\omega_p^2}{(\omega^2 + j\Gamma\omega)} + \sum_{i=1}^{2} C_i \left[\frac{e^{j\phi_i}}{(\omega_i - \omega - j\Gamma_i)} + \frac{e^{-j\phi_i}}{(\omega_i + \omega + j\Gamma_i)} \right] \tag{3.29}$$

where the third and four elements in the equation represent the contributions of the interband transitions (gaps). In equation 3.29, C_i is the amplitude, ϕ_i is the phase, ω_i is the energy of the gap, Γ_i is the broadening and we can also describe the relation as function of wavelength as:

$$\varepsilon_{Au}(\lambda) = \varepsilon_{\infty} - \frac{1}{\lambda_P{}^2 (1/\lambda^2 + j/\lambda_c\lambda)} + \sum_{i=1}^{2} \frac{A_i}{\lambda_i} \left[\frac{e^{j\phi_i}}{(1/\lambda_i - 1/\lambda - j/\gamma_i)} + \frac{e^{-j\phi_i}}{(1/\lambda_i + 1/\lambda + j/\gamma_i)} \right] \tag{3.30}$$

where $\lambda_i = 2\pi c/\omega_i$ is the interband transition in wavelength, $\gamma_i = 2\pi c/\Gamma_i$ is the transition broadening expressed in wavelength units, and $A_i = C_i/\omega_i$ is the dimensionless critical point amplitude. Also C_i, ϕ_i, ω_i and Γ_i are the amplitude, phase, energy of the gap in frequency units and the broadening, respectively [85]. The values of the parameters of equation 3.30 are represented in the Table 3.3.

Table 3.3 Coefficients for gold from reference [85].

ε_{∞}	λ_P [nm]	λ_c [nm]	i	A_i	ϕ_i	λ_i [nm]	γ_i [nm]
1.54	1.43	14500					
			1	1.27	$-\pi/4$	470	1900
			2	1.1	$-\pi/4$	325	1060

The behavior of the Drude model with and without the interband transition (equations 3.27 and 3.30) is shown in Figure 3.2. This Figure illustrates the variation of the real and imaginary part of the refractive index (Figure 3.2a) and of the permittivity (Figure 3.2b) as function of the wavelength for silver and gold, in the case of gold with and without the interband transition.

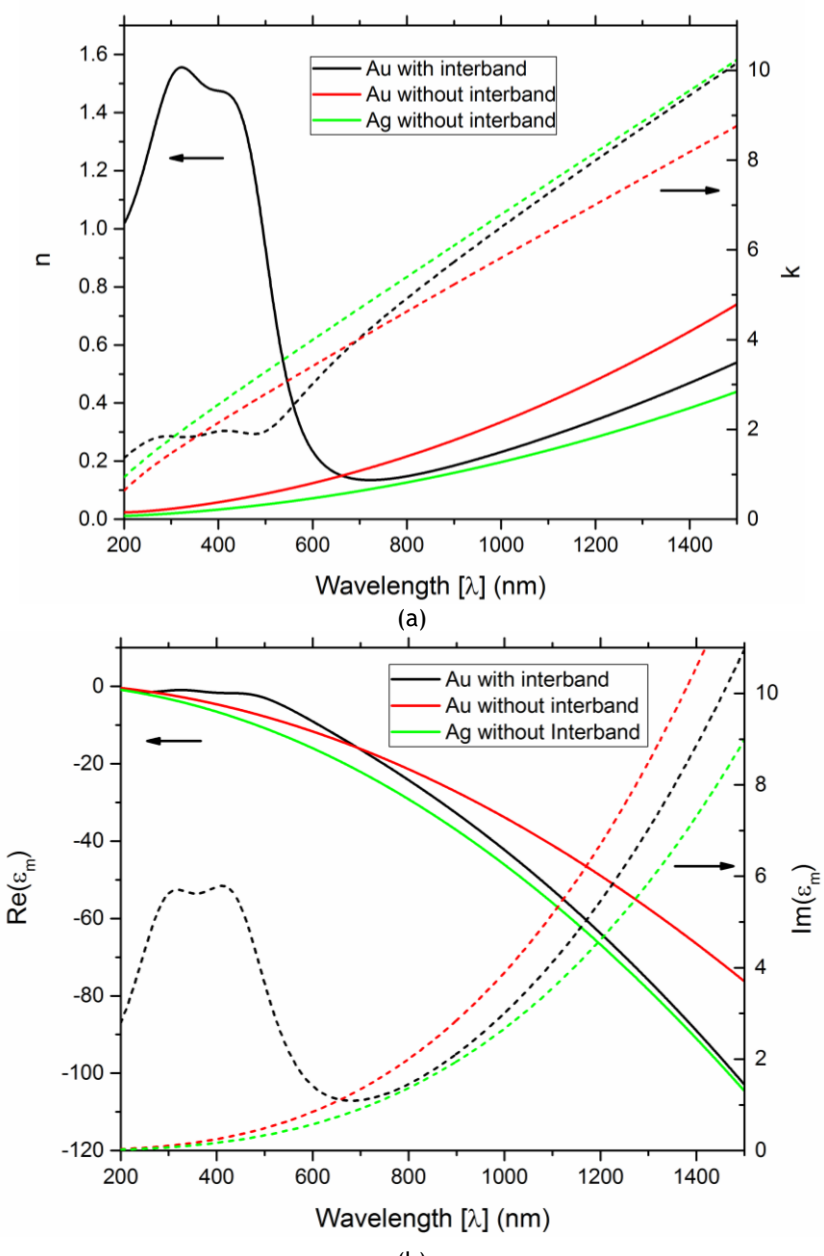

Figure 3.2 (a) Refractive index and (b) permittivity of gold (Au) and silver (Ag). The solid lines are the real part of the refractive index and permittivity, the dashed lines are the imaginary part of the refractive index and permittivity, respectively. The black and red lines refer to the gold with and without interband, respectively, and the green line refers to silver.

From Figure 3.2 we observe that the difference between the Drude model with and without interband is considerable. Comparing the results of these models with the experimental values from Johnson in [91], one concludes that equation 3.30 is a good approximation of the behavior of the gold. On the other hand, equation 3.27 can be a good approximation for silver [85].

3.3 Optical waveguide theory

In this section, we are interested in the study of electromagnetic modes in cylindrical (core of the optical fiber and metallic wire) and planar (slab inclusions)

geometries. The slab inclusion comprehends two types of materials, metal and high refractive index material.

3.3.1 Definitions and properties of guided modes

Waveguides not only confine the electromagnetic (EM) field, but also and more importantly, constrain the directions of propagation of the field. Waveguides are distinguished according to their geometry and consequently the type of confinement obtained, ranging from planar to axial waveguides, being the optical fiber the most notorious and used technological application of waveguides. This spatial confinement results in a discrete set of solutions of the wave equations 3.10 and 3.11, which are usually called guided modes. In optical fibers, the dependency in the spatial z coordinate along the axis is obtained using the variable separation method:

$$E_i(r) = e_i(x, y)\exp(-j\beta_i z) \tag{3.31}$$

$$H_i(r) = h_i(x, y)\exp(-j\beta_i z) \tag{3.32}$$

where β_i is the propagation constant of the *i*-th mode, e_i and h_i are the electric and magnetic fields of the guided *i*-th mode, respectively. The propagation constant of one mode can be written as function of the effective refractive index (n_{eff}) as

$$\beta = n_{eff}k_0 = (n_{eff}' + jn_{eff}'')k_0 \tag{3.33}$$

where n_{eff}' and n_{eff}'' are the respective real and imaginary parts of the effective refractive index.

3.3.2 Poynting vector, total power and loss in the guided mode

The optical power flow carried by a guided mode is characterized by the real part of the time-averaged Poynting vector as:

$$\boldsymbol{S} = (1/2)\,\mathrm{Re}(\boldsymbol{E}\times\boldsymbol{H}^*) = (1/2)\,\mathrm{Re}(\boldsymbol{e}\times\boldsymbol{h}^*)\exp(-\alpha z) \tag{3.34}$$

where $\alpha = 2n_{eff}''k_0$ is known as the power absorption coefficient. The Poynting vector has the same direction of the EM wave, and that means the Poynting vector can be reduced to a scalar field $S_z = \boldsymbol{S}\cdot z$. The total power *P* of a guided mode after a propagation distance *z* = *L* (where *L* is the length of the sensing fiber) is given by integrating the power density across an infinite cross section A_∞:

$$P = \int_{A_\infty} S_z dA = \frac{1}{2}e^{\alpha L}\int_{A_\infty}\mathrm{Re}(\boldsymbol{e}\times\boldsymbol{h}^*)dA \tag{3.35}$$

In the field of optics, the absorption coefficient is most commonly represented in terms of decibel as:

$$\alpha_{dB} = \frac{20}{\ln 10}\alpha L \tag{3.36}$$

3.3.3 The planar step-index waveguide

The planar step-index waveguide is the simplest of step profile waveguides and in this thesis is used to provide a simple tool to model and help to understand the behavior of the modes in metal and in high refractive index planar profiles, as shown in Figure 3.3.

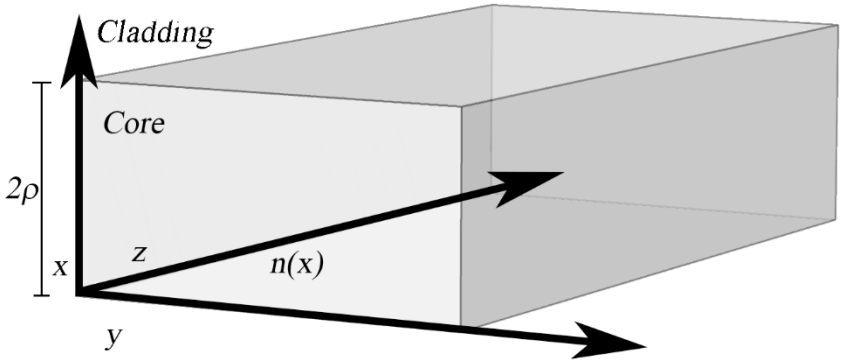

Figure 3.3 Schematic of the planar step-index waveguide.

The schematic of the planar step-index waveguide is represented in the Figure 3.3 and the profile is defined as

$$n(x) = \begin{matrix} n_{co}; & 0 < x < 2\rho \\ n_{cl}; & 2\rho < x < \infty \end{matrix} \quad \text{where } n_{co} > n_{cl} \tag{3.37}$$

where ρ is the core half width, n_{co} and n_{cl} are the refractive index of the core and of the cladding, respectively. Also, it is possible to define more complex structures that include components of different materials such as an internal medium (*e.g.* composed of a dielectric or an absorbing dielectric) surrounded by external medium. This guide is a two-dimensional waveguide and by orienting it in a system of Cartesian axes, the fields depend on *x* and *z*, that means the equations 3.30 and 3.32 can be described as:

$$E_i(x,z) = e_i(x)\exp(-j\beta_i z) \tag{3.38}$$

$$H_i(x,z) = h_i(x)\exp(-j\beta_i z) \tag{3.39}$$

We can express the transverse fields in terms of the longitudinal fields by [92]:

$$e_x = \frac{j}{p}\left[\beta\frac{\partial e_z}{\partial x} + \left(\frac{\mu_0}{\varepsilon_0}\right)^{1/2} k_0 \frac{\partial h_z}{\partial_y}\right]; \qquad e_y = \frac{j}{p}\left[\beta\frac{\partial e_z}{\partial y} - \left(\frac{\mu_0}{\varepsilon_0}\right)^{1/2} k_0 \frac{\partial h_z}{\partial_x}\right], \tag{3.40}$$

$$h_x = \frac{j}{p}\left[\beta\frac{\partial h_z}{\partial x} - \left(\frac{\varepsilon_0}{\mu_0}\right)^{1/2} k_0 n^2 \frac{\partial e_z}{\partial_y}\right]; \quad h_y = \frac{j}{p}\left[\beta\frac{\partial h_z}{\partial y} + \left(\frac{\varepsilon_0}{\mu_0}\right)^{1/2} k_0 n^2 \frac{\partial e_z}{\partial_x}\right], \tag{3.41}$$

where $p = n^2 k_0^2 - \beta^2$ and n takes either the value of n_{co} or n_{cl} depending in which region the fields are calculated. In the case of the planar waveguide, we consider that the structure is infinitely extended in the *y* direction, and the partial derivative as function of *y* is equal to 0. Equations 3.40 and 3.41 can be written as:

$$e_x = \frac{j}{p}\beta\frac{\partial e_z}{\partial x};\quad e_y = -\frac{j}{p}\left(\frac{\mu_0}{\varepsilon_0}\right)^{1/2} k_0\frac{\partial h_z}{\partial_x}; \tag{3.42}$$

$$h_x = \frac{j}{p}\beta\frac{\partial h_z}{\partial x}\quad h_y = \frac{j}{p}\left(\frac{\varepsilon_0}{\mu_0}\right)^{1/2} k_0 n^2\frac{\partial e_z}{\partial_x}, \tag{3.43}$$

We obtain a solution for e_z and h_z by solving the wave equations 3.15 and 3.16 and using the equation 3.37 we obtain:

$$\left(\rho^2\frac{d^2}{dx^2}+U^2\right)\Psi = 0; \qquad 0 \leq |x| < 2\rho \tag{3.44}$$

$$\left(\rho^2\frac{d^2}{dx^2}-W^2\right)\Psi = 0; \qquad 2\rho < |x| < \infty \tag{3.45}$$

where $U = k_0\rho\sqrt{\left(n_{co}^2 - n_{eff}{}^2\right)}$ and $W = k_0\rho\sqrt{\left(-n_{cl}^2 + n_{eff}{}^2\right)}$ are the model parameters of the core and of the cladding, respectively. Ψ denotes one of the longitudinal field components, e_z or h_z [92].

The eigenvalue equation for the planar waveguide mode can be defined by two types of polarization states of the electromagnetic field: the transverse magnetic (TM) and transverse electric (TE) modes. TM modes do not have longitudinal magnetic field ($h_z = 0$) and we TE modes when do not have longitudinal electric field ($e_z = 0$). The modal field components for a step-profile planar waveguide are represented in Table 3.4 for modes TE and in Table 3.5 for modes TM [92].

Table 3.4 Modal field components for step-profile planar waveguide for the modes TE, where $X = x/\rho$ is the normalized radial distances and the $e_x = e_z = h_y = 0$ [92].

		Core	Cladding
e_y	Even	$\frac{\cos(UX)}{\cos(U)}$	$\frac{\exp(-W\lvert X\rvert)}{\exp(-W)}$
	Odd	$\frac{\sin(UX)}{\sin(U)}$	$\frac{X}{\lvert X\rvert}\frac{\exp(-W\lvert X\rvert)}{\exp(-W)}$
h_x	Even	$-\frac{\beta}{k_0}\left(\frac{\varepsilon_0}{\mu_0}\right)^{1/2}\frac{\cos(UX)}{\cos(U)}$	$-\frac{\beta}{k_0}\left(\frac{\varepsilon_0}{\mu_0}\right)^{1/2}\frac{\exp(-W\lvert X\rvert)}{\exp(-W)}$
	Odd	$-\frac{\beta}{k_0}\left(\frac{\varepsilon_0}{\mu_0}\right)^{1/2}\frac{\sin(UX)}{\sin(U)}$	$-\frac{\beta}{k_0}\left(\frac{\varepsilon_0}{\mu_0}\right)^{1/2}\frac{X}{\lvert X\rvert}\frac{\exp(-W\lvert X\rvert)}{\exp(-W)}$
h_z	Even	$\frac{jW}{k_0\rho}\left(\frac{\varepsilon_0}{\mu_0}\right)^{1/2}\frac{\sin(UX)}{\sin(U)}$	$\frac{jW}{k_0\rho}\left(\frac{\varepsilon_0}{\mu_0}\right)^{1/2}\frac{X}{\lvert X\rvert}\frac{\exp(-W\lvert X\rvert)}{\exp(-W)}$
	Odd	$\frac{jW}{k_0\rho}\left(\frac{\varepsilon_0}{\mu_0}\right)^{1/2}\frac{\cos(UX)}{\cos(U)}$	$\frac{jW}{k_0\rho}\left(\frac{\varepsilon_0}{\mu_0}\right)^{1/2}\frac{\exp(-W\lvert X\rvert)}{\exp(-W)}$

Table 3.5 Modal field components for step-profile planar waveguide for the modes TM, where the $X = x/\rho$ is the normalized radial distances and the $e_y = h_z = h_x = 0$ [92].

		Core	Cladding
e_x	Even	$\frac{\cos(UX)}{\cos(U)}$	$\frac{n_{co}^2}{n_{cl}^2}\frac{\exp(-W\mid X\mid)}{\exp(-W)}$
	Odd	$\frac{\sin(UX)}{\sin(U)}$	$\frac{n_{co}^2}{n_{cl}^2}\frac{X}{\mid X\mid}\frac{\exp(-W\mid X\mid)}{\exp(-W)}$
h_y	Even	$\frac{n_{co}^2 k_0}{\beta}\left(\frac{\varepsilon_0}{\mu_0}\right)^{1/2}\frac{\cos(UX)}{\cos(U)}$	$\frac{n_{co}^2 k_0}{\beta}\left(\frac{\varepsilon_0}{\mu_0}\right)^{1/2}\frac{\exp(-W\mid X\mid)}{\exp(-W)}$
	Odd	$\frac{n_{co}^2 k_0}{\beta}\left(\frac{\varepsilon_0}{\mu_0}\right)^{1/2}\frac{\sin(UX)}{\sin(U)}$	$\frac{n_{co}^2 k_0}{\beta}\left(\frac{\varepsilon_0}{\mu_0}\right)^{1/2}\frac{X}{\mid X\mid}\frac{\exp(-W\mid X\mid)}{\exp(-W)}$
e_z	Even	$-\frac{jW}{\rho\beta}\frac{n_{co}^2}{n_{cl}^2}\frac{\sin(UX)}{\sin(U)}$	$-\frac{jW}{\rho\beta}\frac{n_{co}^2}{n_{cl}^2}\frac{X}{\mid X\mid}\frac{\exp(-W\mid X\mid)}{\exp(-W)}$
	Odd	$-\frac{jW}{\rho\beta}\frac{n_{co}^2}{n_{cl}^2}\frac{\cos(UX)}{\cos(U)}$	$-\frac{jW}{\rho\beta}\frac{n_{co}^2}{n_{cl}^2}\frac{\exp(-W\mid X\mid)}{\exp(-W)}$

The eigenvalue equations for a planar step-index (applied only if the length of the metal is infinite or close to infinite, in numerical terms) are:

$$\text{TM modes}\ \begin{cases} Even \rightarrow n_{co}^2 W = n_{cl}^2 U\tan U \\ Odd \rightarrow n_{co}^2 W = -n_{cl}^2 U\cot U \end{cases} \tag{3.46}$$

$$\text{TE modes}\ \begin{cases} Even \rightarrow W = U\tan U \\ Odd \rightarrow W = -U\cot U \end{cases} \tag{3.47}$$

where each value of the effective refractive index n_{eff} must lie in the range for bound modes $n_{cl} < n_{eff} < n_{co}$. These equations are transcendental and cannot be solved analytically, instead numerical methods have to be used.

3.3.4 The circular step-index waveguide

In the case of a circular or fiber step-index waveguide, the same method used to study the planar waveguide can be applied. The schematic of the fiber step-index waveguide is shown in Figure 3.4.

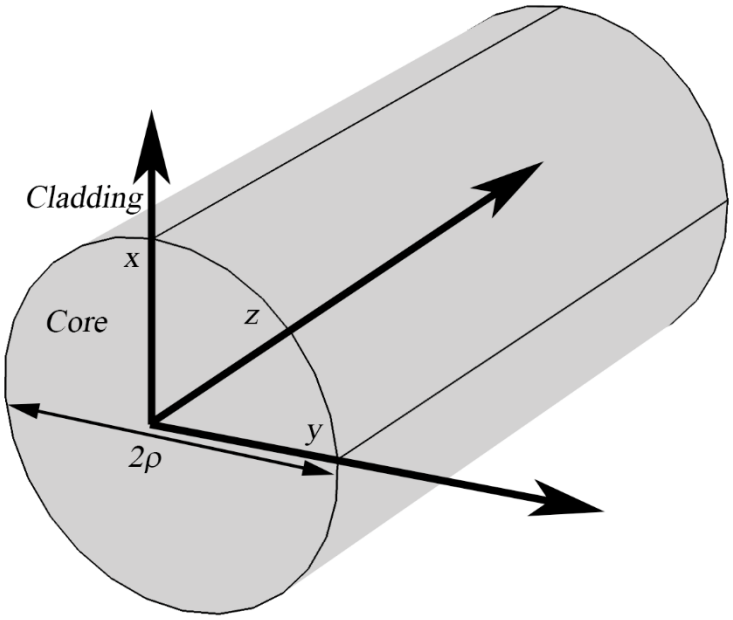

Figure 3.4 Schematic of the fiber step-index waveguide.

In this case ρ is the radius of the fiber and the use of the Cartesian coordinate system is not the best choice, because with a cylindrical symmetry it is more convenient to use the polar coordinate system. That means, that equations 3.30 and 3.32 can be expressed as:

$$E_i(r,\phi,z) = e_i(r,\phi)\exp(-j\beta_i z) \tag{3.48}$$

$$H_i(r,\phi,z) = h_i(r,\phi)(-j\beta_i z) \tag{3.49}$$

From waveguide theory and considering polar coordinates, we assume that the transverse field components can be expressed in terms of the longitudinal field components e_z and h_z as [92]:

$$e_r = \frac{j}{p}\left[\beta\frac{\partial e_z}{\partial r} + \left(\frac{\mu_0}{\varepsilon_0}\right)^{1/2}\frac{k_0}{r}\frac{\partial h_z}{\partial\phi}\right]; \qquad e_\phi = \frac{j}{p}\left[\frac{\beta}{r}\frac{\partial e_z}{\partial\phi} - \left(\frac{\mu_0}{\varepsilon_0}\right)^{1/2}k_0\frac{\partial h_z}{\partial r}\right], \tag{3.50}$$

$$h_r = \frac{j}{p}\left[\beta\frac{\partial h_z}{\partial r} - \left(\frac{\varepsilon_0}{\mu_0}\right)^{1/2}\frac{k_0 n^2}{r}\frac{\partial e_z}{\partial\phi}\right]; \qquad h_\phi = \frac{j}{p}\left[\frac{\beta}{r}\frac{\partial h_z}{\partial\phi} + \left(\frac{\varepsilon_0}{\mu_0}\right)^{1/2}k_0 n^2\frac{\partial e_z}{\partial r}\right]. \tag{3.51}$$

As the planar waveguide, we can obtain a solution for e_z and h_z by solving the wave equations 3.15 and 3.16 and we deduce that:

$$\left(\frac{\partial^2}{\partial R^2} + \frac{1}{R}\frac{\partial}{\partial R} + \frac{1}{R^2}\frac{\partial^2}{\partial\phi^2} + U^2\right)\Psi = 0; \qquad 0 \le R < 1 \tag{3.52}$$

$$\left(\frac{\partial^2}{\partial R^2} + \frac{1}{R}\frac{\partial}{\partial R} + \frac{1}{R^2}\frac{\partial^2}{\partial\phi^2} - W^2\right)\Psi = 0; \qquad R > 1 \tag{3.53}$$

where $R = r/\rho$ is the normalized radial distance.

In the case of acircular fiber, TE and TM, with circular symmetric fields, can be propagated as in the planar waveguides, because they have electric and magnetic fields that are parallel to the interface, respectively. In terms of local plane waves, or rays, only meridional rays, i.e. those passing through the waveguide axis can preserve the $e_{z,i} = 0$ and $h_{z,i} = 0$ at every reflection [92]. In general, the ray follows an helical or skew trajectory in a circular fiber, that means it is impossible to maintain $e_{z,i} = 0$ and $h_{z,i} = 0$, because the direction of propagation rotates along the ray trajectory. These combinations of TM and TE modes are called hybrid modes (EH and HE modes) [92].

The general solutions for longitudinal field components can be written as [92]:

$$e_z = A\frac{J_v(UR)}{J_v(U)} f_v(\phi) \qquad h_z = B\frac{J_v(UR)}{J_v(U)} g_v(\phi) \qquad 0 \le R < 1 \tag{3.54}$$

$$e_z = A\frac{K_v(WR)}{K_v(W)} f_v(\phi) \qquad h_z = B\frac{K_v(WR)}{K_v(W)} g_v(\phi) \qquad R > 1 \tag{3.55}$$

where *A* and *B* are constants, J_v and K_v are respectively the Bessel functions of the first kind and modified Bessel functions of the second kind relatively to v (v is the Bessel order and can be a positive integer or zero) and $f_v(\phi)$ and $g_v(\phi)$ are defined as:

$$f_v(\phi) = \begin{cases} \cos(v\phi) \rightarrow \text{Even modes} \\ \sin(v\phi) \rightarrow \text{Odd modes} \end{cases} \tag{3.56}$$

$$g_v(\phi) = \begin{cases} -\sin(v\phi) \rightarrow \text{Even modes} \\ \cos(v\phi) \rightarrow \text{Odd modes} \end{cases} \tag{3.57}$$

Finally, the eigenvalue equation for a step-index circular fiber depends on the four modes $TM_{0,m}$, $TE_{0,m}$, $EH_{v,m}$ and $HE_{v,m}$ and are described as (*m* is the root of the eigenvalue equation):

$$\begin{matrix} \text{EH}_{\text{vm}} \text{ and } \text{HE}_{\text{vm}} \\ \text{Modes} \end{matrix} \rightarrow \begin{matrix} \left[\frac{J_v'(U)}{UJ_v(U)} + \frac{K_v'(W)}{WK_v(W)}\right]\left[\frac{J_v'(U)}{UJ_v(U)} + \frac{n_{cl}^2}{n_{co}^2}\frac{K_v'(W)}{WK_v(W)}\right] = \\ = \left(\frac{v\beta}{k_0 n_{co}}\right)^2 \left(\frac{V}{UW}\right)^4 \end{matrix} \tag{3.58}$$

$$\text{TE}_{0,m} \text{ modes} \qquad \frac{J_1(U)}{UJ_0(U)} + \frac{K_1(W)}{WK_0(W)} = 0 \tag{3.59}$$

$$\text{TM}_{0,m} \text{ modes} \qquad \frac{n_{co}^2}{U}\frac{J_1(U)}{UJ_0(U)} + \frac{n_{cl}^2}{W}\frac{K_1(W)}{WK_0(W)} = 0 \tag{3.60}$$

where $V = (U^2 + W^2)^{1/2}$ is the waveguide parameter, J_ν' and K_ν' are the derivate of the Bessel function of the first kind and of the modified Bessel function of the second kind, respectively.

In these two-last sections we described eigenmodes for the step-profile planar waveguide and the step-profile circular waveguide, composed by the core and the cladding. The same technique can be used when, the step-profile planar waveguide is composed of metallic material, the exclusive difference being the complex component of the refractive index of the metal, as shown in Figure 3.5.

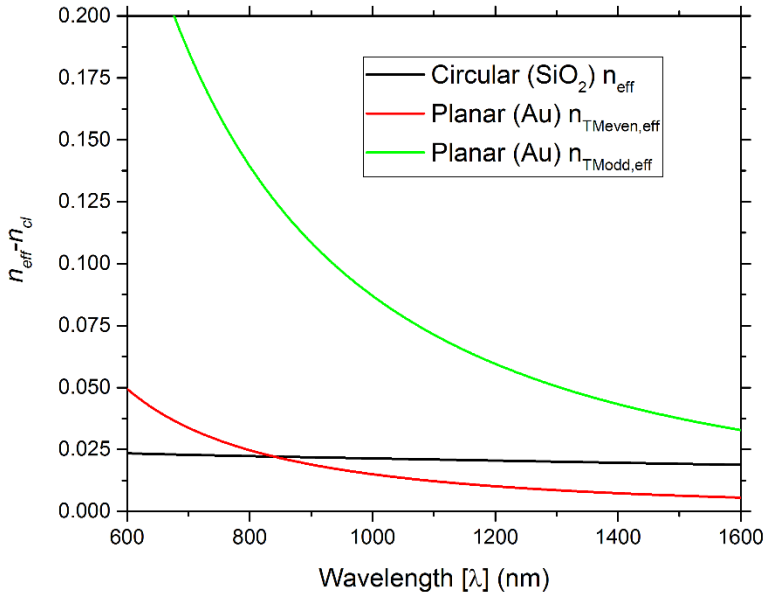

Figure 3.5 Numerical solution of the eigenvalue equation in a step-profile planar composed of gold (Au) and step fiber circular composed of the core (GeO_2-SiO_2) and the cladding (SiO2).

Figure 3.5 shows the numerical solution of the eigenvalue equation in a step-profile planar composed of gold (Au) and two external refractive indices. Also, Figure 3.5 shows the numerical solution of the eigenvalue equation in a circular fiber composed of the core (GeO_2-SiO_2) and the cladding (SiO_2).

3.4 Surface plasmon resonance (SPR)

In this section, we describe the theory of surface plasmon polariton, the importance in the dielectric metal interface, and the types of SPR-based optical fibers sensors.

3.4.1 Theory of the surface plasmon polariton (SPP)

A plasmon is defined as a (quasi-particle) field resulting from oscillations of the free electrons in a medium. The excitation of the surface plasmon polaritons (SPP) [1] results from the coupling of the electromagnetic waves with the oscillations of the free electrons of the metal on the surface between the metal and the external dielectric medium, as shown in Figure 3.6. When the excitation is produced optically the effect is known as SPR [1], [2].

As shown in Figure 3.6a, only modes with TM polarization or modes with an electric field parallel to the metal surface can delocalize electrical charges and then form

localized charge distributions, and obtain the SPR. In Figure 3.6b it can be observed that the maximum amplitude of the field occurs at the interface between the metal layer and the dielectric layer and decays exponentially on both sides of the metal and of the dielectric.

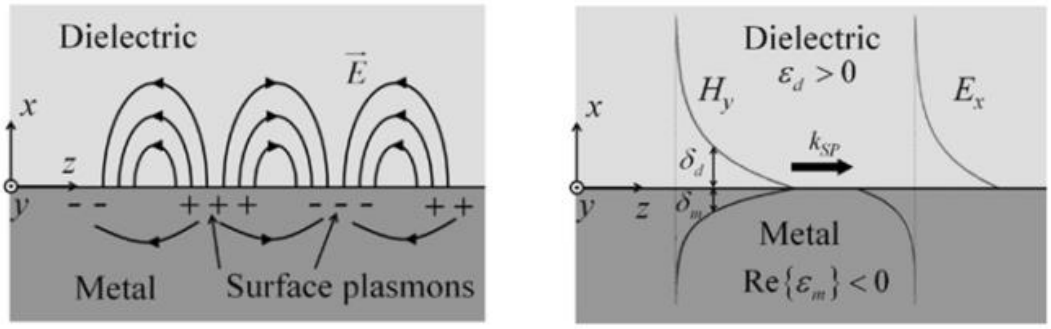

(a) (b)

Figure 3.6 Surface plasmon is propagated along the interface between the metal and the dielectric, where ε_m is the permittivity of the metal, ε_d is the permittivity of the dielectric and the penetration field in each element is given as δ_d and δ_m, for the dielectric and metal, respectively. (a) Lines of the electric field and (b) distribution of electric, E_x and magnetic, H_y, fields, respectively [1].

From equation 3.23 it can be concluded that the plasmon frequency ω_p is a cutoff frequency below which the light wave vector becomes imaginary, indicating that light cannot propagate in the medium. Instead, the light that strikes the surface of the metal is fully reflected, and the electromagnetic field can only penetrate the metal to a small depth. In simple words, below ω_p, metal charges can oscillate with the field, radiating a secondary electromagnetic field, which cancels the incident wave. This effect results in a strong coupling between the oscillation of the plasmon and the electromagnetic field, which results in an excitation, known as the surface plasmon resonance [67], [93]. Above ω_p, the charges move very slowly, unable to keep up with the oscillations of the field and cannot cancel it.

3.4.2 Planar waveguide in a metal and dielectric external interface

As described in the section 3.3.3 for a planar waveguide with core and cladding, we can do the same for interface metal/dielectric (M/D) where the refractive index of the material n takes either the value of the metal n_m or of the external dielectric n_d.

The most simple geometry sustaining SPPs is that of a single interface (Figure 3.6) between a dielectric, non-absorbing half space (x > 0) with positive real dielectric constant ε_d and an adjacent conducting half space (x < 0) described via a dielectric function $\varepsilon_m(\omega)$. The requirement of metallic character implies that Re[$\varepsilon_m(\omega)$] < 0. For metals this condition is fulfilled at frequencies below the bulk plasmon frequency ω_p. We want to look for propagating wave solutions confined to the interface, i.e. with evanescent decay in the perpendicular *x*-direction.

Considering Figure 3.6, using the equations from 3.42 to equation 3.45 and considering only the TM solution, we obtain the equations for both regions of the study [94]. For x > 0:

$$e_z(x) = A\exp\left(j\beta - k_d x\right) \tag{3.61}$$

$$h_y(x) = -jA\frac{n_d^2}{k_d}\sqrt{\left(\frac{\varepsilon_0}{\mu_0}\right)}\exp(j\beta z - k_d x) \tag{3.62}$$

$$e_x(x) = -jA\frac{\beta}{k_d}\exp(j\beta z - k_d x) \tag{3.63}$$

and for x < 0:

$$e_z(x) = B\exp\left(j\beta z + k_m x\right) \tag{3.64}$$

$$h_y(x) = -jA\frac{n_m^2}{k_m}\sqrt{\left(\frac{\varepsilon_0}{\mu_0}\right)}\exp(j\beta z + k_m x) \tag{3.65}$$

$$e_x(x) = jA\frac{\beta}{k_m}\exp\left(j\beta z + k_m x\right) \tag{3.66}$$

where $k_m = \sqrt{\left(-\beta^2 + n_m^2 k_0^2\right)} = \sqrt{p_m}$ and $k_d = \sqrt{\left(\beta^2 - n_d^2 k_0^2\right)} = \sqrt{p_d}$ are the SPP parameters in the metal and external dielectric, respectively. Continuity of the axial electric field at the M/D interface and of the magnetic field parallel to the *y*-direction gives *A* = *B* and:

$$\frac{k_d}{k_m} = -\frac{n_d^2}{n_m^2} \tag{3.67}$$

Solving this condition for the propagation constant of the metal, k_m, and external dielectric, k_D, which have the dispersion relation of SPPs propagating at the interface between the two half spaces [94], such as:

$$k_{sp} = \beta = k_0\sqrt{\frac{n_m^2 n_d^2}{n_m^2 + n_d^2}} \tag{3.68}$$

This equation is also called the propagation constant of the surface plasmon (k_{sp}) at the interface M/D.

The same solution of the TM mode can be applied for the TE mode as shown in [94], but on continuity of the electric field, parallel to the *y* direction and of the magnetic field parallel to the *z*-direction at the M/D interface, leads to the condition:

$$A\left(k_m + k_d\right) = 0 \tag{3.69}$$

Since confinement to the surface requires Re [k_m] > 0 and k_d > 0, this condition is only fulfilled if A = 0, so that A = B = 0. Thus, no surface modes exist for TE polarization. Surface plasmon polaritons only exist for TM polarization [94].

The physical parameters of the metals such as plasma frequency ω_p (equation 3.23) and propagation constant of the plasma k_{sp} cannot be altered. However, from the point of view of sensor design, it is possible to optimize sensor performance by altering the thickness of the metal or by combining different layers of metals and dielectrics. This can be used to control the nature of the plasmon modes obtained in

each interface and their mutual interaction, and in the process customize the sensor response.

3.4.3 Fiber optics sensors based on surface plasmon resonance

The technology evolution began with the Otto and Kretschmann configurations [15], based on a simple prism with a metal layer (gold), and becoming more complex, when including configurations based on: D-type fibers [45], cladding-off fibers [58], end-reflection mirrors [95], tapered fibers [96], photonic crystal fibers [97], fiber Bragg gratings [98], among others. More recently, the development of new fabrication techniques, capable of providing micro and nanoscale metallic structures, have paved the way to the development of new devices that use the localization of surface plasmons to better control their properties and achieve higher sensing performances. These approaches include metamaterials [99], nano and micro structures with different sizes and forms [100], and their combination with other materials, in a myriad of optical devices, including optical fibers [101]. The performance of these devices based on metallic sub-micron structures depends strongly on the fine control and optimization of geometrical parameters such as the dimensions or relative positions of the components, thus promoting numerical simulations as the preferred method to explore new sensor designs and reduce time and development costs [20], [97].

Today, fabrication techniques offer many geometries for the metal components, ranging from wires and disks to spheres and grooved surfaces, which can be used to customize the modal dispersion of the plasmons and increase their coupling with light. In particular, it is possible to couple the modes of a step-index fiber with those of a metallic wire at certain wavelengths, when some of these modes become phase matched. Also, metallic wires support multiple modes which permit an increased number of resonant peaks [102], and result in sensors with different values of sensitivity, operation wavelength and RI detection range, among others [55], [103]. Some new fabrication techniques (like spliced-fiber with pressure-filling [104], stack-and-draw technique [105] or pressure assisted melt filling (PAMF) [106] increased the possibility of the creation of new configurations with more complex geometries allowed to produce virtually any nano-structure on an optical fiber [28], [107].

The fiber-based SPR sensors have a configuration like that of the Otto and Kretschmann configurations, as shown in Figure 2.3. A simplistic way of creating this sensor is to replace the prism with an optical fiber where the cladding is removed through a chemical method [29]. The purpose of eliminating or reducing the cladding is to make the electromagnetic field interact more efficiently with the metal and with the external environment, allowing the evanescent field to propagate to the external medium with greater intensity. The condition of the SPR is when:

$$k_{sp} = \frac{2\pi}{\lambda}\sqrt{\frac{\varepsilon_m \varepsilon_d}{\varepsilon_m + \varepsilon_d}} = \frac{2\pi}{\lambda} n_{co} \sin(\theta) = k_z \tag{3.70}$$

In sections 3.3 we explained a numerical solution to the planar and circular step waveguide. From equation 3.70 and the Figure 3.5 we can conclude that the point of intersection between the solution of the optical fiber and the solution of the two-

planar waveguides based in Au and two external refractive indices (1.34 and 1.38). As shown in Figure 2.4, a small variation of the external refractive index and the SPR effect will imply a variation of the wavelength relative to an external reference refractive index. Then the sensitivity (*S*) and the resolution (*R*) can be calculated with the following equations [28]:

$$S(\lambda) = \frac{\Delta\lambda_{peak}}{\Delta n_{ext}} \tag{3.71}$$

$$R(\lambda) = \frac{1}{S(\lambda)}\Delta\lambda_{min} = \frac{\Delta n_{ext}\Delta\lambda_{min}}{\Delta\lambda_{peak}}, \tag{3.72}$$

where λ_{min} is the minimum value in wavelength between two spectral lines that can be experimentally detected and $\Delta\lambda_{peak}$ is the shift in wavelength of the resonance peak obtained from the simulations for different values of external refractive index (n_{ext}). In this thesis, we assume that it is possible to detect experimentally a spectral variation of 0.1 nm (λ_{min}) [108].

3.5 Finite element method (FEM)

In subsection 3.4.3 it was explained some of the main configurations of the optical fiber sensor based in the SPR. Because of the different types of optical fibers and associated SPR sensor configurations, their actual construction and testing is very costly and time consuming, making simulation programs important tools to obtain a first and fast approximation of the final sensor behavior. The eigenvalue equation explained in sections 3.3 can be a first approximation, but the usual numerical analysis methods are: the expansion and propagation method (MPE) [7], the method for multilayer structure transfer matrix modeling [8], the optical fiber multilayer cylindrical structure [9] and the rigorous couple wave analysis (RCWA) [10]. However, these methods have some difficulties for arrangements with nanostructured irregularities [11].

The full analysis of an optical fiber sensor based in SPR may combine the study of multiple modes inside the fiber [109], multiple modes in metallic wires [97], and simultaneous sensing of the external refractive index and temperature [107] [110], which may result in a complex study with multiple nanostructures, modes and materials. However, for many realistic device designs, it is difficult to compute the hybridization mode by ordinary analytical techniques. Thus, numerical schemes must be used to optimize those optical devices. For that, the need of more complex simulation tools using finite difference time domain (FDTD) and finite element methods (FEM) are crucial [12].

The advantage of using numerical methods of analysis is that they allow solving problems where the geometry of the structure is important whether it is micro- or nanostructured. In these cases, the planar method cannot be used, or is not a good approximation. On the other hand, numerical methods of analysis make it possible to carry out studies of the intensity of the electric and magnetic fields throughout the structure, to have a graphical environment, 3D simulations, among other advantages.

The disadvantage of this type of system is the high consumption of computing memory, which leads to a high processing time.

FDTD consists of solving partial differential equations in the time domain, being easier to understand and it is a more commonly used method to solve basic problems. For example, for simple structures, FDTD is easier to implement than FEM. The calculation of the partial differential equations (PDEs) using FEM is based on the construction of sub-elements within the structure to be studied (mesh). In this structure, the calculations of the field equations are represented discreetly in a system of algebraic equations and are solved by an eigenvalue method. The FEM are usually used when it is necessary to vary the resolution by which the field is described over different regions of the simulation box, since other methods (such as FTDT) would render the computational problem too large. The drawback in using the FEM is that to obtain a smaller computational problem, the method to reduce the PDEs to a system of algebraic equations is much more complex.

The study, calculation and implementation of the FEM was carried out in COMSOL Multiphysics and we completed the study using MatLab as an interface and for quick calculation, as shown in Figure 3.7. This figure represents a basic schematic of the computational approach used in this work.

The MatLab starts the simulation defining the design we want to study. COMSOL Multiphysics allows the design of the different components in different dimensions: 3D, 2D and 1D, symmetric or asymmetric, to reduce the number and size of the elements (mesh). In this work, the design was conducted in 2D, due to the high processing time required to use 3D. Then, we select and choose the parameters we want to study in the design, for example, the size of the core, the cladding, the metal type and shape, the type of overlayer, among others.

COMSOL Multiphysics has multiples modules with different tools for each module. In this work, we used the RF module, the physics module called electromagnetic waves frequency domain. This module allows the study of radio frequency comprising physical parameters for the study of high frequency magnetic and electric fields, Poynting vector, parameters of the materials, among others, using Maxwell's equations. The wave equation used by COMSOL Multiphysics is represented in equation 3.15, when the electric displacement field is based on the model of the relative permittivity. But in section 3.2 we demonstrated the equation can be written as a function of the refractive index $\varepsilon_r = (n - ik)^2 = \tilde{n}^2, \sigma = 0, \mu_r = 0$ (and equation 3.15 is written then:

$$\nabla \times \nabla \times \boldsymbol{E}(\boldsymbol{r}, \omega) - k_0^2 \left(\tilde{n}^2(\boldsymbol{r}, \omega)\right) \boldsymbol{E}(\boldsymbol{r}, \omega) = 0 \tag{3.73}$$

Also, in COMSOL it is possible to define the different optical properties of the materials like the electric component (permittivity), magnetic component (permeability), dispersion, and conductivity. These properties can be defined through a equation defined by the user, using the models predefined by the program (Lorentz and Drude) or using materials predefined in COMSOL.

Finally, a good choice of mesh is critical in FEM since it determines the quality of theresults of the simulation, and many times it is necessary to repeat the simulations to adjust the mesh. A good approach is to use smaller elements in regions where the

fields have a sharper variation. On the other hand, a smother variation of the field can be sampled by larges elements.

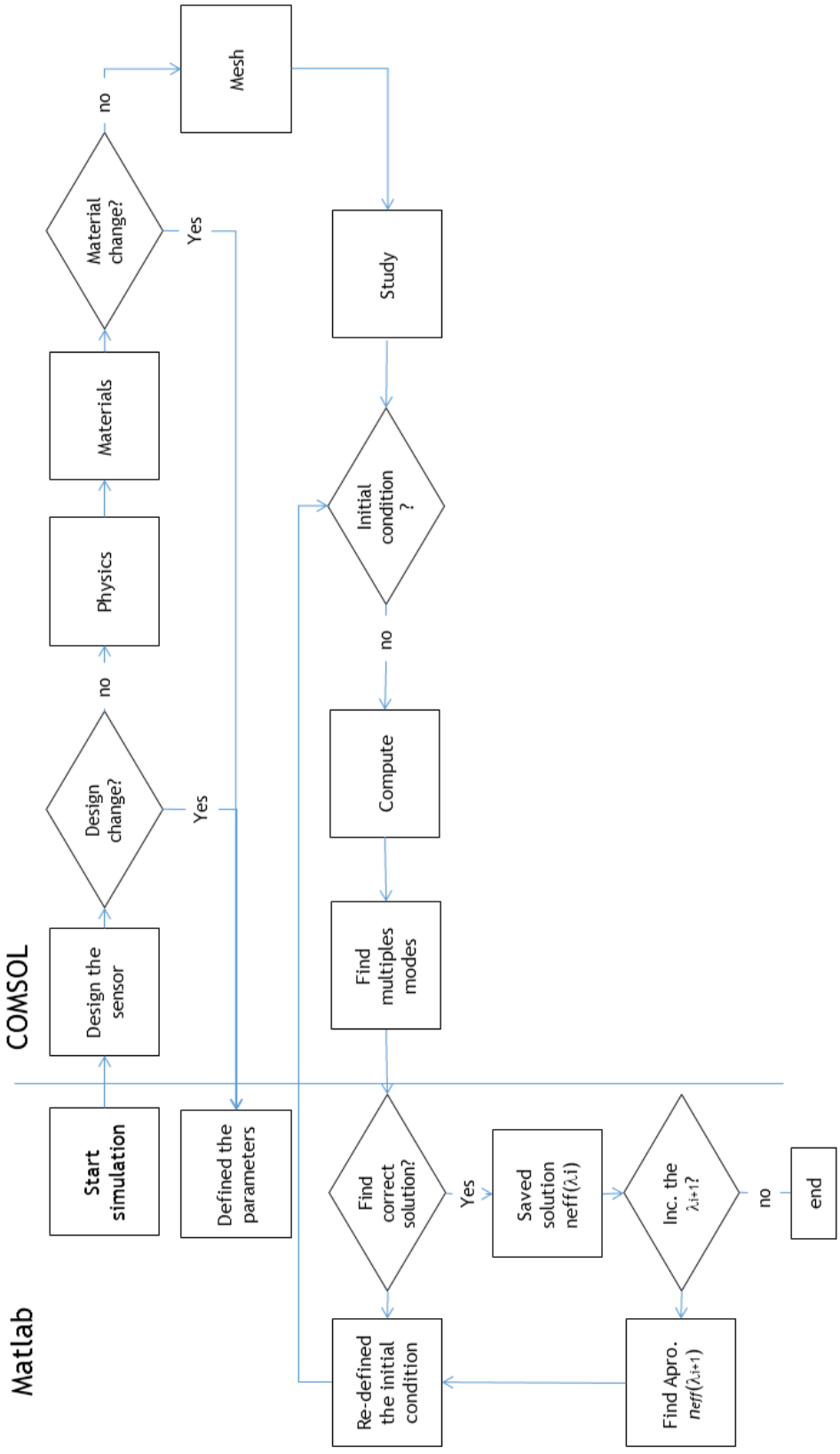

Figure 3.7 Basic scheme of computational simulations used in this work.

In short, the quality and validity of the numerical results is strongly dependent on the mesh used. The choice depends on the balance of two factors:

1. Reduction of the numerical error due to rounding and respective propagation during the calculation, which is obtained for meshes with fewer elements and, consequently reduces the number of calculations in the simulations.
2. Reduction of methodological error associated with the finite element method, which is achieved using more samples of the field, which requires grids with more elements. However, there are drawbacks to choosing meshes with many elements as this increases the complexity of simulations, requiring more computational resources and more time to perform calculations.

The balance between these two sources of error (numerical and methodological) is achieved by selecting grids where there is a denser sampling of the field (smaller finite elements) in areas where the field has larger variations and lowering the sampling in areas where field is approximately constant or zero.

We computed the model in COMSOL and obtained several preliminary solutions. These initial solutions are then exported to MatLab where we have automatized the program to find the more thorough solutions, by solving the mathematical problem defined between equations 3.31 to 3.70 in the sections 3.3 and 3.4. If the solution cannot be found, we redefine the initial condition and compute again in COMSOL. If we find the correct solution or mode, we save the information and increment the value of the wavelength. The new initial approximation is calculated using Newton's method, a mathematical technique to approximate solutions for non-linear equations and systems of equations. We repeat this process until we obtain the results as function of the wavelength.

Chapter 4 Singlemode sensors with thin metal films

The previous chapters reviewed the fundamental physical principles and models that support the operation of SPR sensors and summarized the main sensor configurations, including their structure and components, as well as their applications and methods of detection. Although the basic physical principles behind the SPR phenomenon are well understood, their optimization towards better sensing designs is not trivial, specially in sensors with complex structures, combining components with different types of materials, in particular if one wishes to consider realistic models of their optical properties. For example, real metals and dielectrics are described by complex dispersion and absorption curves over the wavelength operation range of the sensors. This imposes the use of numerical methods of analysis to compute the optical and plasmonic modes supported by the sensors and their impact on sensor performance.

In this chapter we use a computer model based on FEM implemented in COMSOL Multiphysics to simulate and optimize the operation and performance of different SPR sensor configurations based on single mode D-type fibers with thin metal films. This model incorporates most of the phenomenological aspects and reproduces the results described in literature. In particular, we verify the fundamental physical principles behind SPR, from the conditions for the occurrence of SPR, the behavior of the electric and magnetic fields, to the distribution of the Poynting vector in the interface between the dielectric and the metal, among others. We also study the different parameters that affect the performance of SPR optical fiber sensors, with particular emphasis to the thickness of the metal film and other material layers, and the relative position of the components of the sensor.

This chapter is also focused on improving the performance of one of the sensor configurations most commonly described in the literature, namely SPR sensors based on single mode D-type fibers with thin metal films, by incorporating a distribution of holes in the structure of the fiber that promotes the interaction between the single guided mode in the core of the fiber with the plasmon modes supported by the metal film. This distribution of holes can operate as a scattering structure that enhances the optical intensity on the metal, or even forms a photonic crystal that traps light at the center of the fibre (the fibre is in fact a D-type PCF), allowing this light only to escape in the direction of the metal film. We consider the enhancements in sensitivity, in the resolution, in loss and in operational wavelength range of the sensors. This configuration establishes a reference to the following chapters, where we present

other variations of this basic sensor by exploring other degrees of freedom in sensor design.

4.1 SPR sensor based on conventional D-type fiber

The conventional D-type fiber sensor is one of the many configurations studied in literature, with multiple applications including gas detection [111], curvature sensing [112], temperature and refractive measurement [113]. These sensors are based on a fiber that is highly birefringent, where the linear polarization states are structurally maintained [44] and the detection of the external medium refractive index is based on its interaction with the evanescent field of the light that travels in the optical fiber [113]. These characteristics of the D-type fiber are very interesting for sensing and they can be even further optimized when combined with SPR. The combination of these technologies results in refractive index sensors with a sensitivity of 1×10^{-7}, much higher than the refractive index sensor configuration that uses only the D-type fiber [19]. Moreover, the SPR D-type fiber sensor has been also implemented as a biosensor [114], [115].

4.1.1 Numerical mode analysis

In order to optimize the SPR D-type fiber sensor, it is crucial to fully characterize the behavior of light inside the waveguide and its interactions with the metal film that create the SPR phenomenon. As described earlier in this thesis, we developed models based on the finite element method which is described in section 3.5. The considered sensing configuration studied in this work, are shown in Figure 4.1. Figure 4.1 illustrates the configuration of the conventional D-type optical fiber with a metal film deposited on the flat D-type fiber surface. The analysis of this structure as a SPR fiber sensor is one of the most commonly studied in the literature [1].

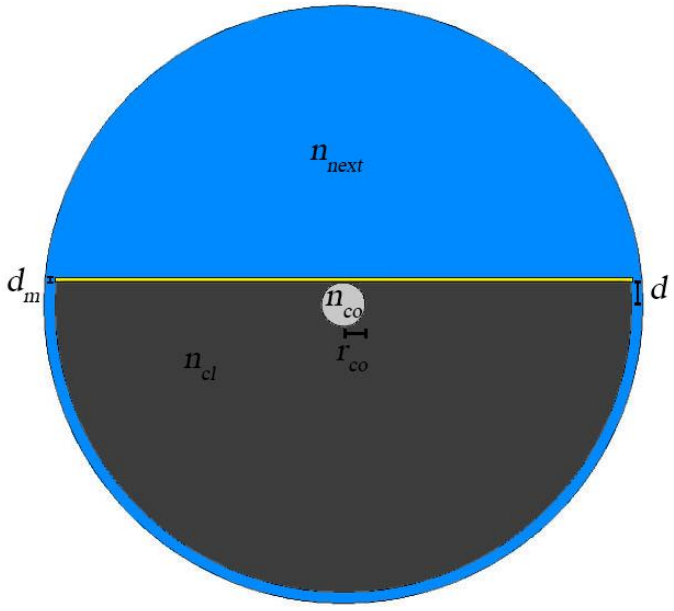

Figure 4.1 Schematic of the SPR D-type sensor. The fiber is composed by two refractive indexes (core - n_{co} and cladding - n_{cl}) then a metallic layer is deposited with thickness d_m and refractive index n_m, at a distance d of the center of the fiber, for the measurement of the external refractive index n_{ext}.

The fiber is formed by a core and a cladding with refractive indexes, n_{co} and n_{cl}, respectively. The fiber has a D-type profile, where a metallic layer, with a refractive index n_m deposited in the horizontal surface. It is assumed that the space outside the fiber is filled with the analyte medium to be studied, having a refractive index of n_{ext}. The distance between the center of the fiber and the gold layer is denoted by d (residual cladding) and the thickness of the gold layer by d_m. The refractive indexes of the dielectric materials were alculated using the Sellmeier equation 3.25, whereas that of the metal was obtained from the Drude model (equation 3.27).

The next step was the creation of the mesh, which basically consists in dividing the simulation domain into smaller subdomains; as shown in Figure 4.2. The subdomains have different sizes and are smaller near the interfaces between different media, to account for steeper variations of the electromagnetic field. The field equations were then discretized into an algebraic system of equations and solved for their characteristic eigenvalues.

The numerical mode analysis provided by COMSOL allows us to find the solution of the eigenvalues for our configuration, through the definition of the wavelength, number of modes and initial approximation. The initial distribution of the field used by COMSOL to iterate the solution of the problem is set to be identical to the fundamental mode, calculated analytically for the fundamental mode of the core of the fiber.

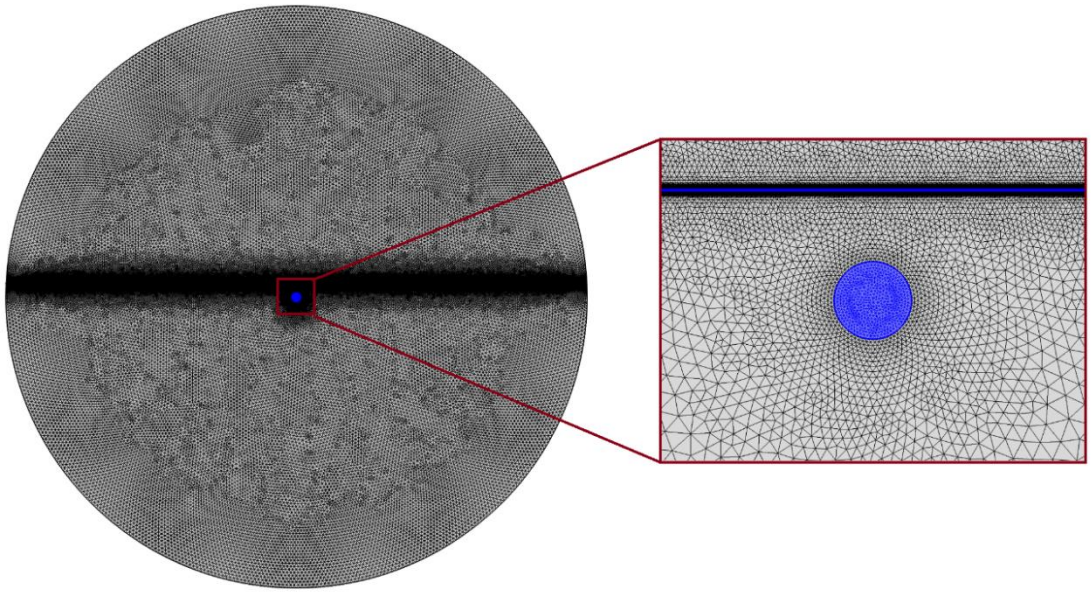

Figure 4.2 Structure of the finite elements in COMSOL for a D-type optical fiber with a metallic layer for SPR. The elements are smaller in the metallic layer and in the core.

In **Erro! A origem da referência não foi encontrada.** we studied the calculation of the modes in isolated waveguides. However, SPR sensors combine several of these waveguides integrated in the structure of an optical fiber. Therefore, it is necessary to understand how the modes supported by the different waveguides couple and determine the optical response of the sensor. The strongest coupling occurs when the dispersion curves of the different waveguides cross, as shown in Figure 4.3. At these crossing points, occurs a strong hybridization of these modes, resulting in the so called supermodes (SMs). An approximated method of calculating the supermodes can be found in reference [116].This approximation is poor because it does not consider how

these waveguides are integrated in the overall structure of the optical fiber and how the latter influences the coupling between the modes. In Figure 4.3b we show the results of the loss curves, resulting from the hybridization of the modes whose dispersion curves are described in Figure 4.3a. By changing the external refractive index, the crossing point of the two dispersion curves changes, thus, shifting the maximum loss peak in wavelength, as shown in Figure 4.3b.

These SMs can be also calculated more accurately using COMSOL, but with and increase of the time of computation and calculation complexity, in comparison with the method referred in section 3.3. The calculation of the properties of the SM using COMSOL are also shown in Figure 4.3, but for this case are practically indistinguishable from the results using the previous method.

Figure 4.4 illustrates the intensity of the Poynting vector using the study Mode Analyses from COMSOL, for the structure of Figure 4.1, considering a metallic layer, in this case a 45 nm thickness gold layer and the mesh of Figure 4.2 with no resonance (Figure 4.4a)) and in resonance (Figure 4.4b)). The study allows confirmation of the single-mode behavior propagation in the optical fiber in the interaction with the metal. Also, these figures allowed to observe some of the conditions of the SPR, for example, the coupling between the fundamental mode of the fiber and the metal mode, which is denoted by the loss of light in the center of the core. The maximum intensity on the center of the core goes from 372 Wm^{-2} (Figure 4.4a) to 158 Wm^{-2} (Figure 4.4b), while at the same time is observed an increment of the light energy in the interface between the metal and the external medium.

Another important parameter for the SPR is the polarization. SPR occurs when the electric field is perpendicular to the surface of the metal or the magnetic field is parallel to the surface of the metal (TM modes). The blue lines indicate the polarization and we verified that the TM mode, in fact, produced the SPR and not the TE mode.

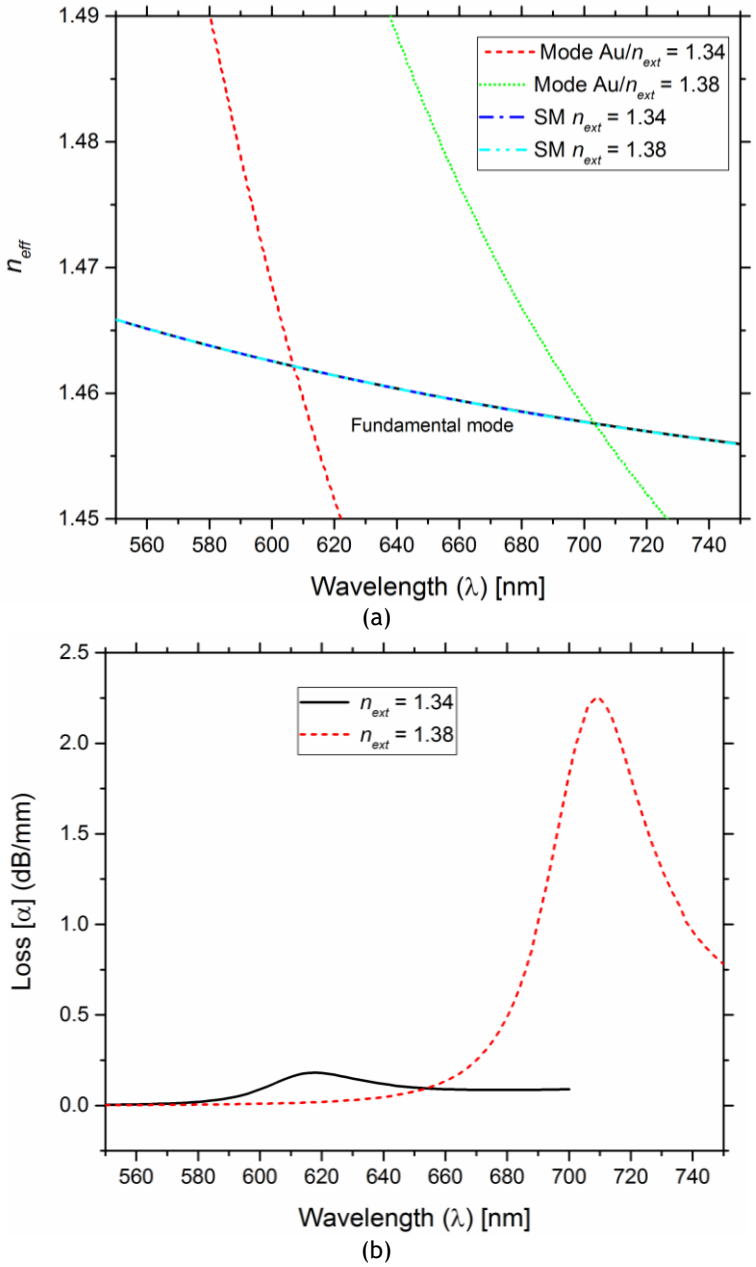

Figure 4.3 (a) Refractive index as function of the wavelength of the modes when considering insolated waveguides for the fundamental mode fiber type D (solid black) and for the plasmonic mode in the interface Au and n_{ext} = 1.34 and n_{ext} = 1.38 (dashed red). The found SMs are represented in dot-dashed blue and dot-two-dashed, respectively. (b) Attenuation in function of the wavelength for the SMs with different external refractive indexes. The thickness of the gold is d_m = 45 nm.

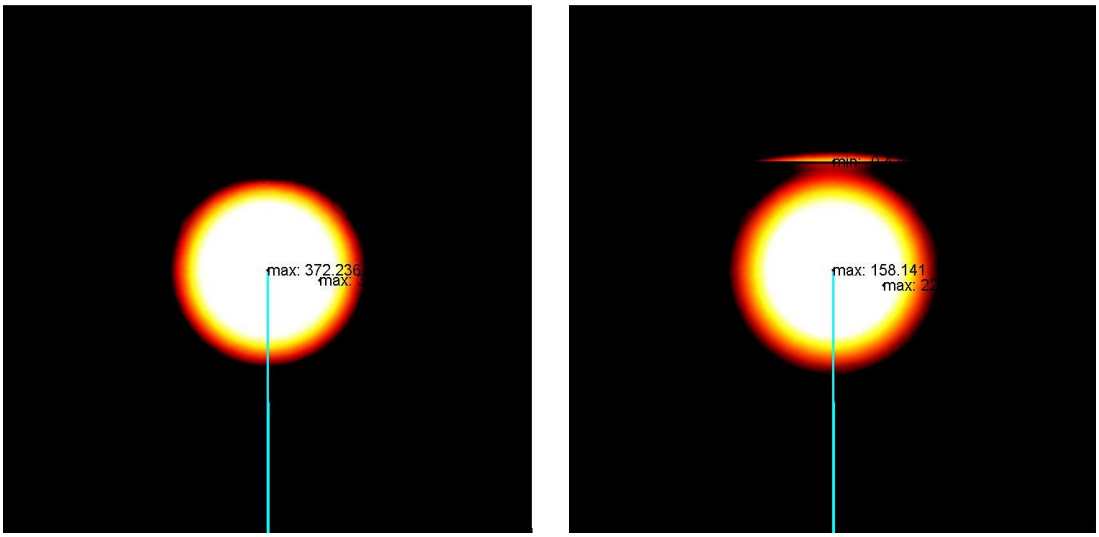

Figure 4.4 Poynting vector distributions in 2D near of the fiber core and the interface metal, with a thickness of metal d_m = 45 nm and an external refractive index n_{ext} = 1.34. The blue lines indicate the transverse electric field e_x and e_y. (a) No resonance λ = 500 nm. (b) Resonance λ = 630 nm.

Another tool of COMSOL permits the study of the field across the transversal section. For example, we can do the study of the normalized 1D Poynting vector amplitude across the fiber core, as shown in Figure 4.5, for different wavelengths.

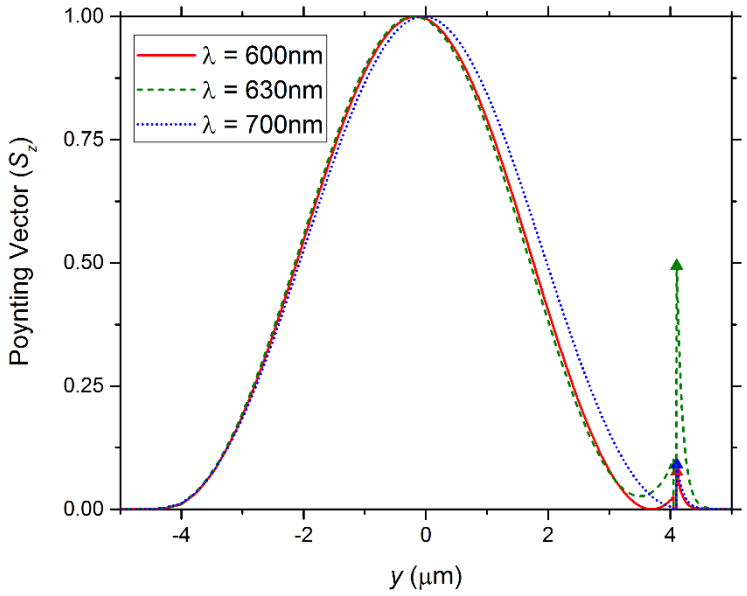

Figure 4.5 Normalized Poynting vector amplitude along a cutline across the fiber core for different values of the wavelength, with the thickness of metal d_m = 45 nm and external refractive index n_{ext} = 1.34.

Comparing the curves, it is possible to see the intensity of the light in the external medium is stronger when the wavelength is close to the resonance peak (around 630 nm). We also observed that the intensity of the light inside of the metal is 0 for all wavelengths and for that wavelengths close to the resonance, the maximum of the Poynting vector occurs in the interface between the metal and the external medium. We also verified that the mode propagating in the center of the fiber corresponds to the fundamental mode. These conditions have also been verified in each simulation (each wavelength) using MatLAb and confirmed by Figure 4.4 and Figure 4.5.

4.1.2 Algorithm using Fresnel laws

To confirm that the method works properly, it was compare with the results obtained in reference [46] which employed the method for multilayer structure transfer matrix modeling, based on Fresnel equations applied to the structure of Figure 4.1, allowing the transmission intensity to be written (for four layers) as:

$$T = \left| r_{1234} \right|^{L / r_c \tan(\theta)} \tag{4.1}$$

where r_{1234} is the reflective coefficients for four layers, which and can be written as:

$$r_{1234} = \frac{r_{12} + r_{234} \exp\left(j2k_2 d \right)}{1 + r_{12} r_{234} \exp\left(j2k_2 d \right)} \tag{4.2}$$

where the reflective coefficients for three layers and two layers are, respectively:

$$r_{234} = \frac{r_{23} + r_{34} \exp\left(j2k_3 d \right)}{1 + r_{23} r_{34} \exp\left(j2k_3 d \right)} \tag{4.3}$$

$$r_{ij} = \frac{n_i^2 / k_i - n_j^2 / k_j}{n_i^2 / k_i + n_j^2 / k_j} \tag{4.4}$$

and where k_i is the component of the wave vector on the interface of the two layers of the sensor in the direction z and is given as $k_i = k_0 \left(n_i^2 - n_1 \sin^2 \theta \right)^{1/2}$, where n_1, n_2, n_3 and n_4 represent the refractive index of the core, cladding, metal and external test medium, respectively.

Equation 3.36 can be written as function of the transmission (*T*) as

$$T = \exp\left(-\alpha L \right) \tag{4.5}$$

Applying the equations 4.1, 4.5 and considering *L* = 1mm it is possible to obtain the results by the two different methods, as shown in Figure 4.6. The behavior of the two methods is similar, with the difference in the transmission coefficients and a small shift in the wavelength dips. We attribute this difference to the fact that in the method based in the Fresnel equations are only considered planar waves in a fairly symmetrical arrangement. On the other hand, when using FEM, we consider the D-type fiber as a non-symmetrical cylindrical waveguide, being able to model the inhomogeneous optical regions with a resolution of the cell size, resulting in a more accurate outcome. In terms of the results and in what concerns the material thickness, the optimal point is when a layer of 55 to 65 nm is used.

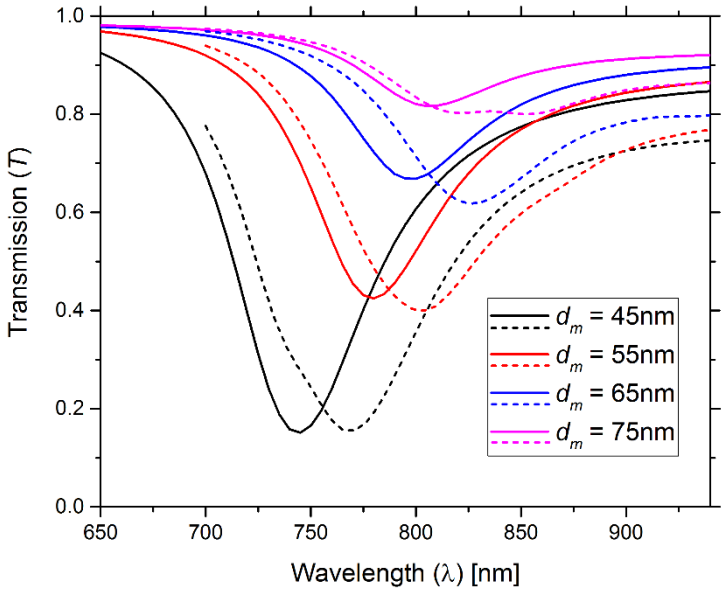

Figure 4.6 Transmission (*T*) as a function of wavelength for a SPR D-type fiber by two methods: The Fresnel method (solid line) and using the FEM method (dash line) with different thicknesses of the gold (Au), d = 4.0 μm, n_{ext} = 1.392 and θ = 88.85°.

Tailoring the simulation analysis in COMSOL, it is possible to optimize the sensitivity, transmission coefficient dip, wavelength operation area, amongst others for a refractive index D-type fiber optic SPR sensor. To decrease the depth of the transmission coefficient dip, and consequently lowering the sensitivity of the external medium, d can be increased, as is shown in Figure 4.7.

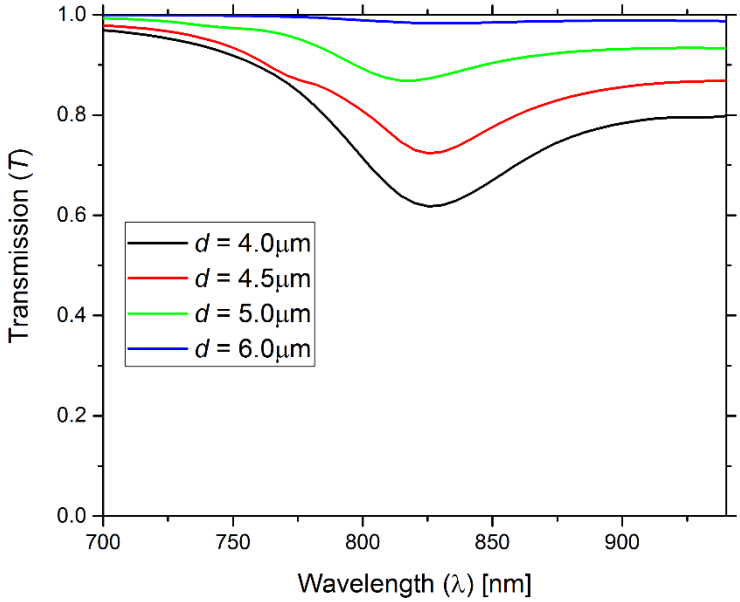

Figure 4.7 Simulation of the transmission coefficient of the sensor, for different distances between the center of the core and the metal (d). In this simulation, the thickness of the gold layer is 65 nm and the refractive index of the external environment is 1.392.

From Figure 4.6 it is possible to have an SPR sensor that works in an operation area near 830 nm, for a metal thickness of 65 nm (Au). Finally, to understand the efficiency of the sensor we study the behavior of the SPR sensor for two different external refractive indexes, as shown in Figure 4.8.

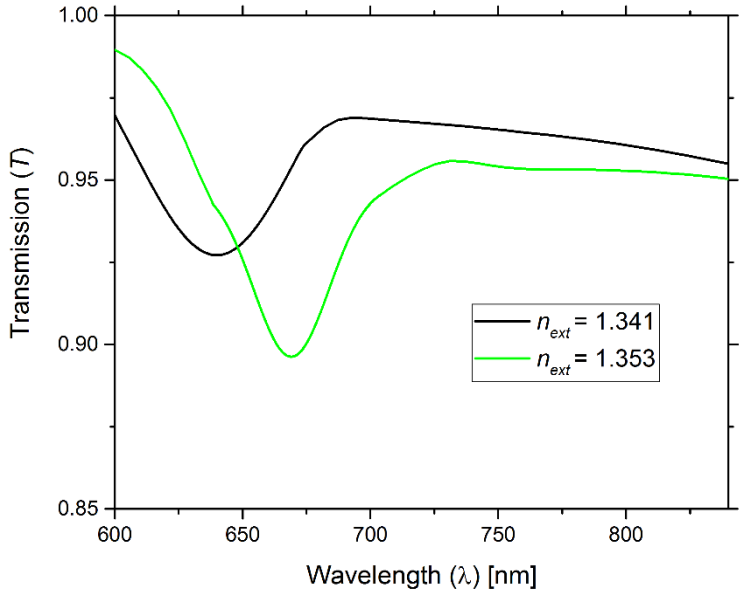

Figure 4.8 Transmission as function of wavelength for two values of external refractive index, where d = 4.0 μm and d_m = 65 nm.

In this way we can calculate the sensor sensitivity, λ/RIU, through equation 3.71 as a function of the different refractive indexes of the external environment, and compare the method with the results found in the literature. The resulting sensitivity of 2542 nm/RIU is close to the sensitivity of 3150 nm/RIU found in [68] with an overlayer of tantalum pentoxide (Ta_2O_5).

In case another operation wavelength is required, one possible solution is to apply an additional layer of a dielectric with a high refractive index, such as tantalum pentoxide (Ta_2O_5) [1], [68] whose simulation results can be seen in Figure 4.9 and compared with the results presented in reference [68]. For different thicknesses of Ta_2O_5 (d_{ov}), the transmission coefficient dip of the sensor is not significantly altered, being possible to tailor the sensor operation wavelength [68]. We also observe from Figure 4.9 that for n_{ext} = 1.329 with a overlayer thickness d_{ov} = 25 nm. The wavelength of the operation is in the 850 nm region, where in Figure 4.6 the SPR sensor with the same thickness of the metal (d_m = 65 nm) but without overlayer the wavelength of the operation was 820 nm, but with a higher external refractive index (1.392).

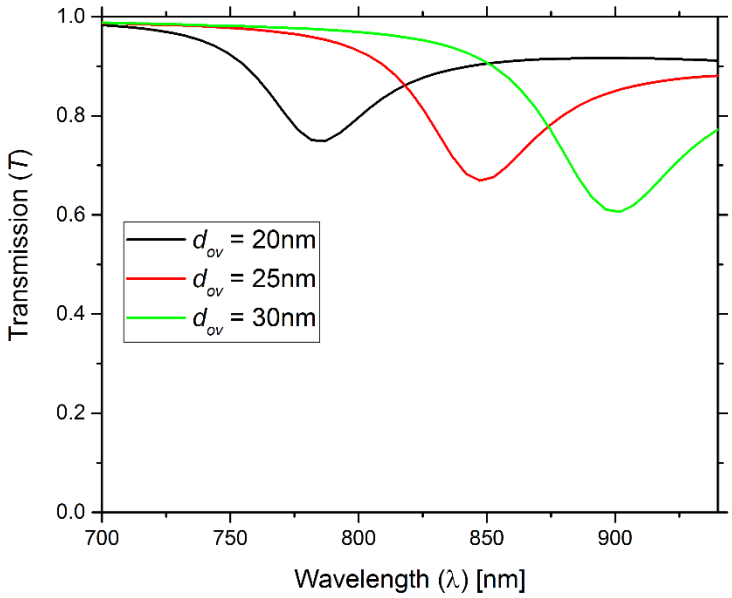

Figure 4.9 Simulation of the transmission coefficient *T* of the sensor for different thicknesses of the dielectric (Ta_2O_5). The thickness of gold is 65 nm and n_{ext} = 1.329

The Ta_2O_5 overlayer allows us to shift the operation wavelength of the sensor, as shown in Figure 4.9. In order to study the sensitivity of the sensor with this overlayer, Figure 4.10 shows the variation of the transmission as a function of wavelength for different external refractive indexes.

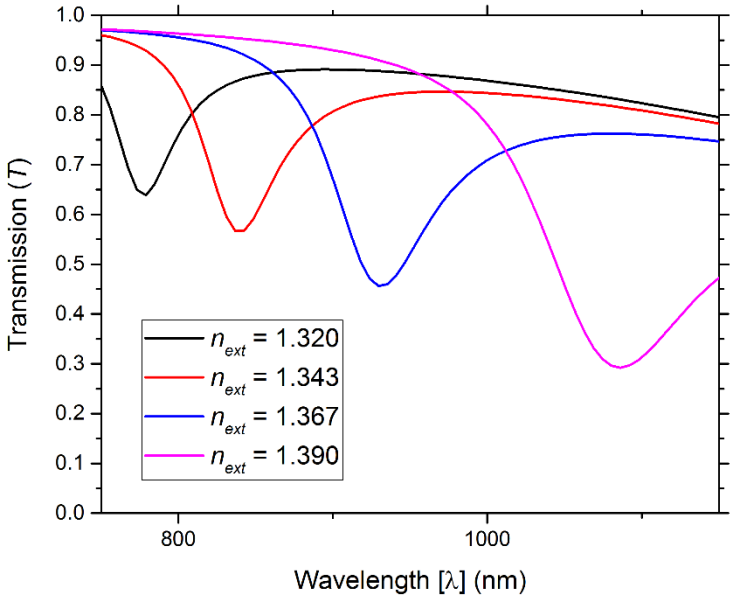

Figure 4.10 Transmission coefficient *T* of the sensor with different dielectric (Ta_2O_5) thickness d_{ov} = 20 nm. The thickness of gold is 65 nm.

From Figure 4.10 and equations 3.71 and 3.72, we can calculate the sensitivity and resolution of the sensor, as shown in Table 4.1. The usage of the Ta_2O_5 overlayer not only produces a shift to higher operation wavelengths in the sensor, it also produces an improvement in the sensitivity. This sensitivity is close to the obtained in [68].

Table 4.1 Sensitivity, resolution and wavelength operation range values for the refractive index SPR optical fiber sensor based on conventional D-type fiber with an overlayer of Ta_2O_5 with a thickness of 20 nm.

	Sensitivity (nm/RIU)	Resolution (RIU)	Range λ (nm)
Range of n_{ext}	**Overlayer Ta_2O_5 d_{ov} = 20 nm**		
[1.320,1.343]	2.652×10^{3}	3.770×10^{-5}	778-840
[1.343,1.367]	3.913×10^{3}	2.556×10^{-5}	840-930
[1.367,1.390]	6.783×10^{3}	1.474×10^{-5}	930-1068

In Figure 4.6 the two simulations, one with COMSOL and the other with Fresnel's equations, present a similar behavior. Also, the simulation in COMSOL has the ability to model inhomogeneous optical regions with a resolution of the cell size and allows the analysis of other parameters such as the intensity of magnetic and electric fields across the structure [117]. On top of that, COMSOL permits in a graphical environment more accurate and realistic results than traditional approaches, although at the expense of longer running times.

Thus, we can use COMSOL to improve the performance of a refractive index SPR D-type optical fiber sensor, where the characteristics of the material layers, in terms of type and thickness, and the residual fiber cladding thickness can be optimized, as shown in the following section.

4.2 Optimization of the microstructured D-type fiber sensor based in SPR

The geometry of the SPR sensors in optical fibers is more complex than the Otto and Kretschmann configurations [1] where a beam of light is focused directly on the thin metal layer. Instead the distribution of light inside the fiber depends on the optical modes allowed by the shape and dimensions of the fiber, which do not necessarily provide higher intensities on the metal layer and strong excitation of the surface plasmon. As a result, the sensitivity of the sensor is far from optimal. So far, most of the studies or optimization of SPR sensors in optical fibers rely on geometrical optics and use a model based on transference matrices, developed for multilayer planar sensors [71], and are mainly concerned with the fine tuning of the resonance frequency of the plasmon to the operational frequency or wavelength of the device by optimizing the metal thickness and adding supporting layers. As we have shown in [45], this approach has strong limitations since it does not take into account the modal structure of the fiber, and consequently the intensity profile that actually reaches the metallic layer. As a result, using the transference matrix approach, there is an overestimating assumption that all the light shines on the metal surface, and also it disregards how a particular fiber mode adjusts to the presence of that layer. Empirically, we can expect a sensor to be more sensitive if, at the resonance frequency of the plasmons, most of the light inside the fiber can be tunneled through the metal

into the exterior medium. In principle this can be achieved not only by adjusting the geometry and constitution of the multilayers that separate the core and the exterior, but also by introducing structures inside the fiber that scatter the light and change the spatial structure of the modes towards the exterior of the fiber.

In this section, we present two new microstructured D-type fiber configurations for refractive index measurement based on SPR. The two new fiber configurations aim to increase the electromagnetic field in the sensing zone and therefore the sensitivity of the sensor in relation to variations of the refractive index of the external medium.

4.2.1 Triangular and parabolic SPR D-type fiber sensor

The conventional D-type fiber was compared with the two new configurations (Figure 4.11a and Figure 4.11b). The conventional D-type fiber is based on a singlemode configuration (r_{co} = 4.0 μm and r_{cl} = 62.5 μm) where the cut of the fiber is placed at d = 4.0 μm, the index of refraction of the core is n_{co} = 1.450 and for the cladding is n_{cl} = 1.442. The thickness of the metal is d_m = 65 nm. The holes in the new configurations have the goal to create an optical mirror that reflects the light into the external medium. In the first new configuration, the cladding holes of the microstructured D-type fiber are placed in a triangular arrangement, while in the second configuration, they are placed in a parabolic arrangement (Figure 4.11a and b, respectively).

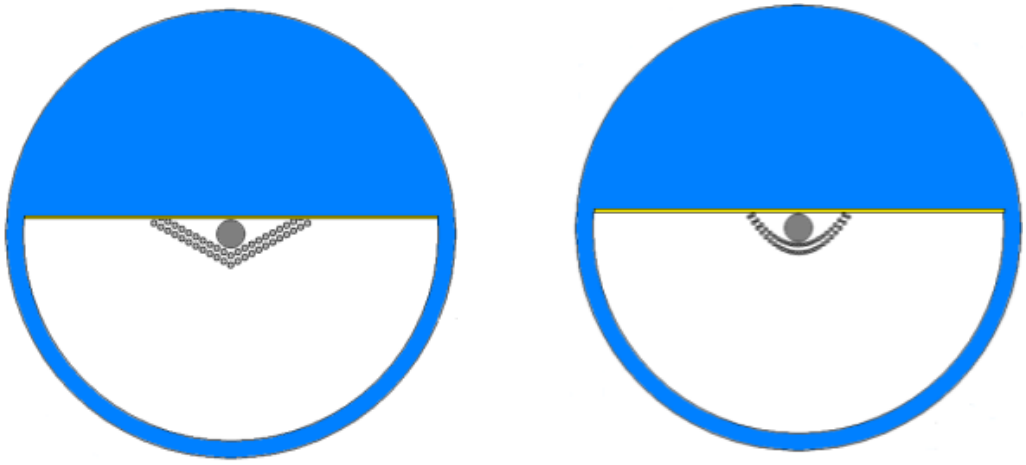

(a) (b)

Figure 4.11 D-type optical fiber (a) holes in a triangular configuration and (b) holes in a parabolic configuration.

Using Equation 3.73 with the FEM in a defined structure, we can obtain the field equations, which are discretized into an algebraic system of equations and then solved for their characteristic eigenvalues. To determine the optical performance of the two new proposed configurations, the electric field intensity in the external medium is evaluated, as shown in Figure 4.12.

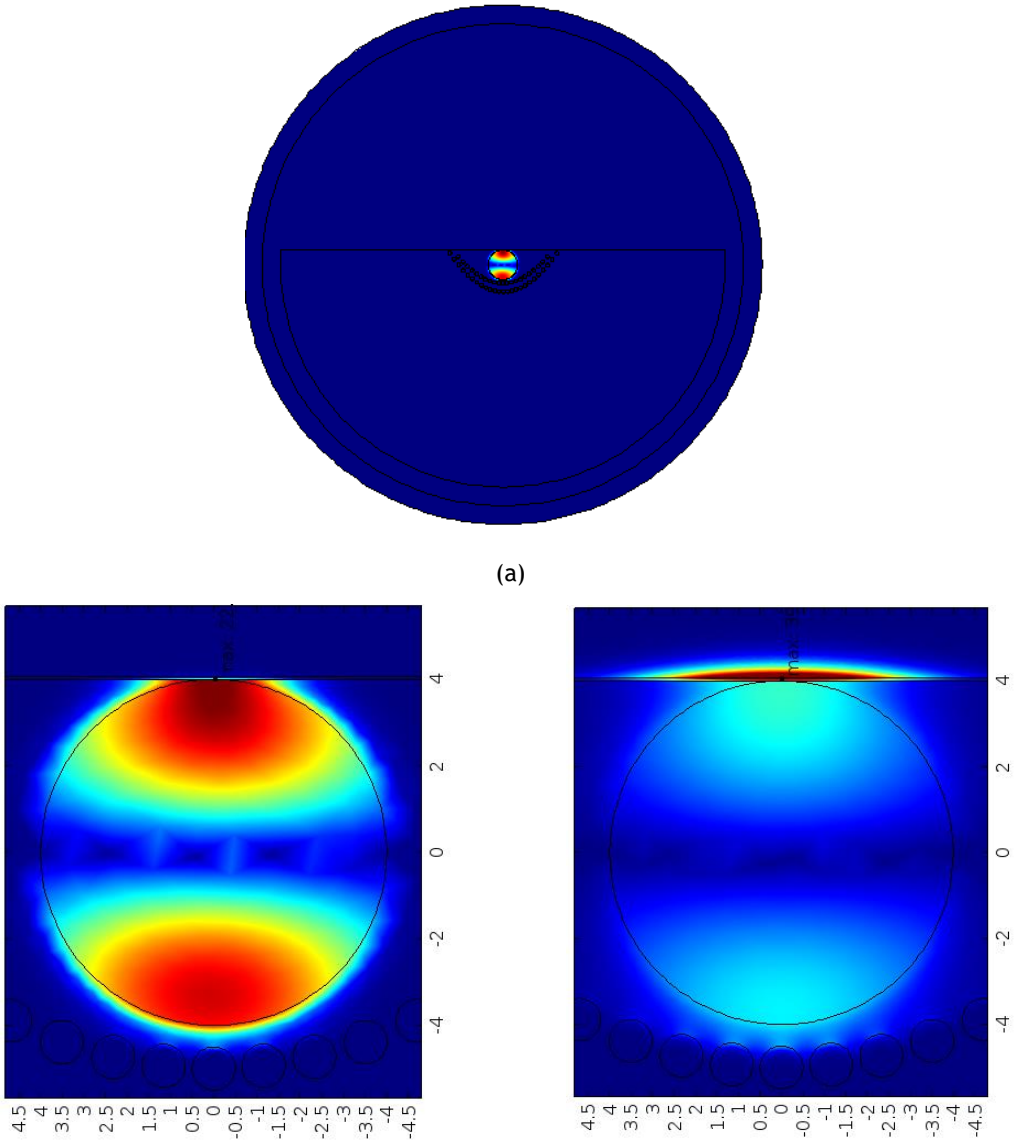

(a) (b) (c)

Figure 4.12 (a) Intensity of the electric field E_z in 2D (V/μm) with λ = 300 nm, d_m = 65 nm and n_{ext} = 1.37. (b) and (c) Zoom of the core of the intensity of the electric field E_z in 2D (V/μm) with: (b) λ = 300 nm, no SPR present and (c) λ = 660 nm, with SPR.

Figure 4.12a shows the intensity of the electric field z (E_z) in 2D for the parabolic configuration, without SPR (λ = 300 nm). In Figure 4.12b, also for the case without SPR (λ = 300 nm), a zoom of the intensity of electric field in the fiber core shows the electric field is concentrated in the core and vanishes quickly in the external medium. In the case of Figure 4.12c, where SPR occurs (λ = 650 nm), the core zoom shows that the maximum of the intensity of electric field occurs in the transition metal-dielectric (M/D) and the energy is concentrated in the interface of the metal-dielectric and on the external medium. These results clearly show the physical effect of the SPR in an optical fiber, where at specific resonant wavelengths, dependent on the refractive index of the external medium, the metallic film becomes in practice transparent, as light is tunneled from the core to the exterior, thus increasing dramatically the losses of the fiber, due to the occurrence of the SPR effect.

4.2.2 Microstructured D-type fibers: intensity of electric field and transmission coefficient

Figure 4.13a presents the intensity of the electric field z (E_z) in the following zones: core, thin metal layer and external medium in 1D dimension, for each configuration. This figure shows that the maximum of E_z occurs in the interface M/D and the intensity in the triangular configuration is stronger in comparison to the other two configurations (parabolic and conventional D-type optical fibers).

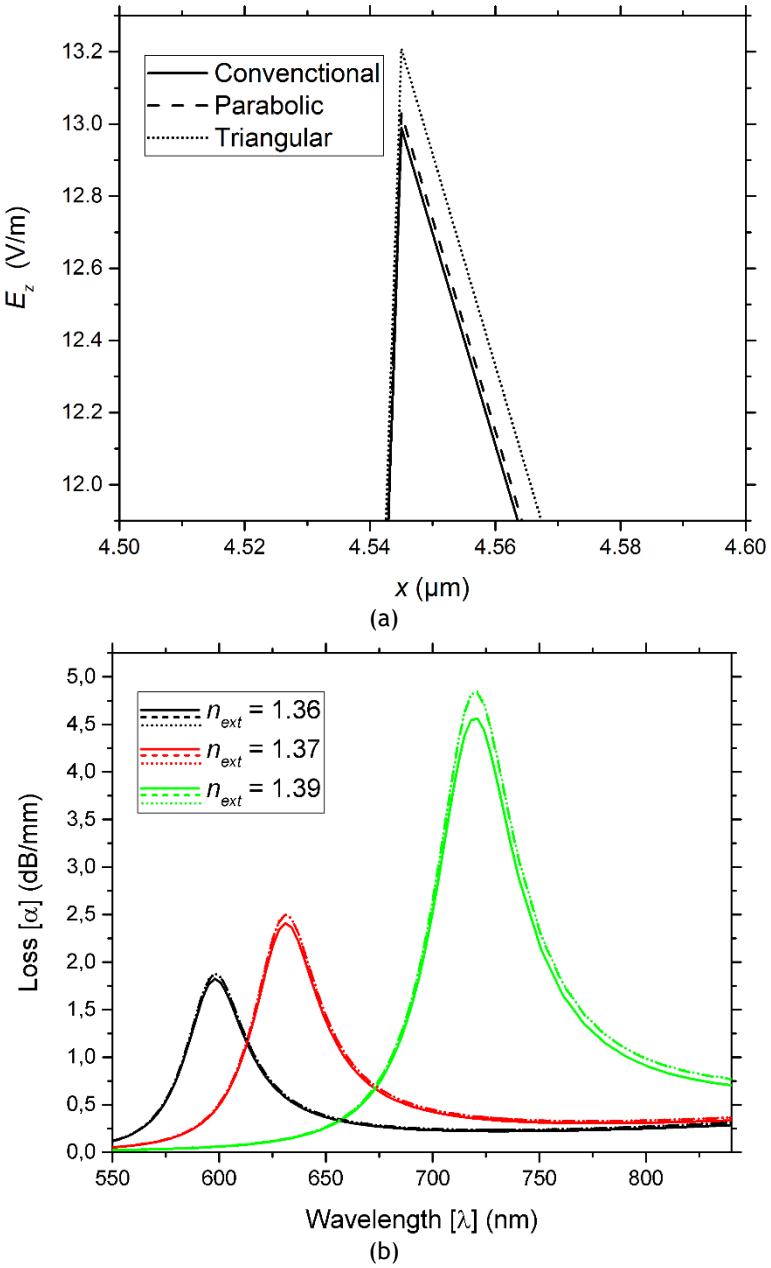

Figure 4.13 (a) Intensity of the electric field E_z in 1D (V/μm) as function of the longitudinal fiber *x* at λ = 630 nm. (b) Attenuation as a function of wavelength for different external refractive indexes (n_{ext}), for three configurations of the SPR sensor, convectional (solid line), parabolic (dashed line) and triangular (dot line), where the d_m = 45 nm and *d* = 4.5 μm.

In this case, instead of using equation 4.5 for calculating the transmission we used equation 3.36 to calculate the loss in the end of the fiber, as function of the wavelength, for all configurations, as shown in Figure 4.13b. In all configurations the

wavelength that generates the SPR is the same, since the SPR wavelength depends mainly on the metal type, its thickness and on the refractive index of the external medium [45]. The intensity of the SPR deep changes for each configuration and the highest deeps are as expected for the parabolic and triangular configurations. Even though the effect is small for the configurations tested, this shows that we can fine tune the intensity of the SPR deep by changing the configuration of the D-type optical fiber.

The two new microstructured D-type fiber configurations presented higher intensity of the electric field in the external medium and higher SPR intensity deep (parabolic and triangular configuration) when compared with the conventional D-type fiber. These results suggest new fiber configurations that include high refractive index contrast microstructures, such as holes, provide a way of optimizing the performance of SPR sensors based on optical fibers.

4.2.3 Microstructured D-type fibers: optimization of the parameters of the SPR

A new configuration of fiber optical based in SPR can be realized and optimized, being, therefore, necessary to perform a set of simulations. The optimization is carried out focussing on the type and thickness of metal, the distance between the core and the metal (residual cladding), the utilization of an overlayer with high refractive index, the wavelength range of detection of the sensor, among others.

This subsection considers that the metal of the film is gold, because this material is typically associated with the best sensitivity [71]. The optimization of the thickness of the metal is performed, as shown in Figure 4.14. In terms of the results and in what concerns the material thickness, the optimal point obtained by the simulation is when a layer of 45 to 65 nm is used, which is normally the value used in literature [23]. From Figure 4.14 we expect some variation in the sensitivity of the SPR sensor because each thickness of the metal occurs in different intensity and wavelength.

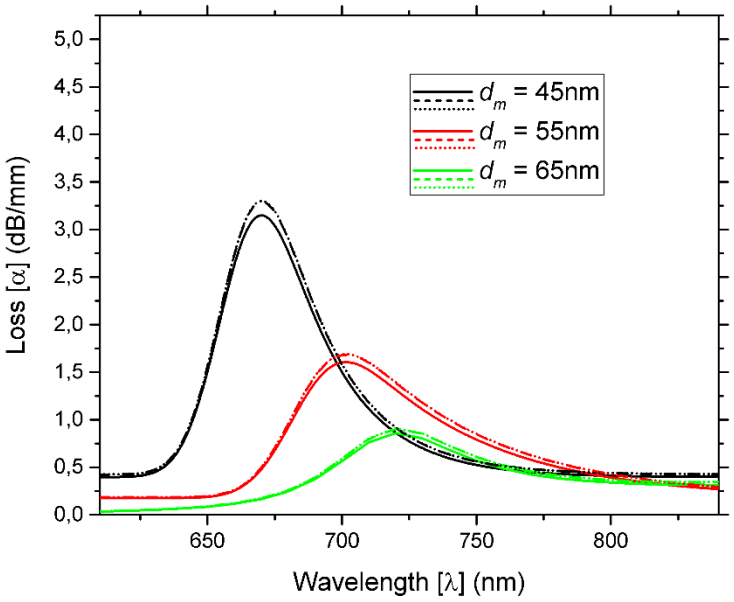

Figure 4.14 Attenuation as a function of wavelength for different thicknesses of gold (Au) and for three configurations of the SPR sensor, conventional (solid line), parabolic (dashed line) and triangular (dot line) where n_{ext} = 1.38 and d = 4.5μm.

The thickness of the metal is not considered in the optimization of the intensity of the loss in our SPR sensor, because the thickness changes the loss intensity and wavelength, simultaneously. The increase or decrease of the loss intensity without changing the wavelength can be achieved by changing the residual cladding, *d*, as is shown Figure 4.15.

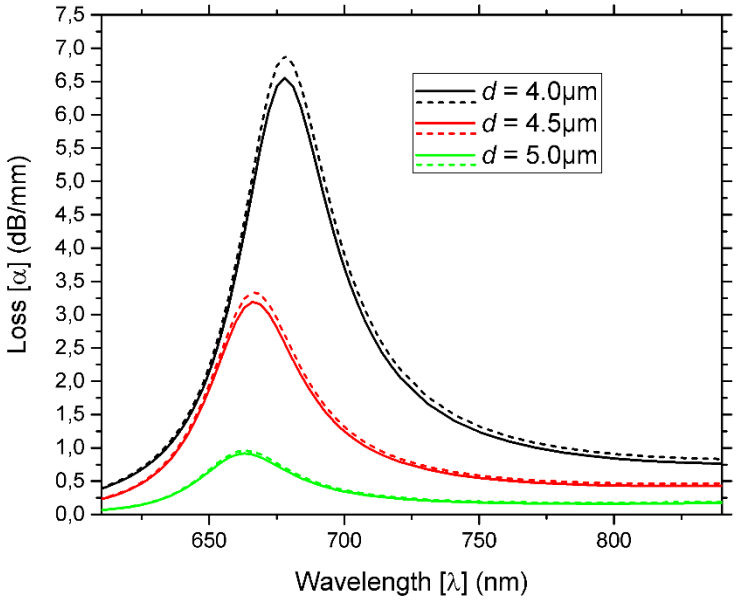

Figure 4.15 Simulation of attenuation as function of the wavelength, for different values of residual cladding, *d*. In this simulation, only two configurations of the SPR sensor were studied, conventional (solid line) and parabolic (dashed line) where d_m = 45 nm and n_{ext} = 1.38.

From Figure 4.14 and Figure 4.15 it is possible to optimize a sensor that works for a wavelength operation near 660 nm and a metal thickness of 45 nm (Au), and choose the appropriate residual cladding.

In case another wavelength operation range is required, one possible solution is to apply an additional layer of a dielectric with a high refractive index, such as tantalum pentoxide (Ta_2O_5) [68], [69], as shown in Figure 4.10.

4.3 PCF D-type sensor based in SPR.

4.3.1 Introduction of photonic crystal fibers

Another kind of SPR sensing configuration is based on photonic crystal fibers (PCFs). While in the last section the refractive index contrast between the core and the cladding results from a different doping of the silica, in PCF fibers there is no doping and the contrast in refractive index between core and cladding results from the lower refractive index of the cladding due to the presence of an array of air holes. Therefore, these fibers are composed of a periodic array of air holes which surround a material, normally SiO_2, running along the entire length of the fiber and confining light in the core (Figure 4.16). The array is characterized by the pitch, denoted by Λ, (center to center distance between the holes) and the hole diameter d_{hole}. The guiding mechanism is a modified form of total internal reflection resulting from the strong index contrast between silica and the holey cladding. They have extraordinary-index

fiber properties compared to conventional step optical fibers, such as endless single-mode operation, unusual chromatic dispersion, high birefringence, high or low non-linearity, among others. It can be shown numerically that endlessly single mode (ESM) guidance occurs when the geometry of the holey array satisfies the relation [118]:

$$\frac{d}{\Lambda} < 0.4 \tag{4.6}$$

Additionally, the optical properties of silica-air PCFs are determined by the position, size, and shape of the air holes, and can be extended by filling the holes with materials such as liquid crystals [119] or metals [97], [120] etc., and consequently have a number of advantages for sensing applications. There are many studies with different configurations using PCFs and SPR [28], [121].

Examples of optical sensors combining photonic bandgap fiber and PCF with D-type fibers can be found in references [25], [122]. In the first reference and for the sensitivity study, the central core is replaced by a hollow core where the light guiding mechanism is based on an effect called photonic bandgap. For the second reference and for the sensitivity study, the distance between the metal and the core of the fiber is analyzed.

In contrast to circular symmetric step-index fibers, the wave equation for PCF cannot be solved analytically, because of the hexagonal symmetry and the strong index-contrast between air and silica. Therefore, we have to use numerical techniques and in the next subsection we show how to apply finite element modeling to compute the propagation constants and modal field profiles.

4.3.2 Design of photonic crystal fibers

Again for the performance characterization of the SPR PCF D-type sensor we compare it with the conventional SPR D-type fiber based on a singlemode configuration (r_{co} = 4 μm) where the edge of the fiber is placed at d = 4.05 μm, the refractive index of the core is n_{co} = 1.476 and for the cladding is n_{cl} = 1.452, for a wavelength of 900 nm. In the case of the PCF D-type fiber, the configuration is d_{hole} = 1.61 μm, Λ = 2.3 μm ($d/\Lambda > 0.4$, therefore, it is expected to have more than one mode. Although for these conditions, the PCF supports more than one mode, in this analysis we consider that only the fundamental mode is excited and leave for the next chapter the features of SPR sensing with multiples modes.) and d = 3.2 μm. For both fibers the thickness of the metal is d_m = 45 nm, the external refractive index is n_{ext} = 1.39 and the length of the sensor is L = 1 mm, as shown in Figure 4.16.

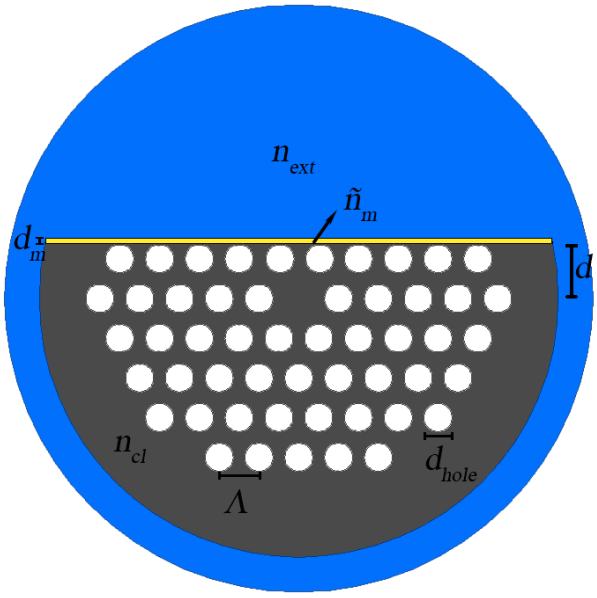

Figure 4.16 Schematic of the PCF D-type.

4.3.3 Loss of the conventional and PCF D-type fiber

Using Equation 3.73 we can compute the attenuation through the fiber as a function of wavelength for the conventional and PCF D-type fiber (Figure 4.17), which is directly related with the light that is applied to the SPR. The loss peak for the external refractive index of 1.34 (red curve) occurs at the wavelength 521 nm, with a loss of 4.57 dB/mm and at 550 nm with a loss of the 1.10×10^{-2} dB/mm, for conventional and PCF D-type fiber, respectively. In the conventional D-type fiber, the loss is stronger and the resonance occurs at lower wavelengths, when compared with the PCF D-type.

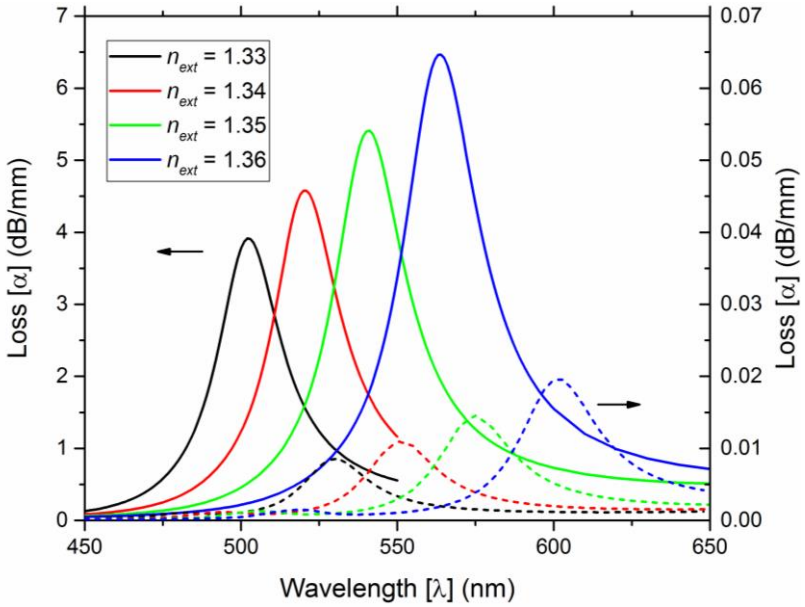

Figure 4.17 Attenuation as a function of wavelength for different external refractive indexes for the conventional (solid line) and PCF (dashed line) D-type. L = 1 mm and d_m = 45 nm.

It is interesting to note that in the considered PCF, light is strongly confined in the center of the fiber, the evanescent field in the external medium is lower than in the

conventional D-type, since the electric field that reaches the metal is low, causing losses to be also low.

4.3.4 Sensitivity and resolution of the two configurations

Figure 4.17 also shows the variation of the attenuation as a function of the wavelength for different external refractive indexes (n_{ext}), for the two types of fiber configurations. The results show a shift to the right in wavelength when the external refractive index is increased.

Using the results of Figure 4.17 and equation 3.71, we can calculate the sensitivity of the refractive index sensor, as shown in Table 4.2, which presents the sensitivity for different values of the external refractive index for the two configurations. Considering an experimental implementation, where a spectral variation of 0.1 nm can be accurately detected and using equation 3.72, we can get the corresponding refractive index sensing resolution as shown in Table 4.2.

Table 4.2 Sensitivity and resolution values for the refractive index optical fiber sensors based on conventional and on PCF D-type fiber configurations.

	Sensitivity (nm/RIU)		**Resolution (RIU)**	
Range of n_{ext}	**Conventional**	**PCF**	**Conventional**	**PCF**
[1.33,1.34]	1.90×10^{3}	2.00×10^{3}	5.26×10^{-5}	5.00×10^{-5}
[1.34,1.35]	2.00×10^{3}	2.40×10^{3}	5.00×10^{-5}	4.17×10^{-5}
[1.35,1.36]	2.29×10^{3}	2.90×10^{3}	4.35×10^{-5}	3.45×10^{-5}

The results from Table 4.2 show that the PFC D-type fiber configuration demonstrates better results in sensitivity and resolution than the conventional D-type fiber configuration. Although for the PCF fiber the performance of the sensor yields better sensitivity and resolution, the level of losses in this fiber is considerably lower (two orders of magnitude) than the conventional fibre and, therefore, it is harder to detect the spectral signature of the surface plasmon resonance. On the other hand, an enhancement of the performance of the studied PCF D-type sensor is expected when the evanescent field in the metal is increased.

4.4 Proposals of PCF D-type sensors based in SPR.

In this section, we investigate how the removal of some of the holes in the fiber can be used to increase the intensity of the electromagnetic field near the metal layer, where the sensing occurs. Through this process it is possible to improve the sensitivity and resolution of the sensor to variations of the external refractive index. Thus, we compare the conventional D-type sensor (Figure 4.1) with our enhanced proposal of the PCF D-type sensor, which is represented in Figure 4.18.

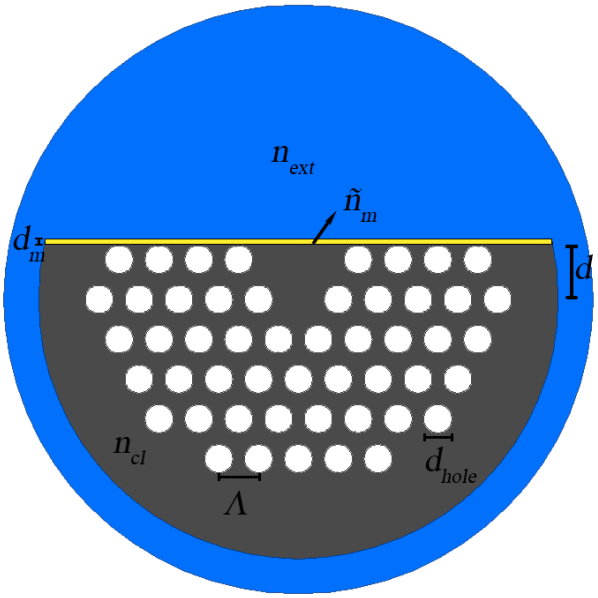

Figure 4.18 Design of the enhanced proposal for the PCF D-type sensor based in SPR.

The configuration is similar to the PCF D-type sensor (Figure 4.16), but we removed two of the holes between the center of the fiber and the metal, to increase the electromagnetic field present near the metal. The parameters used are the same of the PCF D-type sensor. The materials are calculated in the same way that they were studied before.

4.4.1 Loss and distribution of the Poynting vector

Using equation 3.36, we can compute the attenuation through the fiber as a function of the wavelength for the conventional and for the enhanced PCF D-type, as shown in Figure 4.19.

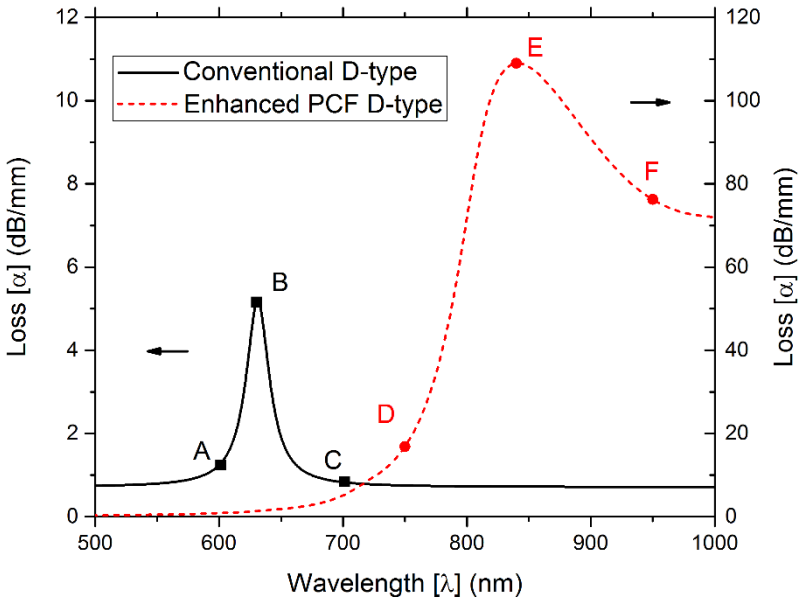

Figure 4.19 Attenuation as a function of wavelength for D-type and enhanced D-type fibers. The configurations had the following parameters: L = 1 mm, n_{ext} = 1.39 and d_m = 45 nm.

In Figure 4.19 the peak in each configuration occurs at the wavelength of 630 nm with a loss of 4.90 dB/mm and at the wavelength of 842 nm with a loss of 109.11

dB/mm, for conventional and enhanced PCF D-type fiber, respectively. The conventional D-type fiber has a much weaker loss and the resonance occurs in lower wavelengths when compared with the enhanced PCF D-type fiber.

The two configurations can also be compared in terms of the Poynting vector distribution. Figure 4.20 shows the Poynting vector, with the arrow indicating the transverse electric field e_x and e_y, of the two configurations, for the different values of wavelength, as shown in Figure 4.19. The loss peaks of the two configurations correspond to an increase of the optical power transferred from the core to the external medium, which results from a strong optical tunneling through the metal film. Although not confirmed by the simulations, these results suggest that the surface plasmon modes in the film play a role in coupling the guided mode of the fiber to the exterior [45].

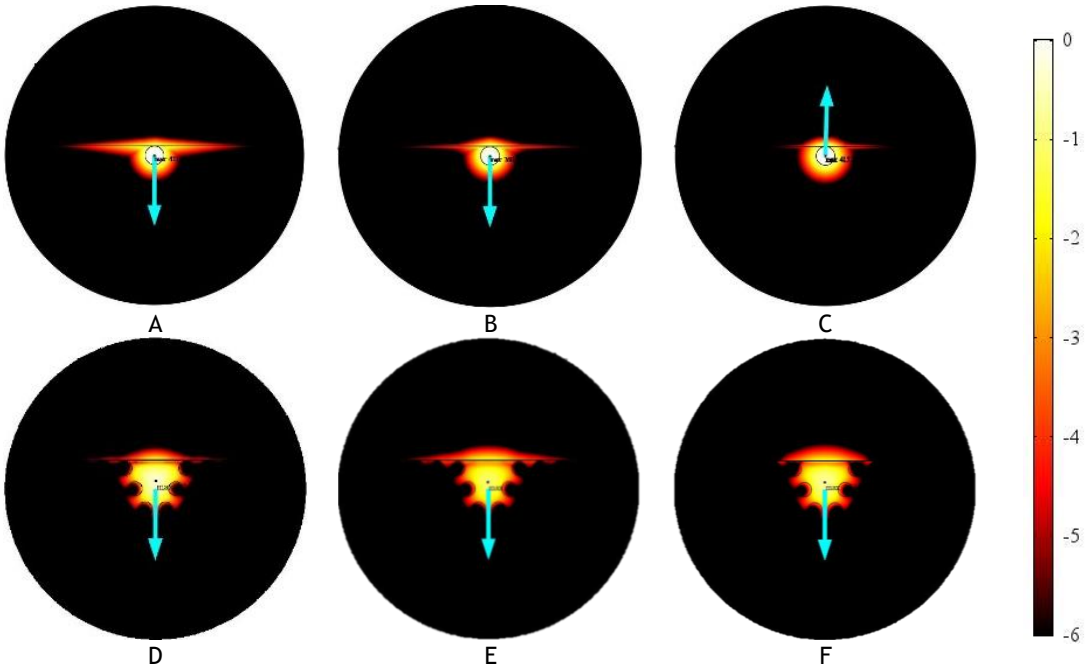

Figure 4.20 Normalized Poynting vector distributions, overlayered by an arrow indicating the transverse electric field e_x and e_y, for the different wavelengths, indicated in Figure 4.19. The upper images are for the conventional D-type fiber and lower images are for the enhanced PCF D-type.

A study of the normalized Poynting vector along a cutline in the symmetry plane of the sensor for the fundamental mode of the enhanced PCF D-type fiber is shown in Figure 4.21. Comparing it with Figure 4.5, it is possible to see that the Poynting vector intensity in the external medium is stronger using the enhanced PCF D-type fiber, than in the conventional D-type fiber, at the resonance wavelength (two fold increase). These results appear to confirm the hypothesis of increase of the optical tunneling through the metal, since the absence of the two holes in the enhanced PCF D-type fiber promotes the delocalization of the field inside the fiber towards the metal film.

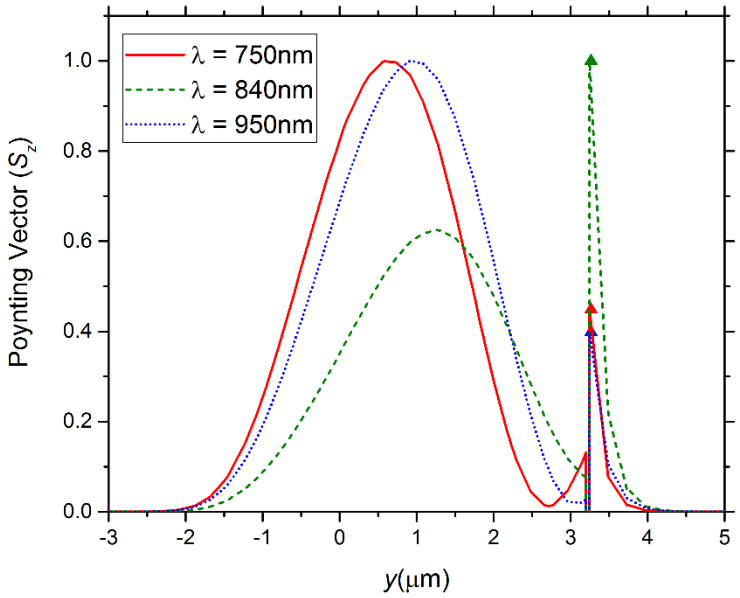

Figure 4.21 Normalized Poynting vector amplitude along a cutline across the fiber core for the different wavelengths indicated in Figure 4.19 for the enhanced PCF D-type fiber.

Figure 4.22 shows the variation of the attenuation as a function of the wavelength for different external media (n_{ext}), for both fiber types. This figure also shows a shift to the right in wavelength when the external refractive index is increased. Again, the values of the loss for the enhanced PFC D-type fiber are considerably higher when compared with conventional D-type fiber, showing a higher interaction of the light with the external medium.

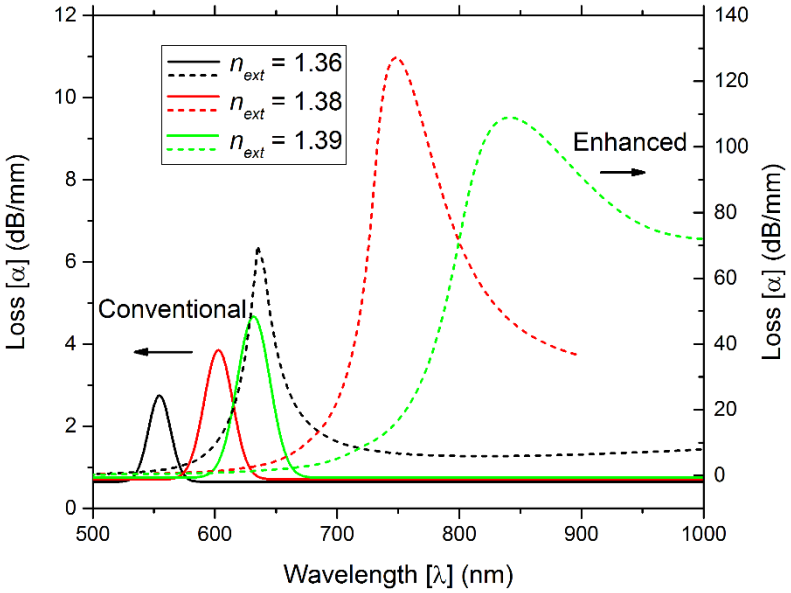

Figure 4.22 Attenuation as a function of wavelength for different refractive indexes of external medium for both configurations. The configurations had the following parameters: d = 4.05 μm and d = 3.2 μm for conventional (solid lines) and enhanced PCF D-type (dashed lines), respectively, L = 1 mm and d_m = 45 nm.

These results suggest that PCF D-type fibers can be also used as optical sensors for measuring refractive index of the external medium. Furthermore, the removal of holes, like in the enhanced PCF D-type fiber, demonstrates that it is possible to increase the sensing performance by engineering the interaction of the optical modes

in the waveguide with surface plasmons of the metallic film, and ultimately the optical losses of the fiber. Figure 4.22 shows that the enhanced PCF D-type fiber with low external refractive index produce narrower resonance peaks, an effect which is especially noticeable for n_{ext} above 1.38. This puts a lower limit to the n_{ext}, since above this value one obtains wide resonance peaks, thus resulting in feeble optical signal and low signal to noise ratios.

Using the results of Figure 4.22 and equation 3.71 we can calculate the sensitivity of the refractive index sensor. Table 4.3 shows the sensitivity for different values of the external refractive index for the two configurations. The results show that the sensitivity of these types of sensors depends strongly on the range of the external medium refractive index. The PCF D-type fiber technology demonstrates better results in the sensitivity than the conventional D-type fiber. When the SPR occurs concomitantly with an effective refractive index of the guided mode closer to the external medium, the confinement of light in the fiber decreases even further. As a result, the SPR effect increases and with it, the overall sensitivity of the sensor. Since the effective refractive index of the guided mode for the PCF D- type fiber is lower than for the conventional D-type fiber, it contributes to a higher sensitivity in the [1.36 - 1.38] RI range. We have repeated the study of the variation of the external refractive index for d_m = 65 nm and obtained similar results in sensitivity with d_m = 45 nm, as shown in Table 4.3. We also observed that the sensitivity of the sensor changes when we increased the metal thickness. For example in the [1.38, 1.39] RI range the SPR sensor decreased the sensitivity in 2000 nm/RIU when the thickness of the metal was increased by 20 nm.

Table 4.3 Sensitivity values for the refractive index optical fiber sensors based on conventional D-type fiber and on the enhanced PCF D-type sensor

	Sensitivity (nm/RIU)			**Resolution (RIU)**		
Range of n_{ext}	**Conventional**	**PCF -45nm**	**PCF -65nm**	**Conventional**	**PCF -45nm**	**PCF -65nm**
[1.36,1.38]	2.40×10^{3}	5.20×10^{3}	5.30×10^{3}	4.20×10^{-5}	1.90×10^{-5}	1.90×10^{-4}
[1.38,1.39]	2.80×10^{3}	10.2×10^{3}	8.20×10^{3}	3.60×10^{-5}	9.80×10^{-6}	1.20×10^{-4}

In order to analyze the effect of the gold thickness fabrication tolerance, we increased the gold thickness by 5% (45 nm + 2.25 nm) and found the variation in the wavelength of the loss peak is $\Delta\lambda$ = (842 nm - 850 nm) / 850 nm=-0.95 %. For the sensitivity, considering the same tolerance and for the [1.38,1.39] RI range, the value found was ΔS = (10.8×10^{3} nm/RIU - 10.2×10^{3} nm/RIU) / 10.2×10^{3} nm/RIU = 5.88 %.

These results show that the enhanced PCF D-type fiber configuration allows a higher interaction of the light with the external medium, namely a two fold increase of the Poynting vector intensity. Comparing both sensing configurations, for the range of n_{ext} [1.38, 1.39], the PCF D-type fiber sensor showed a higher performance, enhancing the sensitivity from 2.8×10^{3} to 10×10^{3} nm/RIU and the resolution from 3.6×10^{-5} to 9.8×10^{-6} RIU, with the conditions described.

4.5 Conclusion

COMSOL Multiphysics was used to test and optimize computationally a sensing configuration, with higher accuracy and considerable economy of time and resources. Some SPR sensor configurations have been tested, namely: the conventional D-type fiber, microstructured fiber with triangular and parabolic arrange of holes, conventional PCF D-type fiber and the enhanced PFC D-type fiber. These new geometry configurations presented the same or higher intensity distributions in the external medium and higher SPR loss when compared with the conventional D-type fiber (except in the case of the conventional PCF D-type fiber).

It was also possible to demonstrate the benefits of using COMSOL to improve the performance of refractive index SPR D-type optical fiber sensors. The optimization of the sensors can be performed through the variation of the metal thickness, the distance of the metal to the center of the fiber and by the use of a high refractive index layer. We concluded the metal thickness changes all the characteristics of the sensors studied in this thesis, such as sensitivity, resolution, operation wavelength and also the loss intensity. The distance *d* only changes the loss intensity. Finally, the high refractive index overlayer alters the sensor operation wavelength. We studied different positions for the air holes in the fiber and we encountered variation in the sensor characteristics, which allowed us to optimize the singlemode SPR sensor.

Furthermore, these results demonstrated the importance of adequate engineer in the integration of the guided modes of the fiber with the optical and plasmonic structures of the device to increase the sensitivity. This approach is not limited to the D-type fibers considered here but can be applied to many other optical and plasmonic systems.

Chapter 5 Multimode sensors with thin metal films

The previous chapter investigated the improvements that can be introduced in the conventional configuration of a SPR fiber sensor by introducing and optimizing a set of holes in a D-type fiber to form a D-type photonic crystal fiber. The basic idea was to promote the interaction between the light guided in the fiber (both by reducing the distance between the core of the fiber), the metal interface and the exterior medium, concentrating light in this region. This approach follows a trend in the scientific community by introducing and optimizing metal-dielectric structures in the fiber that can engineer and control the guided mode of light in the fiber that best interacts with the metal layer. In general these designs make use of single mode fibers however, considering multimode fibers introduces a new degree of freedom in the design, namely the wide diversity of modes supported by the fiber, each with a unique distribution of light intensity and capable of distinct interactions with the plasmons, in principle resulting in various sensor performances. This raises therefore the question of how the sensing performances of the individual modes are combined to generate the overall sensor performance, and whether selecting a specific set of modes can result in performance improvements. This chapter is devoted into answering this question, and to do so, we investigate the occurrence of multiple modes found in a plastic and silica multimode optical fibers and their effect on the SPR. We also compare the sensitivity, resolution and the wavelength range when using the fundamental mode or another higher mode.

5.1 Introduction to multimode fibers

The problem of multiple modes propagating in the optical fiber resulted in a SPR sensor that suffered from modal noise [123]. To solve this problem Lin in [124] proposed the use of a halogen light source and a subtractive mode method. Another solution of this problem was proposed by Homola and Slaik [43] who use a singlemode fiber. From there on, to use singlemode fibers has been the most natural choice for the creation of SPR sensors based on optical fibers [6], [68], [70].

Therefore, the basic singlemode fiber has been the preference choice for optical sensors based on optical fibers, in the past decades for the following reasons:

- *Simplicity*: only one mode is propagated into the fiber (fundamental mode), the complexity of the simulation and experimentation of the sensor depends on the detection of only one mode.
- *Lower power loss*: most of the signal attenuation is caused by the sensor and not by optical dispersion in the fiber, allowing monitorization of multiple sensors at longer distances.
- *Greater distance*: the monitorization or sensing of the sensor can be done at long distance from the receptor, since, with only one mode, the total dispersion of the sensing signal is reduced when compared to a multimode solution.
- *Multiplexing capability*: the possibility to multiplex several sensors in wavelength, using a short spectral window.

For SPR fiber sensors, the main approach consists in removing the cladding partially or completely, so that the light can reach the metal/external interface medium to create the condition of SPR. In these cases, the sensor sensing area depends both on the size of the fiber core that is only a few micrometers and the on the length of the fiber.

One solution to this problem is to work with fibers with a bigger core size (multimode fibers) allowing to increase the sensing area and the sensor robustness. Another solution is based on microstructured fiber or photonics crystal fiber (PCF), which contain holes near the center of the fiber in whose internal surface can be deposited a thin metal layer. This reduces the interaction distance between the guided optical mode, the plamons and the external medium, without the need to produce structural changes in the fiber, which may destroy it partially or totally. This proposal can be a good solution but with a higher cost, more complex to fabricate with very precise and expensive equipment. The utilization of multimode fiber can be an interesting solution for the problem.

SPR multimode fiber sensors present some advantages and disadvantages when compared with SPR singlemode fiber sensors:

- *Bigger core*: A bigger core introduces both advantages and difficulties in the SPR fiber sensors because on one hand, it has a bigger sensing area, it has a more robust configuration, but on the other hand, the modes that propagate in the fiber have higher dispersion and consequently signal attenuation and on top of it we still need to consider the extra signal attenuation imposed by the SPR [122].
- *Smaller transmission distance*: The higher optical dispersion of this fiber causes the maximum distance for the recuperation of the signal to drop drastically.
- *Multiplexing capability*: there is less sensor wavelength multiplexing capability due to the spectral width of each sensor signal.
- *Cost*: the cost of the multimode or singlemode fiber in glass is more or less the same, the difference is on the emission and detection blocks, where singlemode technology is more expensive.

In general, the multimode optical fiber employed is either based on glass or on plastic. For low-cost SPR sensing systems, plastic optical fibers (POFs) are especially advantageous due to their excellent flexibility, easy manipulation, great numerical

aperture, large diameter, and the fact that plastic can withstand smaller bend radii than glass [109], [125].

5.2 Multimode fiber sensor based in SPR

In **Erro! A origem da referência não foi encontrada.** was presented an extensive study of the different variations of the Kretschmann configuration, where light is propagated in a singlemode optical fiber for the excitation of the surface plasmon. In the case of multimode fiber the information found in literature is poor, because the high dispersion and attenuation, the propagation of light in the fiber is worse. But, with the evolution of technology and the interest of having low-cost sensors with moderate sensitivity and resolution, work has been carried out in SPR on multimode fibers [126].

The first SPR sensors based in multimode fibers were compose by a fiber where the cladding was partly removed and a metal film was deposited around the exposed section of fiber core [5]. The first multimode fiber based SPR sensors reached a resolution of $5x10^{-5}$ RIU [60].

Different configurations of SPR sensors based on plastic clad silica (PCS) fibers and on multimode silica fibers have been studied in the last two decades, some examples of configurations are the removed cladding [5], [59], [80], a side-polished fiber [124], tip-polished fiber [95], [127] and tapered fiber [64], [65], [128]. These configurations study and optimize different parameters of the SPR such as the thickness of the metal [95], effect of the overlayer [128], length of the sensor [61], size of the core [59]. In the case of the tapered, different angles and taper profiles [64], [65] among others, where the principal aim is the optimization of the sensitivity and resolution of the sensor.

Plastic Optical Fibers (POF) have same advantages in the context of multimode fibers, since they can also resist smaller bend radii than glass and the refractive index of the core is higher than glass. The first advantage allows increasing the robustness of the sensor and the creation of the other configurations such as the U-shape [129]. The second advantage allows using the sensor to detect higher values of the external medium refractive index (close to 1.49) [90].

Comparing the large applications and variation of the SPR glass optical fiber (GOF) sensors, in recent years, the POF SPR sensors were placed aside, mainly because of the difficulty of employing sol-gel techniques onto POF surface and the high dispersion of the POF [130].

The few configurations of the POF SPR found in literature are like the configurations SPR GOF sensor [48], [129], [131], [132]. Also, the optimization of the SPR POF or multimode GOF in terms of the sensitivity, resolution, signal-noise, loss, wavelength, range of the refractive index external medium follow a similar methodology applied to the optimization of the SPR singlemode sensor. In the case of the SPR multimode sensors, the existence of these different propagating modes in the fiber is not widely studied, as well as the respective effect produced by the metal in the behavior of each mode. The possibility of using different modes to optimize the sensor performance introduces a possible new dimension in the optimization of the sensor.

5.3 POF SPR sensor and effect of modal filtering

In this section, we present the work done in collaboration with Prof. Luigi Zeni, Dr. Nunzio Cennamo, Dr. Pedro Jorge and Dr. Luis Coelho, and reported in [109] resulting from a joint institutional collaboration between department of Industrial and Information Engineering, Second University of Naples, the Institute for Systems and Computer Engineering, Technology and Science (INESC-TEC) and with the Faculty of Exact Sciences and Engineering, University of Madeira [109].

The experimental SPR sensor configurations are based on a side-polished POF coated with a multi-layer element as shown in Figure 5.1 The effect of a Tapered-POF Filter connected before or after the SPR sensor system is then tested for sensor optimization.

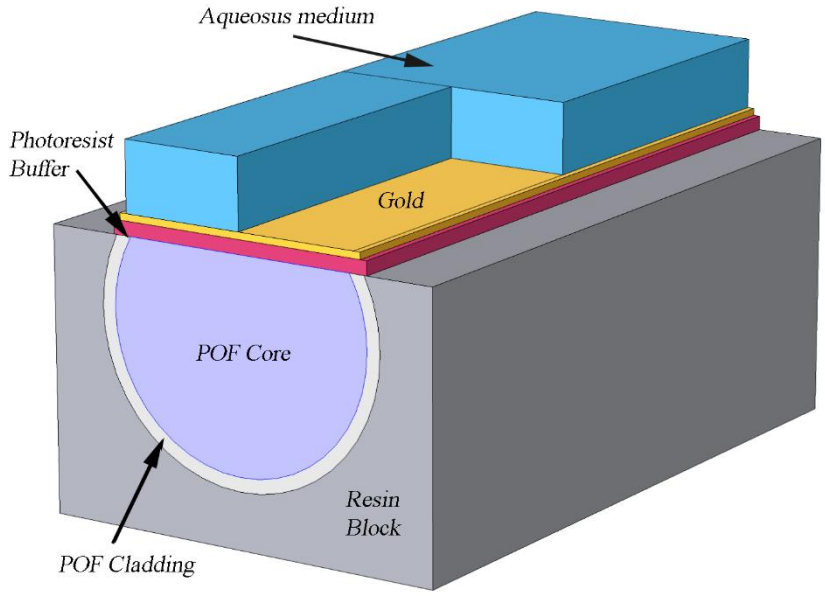

Figure 5.1 Section view of the sensor system based on SPR in POF.

Figure 5.1 shows the schematic section view of SPR sensor system in POF. The plastic optical fiber has a Polymethyl methacrylate (PMMA) core of 980 μm and a fluorinated polymer cladding of 10 μm. Experimental evidence indicates that the configuration with a fiber diameter of 1000 μm exhibits better performance in terms of sensitivity and resolution but not in terms of SNR [35]. The refractive index (RI), in the visible range of interest, is about 1.49 for PMMA, 1.41 for fluorinated polymer and 1.61 for Microposit S1813 photoresist (see layer arrangement in Figure 5.1).

5.4 Numerical simulation without tapered POF filter

To better understand the sensor's behavior, a numerical model was implemented. The design used in this numerical simulation is based in the configuration depicted in Figure 5.1 but in this case without the photoresist, to reduce the number of elements in the calculation. The material values were calculated using the Sellmeier equation for the POF and the Drude model for the metal (Au).

One common analysis of SPR sensors is based on the transference matrices for propagation of light in stratified media, originally derived to describe the operation of

SPR sensors using the Kretschmann configuration based on prisms [1]. From a fundamental point of view, this is equivalent to consider a ray approximation of the propagation modes inside the fiber and is valid if the modal structure of the fiber is not too much affected by the change in cross section profile introduced by the polishing. Then, the transmission along the sensing section of the fiber is affected by the losses of light towards the exterior introduced by each reflection at the metallic film.

However, for the sensor considered in this work, such approach is too crude because the polishing process removes a significant part of the core which affects the modal structure of that section of the fiber. This can be clearly identified in Figure 5.2 where is shown the impact on the intensity distribution of the LP02 (mode 56) and LP04 (mode 16) modes introduced by the change from a circular to a cut profile with the gold layer. It is important to notice that higher order modes are more affected by the change in profile because for them, light propagates preferably at the edge of the core and thus interacts more with the polished surface than lower order modes, which propagate more closely to the center of the core.

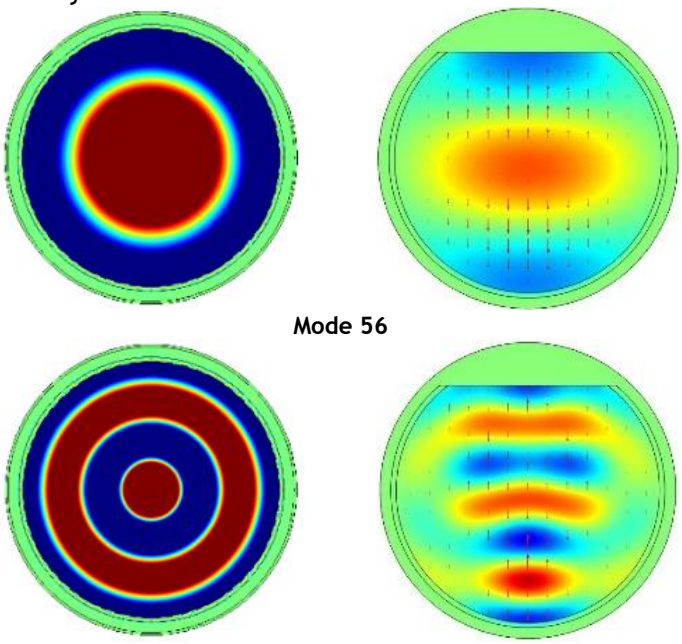

Figure 5.2 Numerical results for two modes LP02 (mode 56) and LP04 (mode 16) in POF. (a) POF without the cut, (b) POF with cut and gold layer.

A second effect is that this also promotes the interaction of higher order modes with the surface plasmons on the metal and therefore these higher modes are more affected by the SPR. Thus, and as can be seen in Figure 5.3a, the losses introduced to higher order modes are much more striking, resulting in a stronger wavelength loss. These results indicate that, the selection of excitation/detection of higher order modes can therefore promote the enhancement of the plasmonic response of fiber optic SPR based sensors.

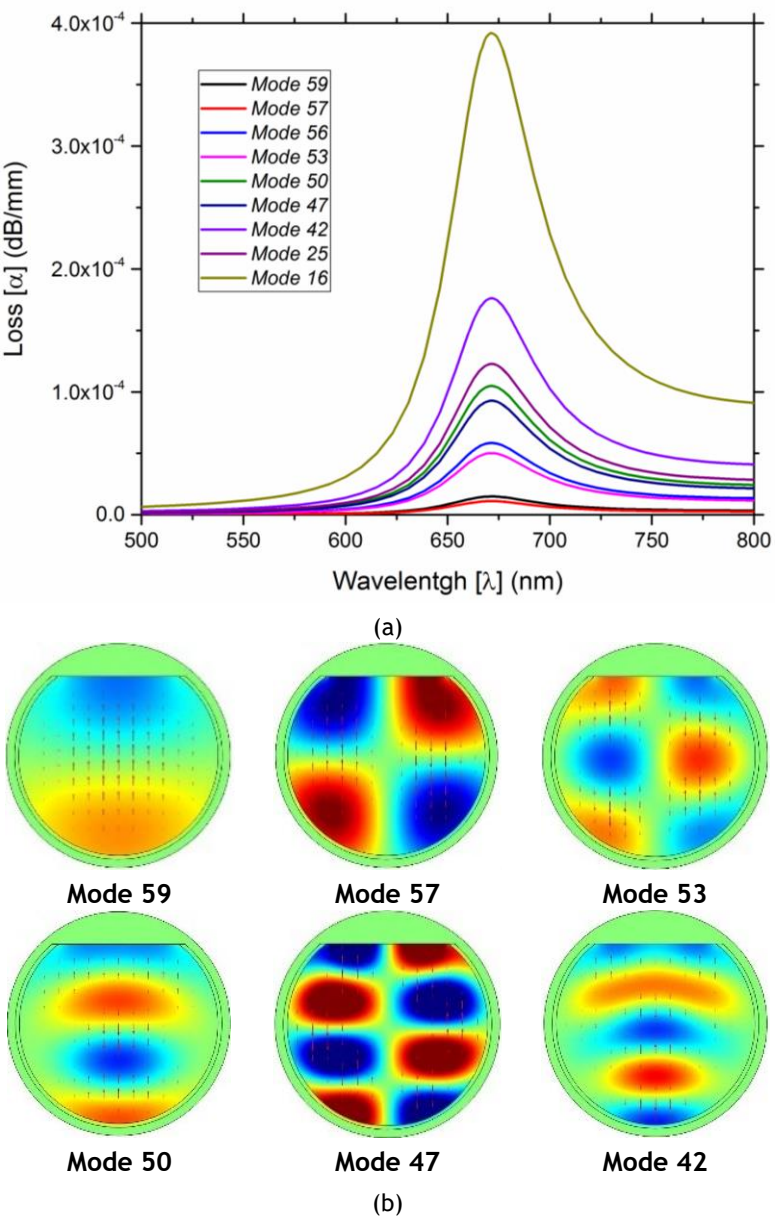

Figure 5.3 (a) Attenuation as function of the wavelength for different modes when the RI of the external medium is 1.39. (b) The distribution of the light intensity of the sensor for different modes.

To complete the study of the numerical simulation of the POF sensor based in SPR, the study of the sensor behaviour when exposed to different external refractive indices is necessary, as shown in Figure 5.4. Figure 5.4a shows the behavior of the sensor for mode 56 and for mode 16. Figure 5.4b is a magnification of Figure 5.4a for mode 56.

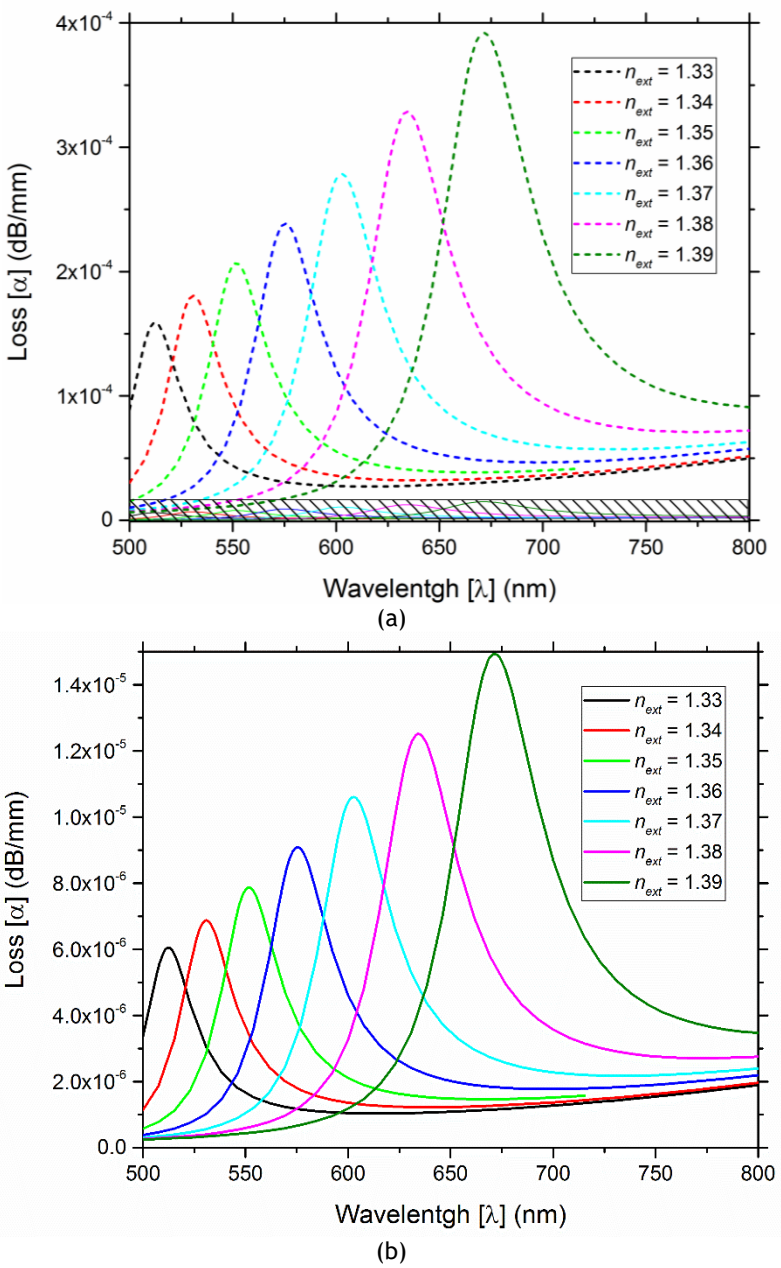

Figure 5.4 Attenuation as function of wavelength for different values of the external refractive index of the sensor for: (a) mode 16 (dashed line) and mode 56 (solid line), (b) magnification of the mode 56 behavior.

Figure 5.4 shows the wavelength of the resonant peak is the same, independently of the mode.

5.5 Experimental characterization of the POF SPR sensor

The fabricated optical sensor system was realized by removing the cladding of the plastic optical fiber close to the half the fiber circumference, the buffer of Microposit S1813 photoresist was spin coated on the exposed core, and finally a thin gold film was deposited using a sputtering machine. The sample consisted in a plastic optical fiber without jacket embedded in a resin block, with the purpose of easing the polishing process. The polishing process was carried out with a 5 μm polishing paper to remove the cladding and part of the core. After 20 complete strokes following a

"figure of eight" to completely expose the core, a 1μm polishing paper was used for another 20 complete strokes with a "figure of eight" pattern. The implemented sensing region was about 10 mm in length. The buffer of Microposit S1813 photoresist was introduced by means of spin coating. The Microposit S1813 photoresist is deposited in one drop (about 0.1 ml) on the center of the substrate. The sample is then spun at 6000 rpm for 60 seconds. The final thickness of photoresist buffer was about 1.5 μm. Experimental results indicate that this configuration with the photoresist buffer layer exhibits better performance in terms of detectable RI range and SNR [48]. Finally, a thin gold film was sputtered by using a sputtering machine (Bal-Tec SCD 500). The sputtering process was repeated twice with a current of 60 mA for a time of 35 seconds (20 nm for step). The gold film so obtained was 60 nm thick and presented a good adhesion to the substrate, verified by its resistance to rinsing in de-ionized water.

Measurements were carried out with an experimental setup arranged to measure the transmitted light spectrum and characterized by a halogen lamp, illuminating the optical sensor system, and a spectrum analyzer for spectral interrogation. The halogen lamp employed exhibits a wavelength emission range from 360 nm to 1700 nm, while the spectrum analyzer detection range was from 300 nm to 1100 nm.

In this work, three different POF sensor configurations are presented and experimentally tested with spectral interrogation: first, the configuration without a tapered POF filter (see Figure 5.1); second, the configuration with a tapered POF filter at the input of the fiber optic SPR sensor system (see Figure 5.5); third, the configuration with a tapered POF filter at the output of the POF, before the spectrum analyzer and after the SPR sensor (see Figure 5.6). The tapered POF presents a PMMA core of 980 μm, a fluorinated cladding of 10 μm, a taper ratio (r_i/r_o) of about 1.8 and a taper region (L_t) of about 10mm in length.

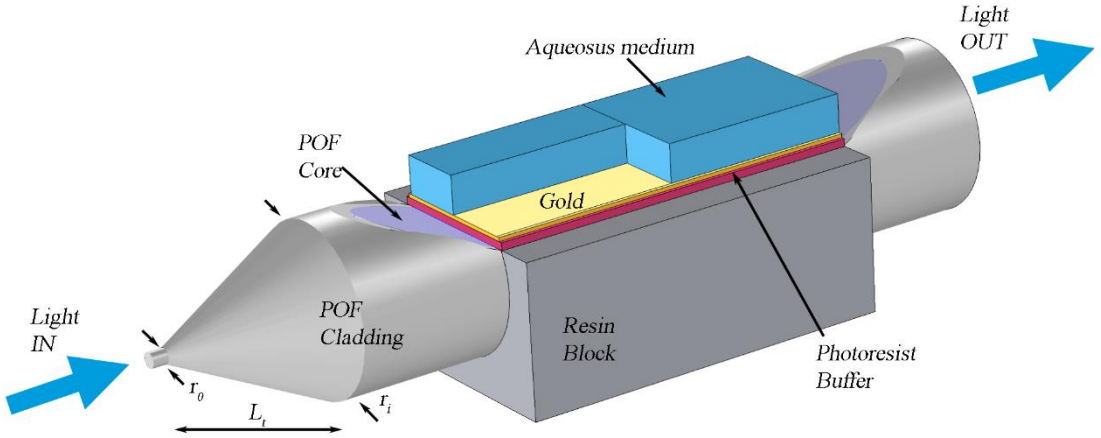

Figure 5.5 Experimental configuration of the sensor system with tapered POF filter at the input of the sensor system

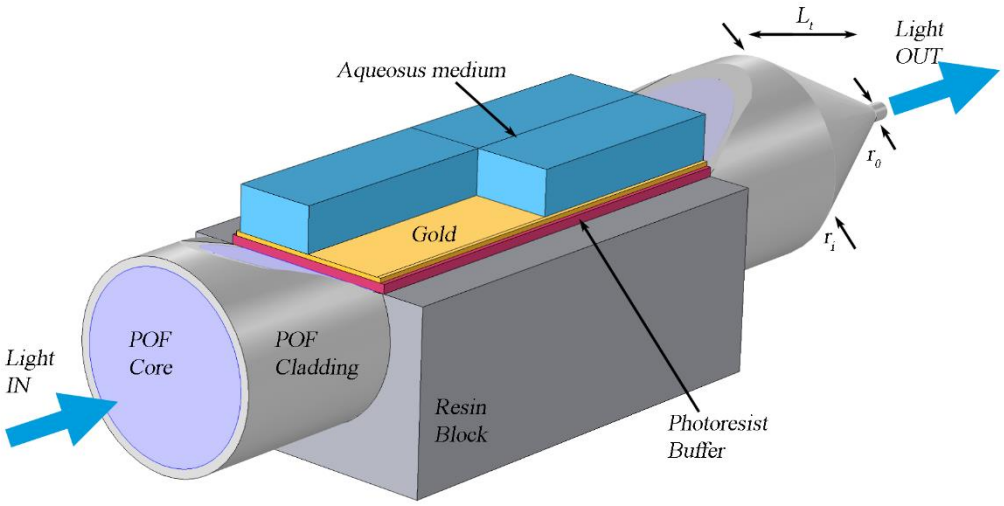

Figure 5.6 Experimental configuration of the sensor system with tapered POF filter at the output of the sensor system.

To obtain these tapers, the plastic optical fiber, without protective jacket, was heated at 150°C and stretched with a motorized linear positioning stage until the taper ratio reached 1.8.

5.5.1 Experimental configuration without tapered POF filter

Figure 5.7 reports the experimental SPR transmission spectra, obtained without the tapered POF filter configuration (see Figure 5.1), normalized to the spectrum achieved with air as the surrounding by the external medium, for seven different solutions (aqueous environment) with RI ranging from 1.330 to 1.390. While the increasing RI introduces a shift in the resonance peak, it also results in a broadening of the resonance curve width, $\delta\lambda_{SW}$, together with a decrease of the total attenuation. In this case, using the configuration without tapered POF filter, when the RI increases from 1.330 to 1.390 the resonance wavelength shift is 86.5 nm.

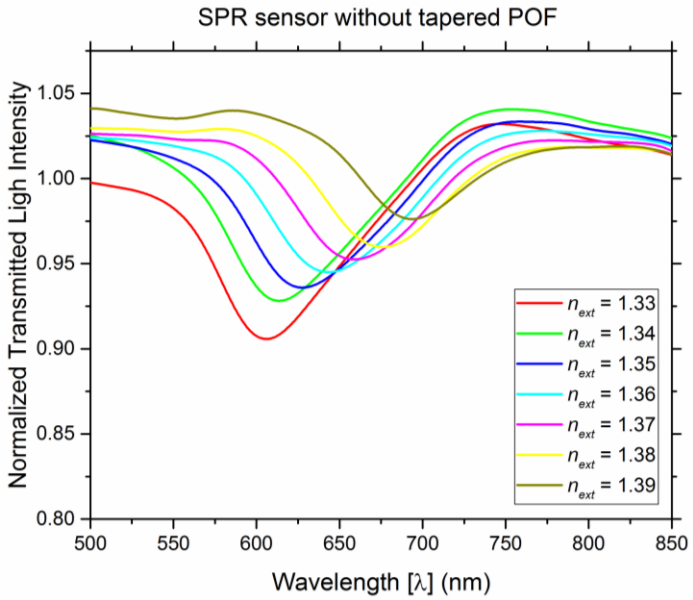

Figure 5.7 Experimentally obtained SPR transmission spectra, normalized to the air spectrum, for different RI of the aqueous medium. Configuration without tapered POF filter.

5.5.2 Configuration with tapered POF filter before the SPR sensor system

Figure 5.8 presents the SPR transmission spectra of the experimental configuration with a tapered POF at the input of the SPR sensor (Figure 5.5). The SPR transmission spectra, normalized to the spectrum achieved with air as the surrounding medium, obtain the same solutions as in Figure 5.7 (RI ranging from 1.330 to 1.390).

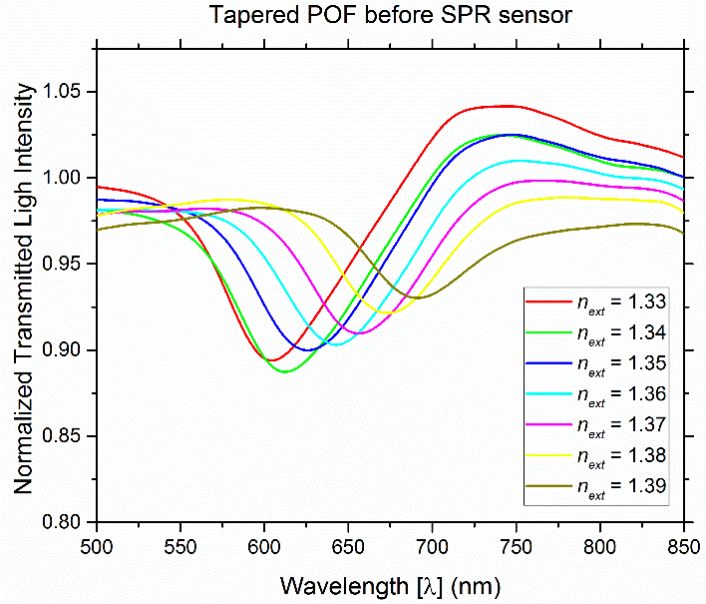

Figure 5.8 Experimentally obtained SPR transmission spectra, normalized to the air spectrum, for different RIs of the aqueous medium. Configuration with tapered POF filter at the input of the SPR sensor.

In this case, using the configuration with a tapered POF filter before the SPR sensor, when the RI increases from 1.330 to 1.390, the resonance wavelength shift is of 94 nm, (an increase of 7.5 nm with respect to the configuration without tapered POF filter). Similarly to the configuration without tapered POF filter, the resonance dip rapidly decreases its depth as the RI increases.

5.5.3 Configuration with tapered POF filter after the SPR sensor system

Figure 5.9 presents the SPR transmission spectra, normalized to the spectrum achieved with air as the surrounding medium, when the experimental configuration with a tapered POF at the output of the SPR sensor is used (Figure 5.6). The SPR transmission spectra have been again obtained for the same solutions (RI ranging from 1.330 to 1.390).

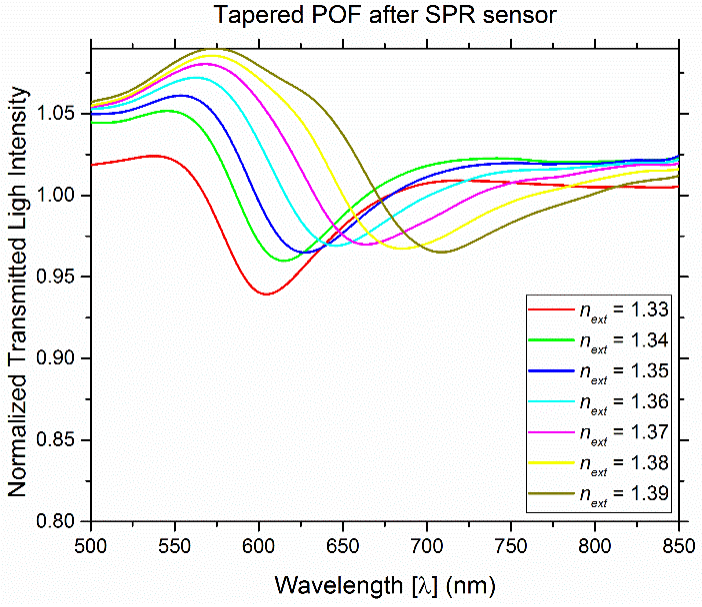

Figure 5.9 Experimentally obtained SPR transmission spectra, normalized to the air spectrum, for different RIs of the aqueous medium. Configuration with tapered POF filter at the output of the SPR sensor.

In this case, using the configuration with tapered POF filter after SPR sensor, when the RI increases from 1.330 to 1.390 the resonance wavelength shift is of 98 nm(an increase of 11.5 nm with respect to the configuration without tapered POF filter). In this way, the sensor sensitivity increased.

5.6 Conclusion

Indeed, looking at the experimental results, the configuration with a tapered POF filter at the output of the SPR sensor system exhibits better performance in terms of sensitivity, when the RI of the aqueous environment increases. Considering the numerical results, this behavior can be ascribed to the rejection of certain modes by the tapered filter, at the sensor output, which results in an increasing of the resonance depth.

On the other hand, filtering at the sensor input seems to have a significant impact on the sensor behavior. This can be explained by the fact that, even if a reduced number of modes is excited at the fiber input, the discontinuity encountered when propagating from the cylinder section to the D-shaped section, creates the conditions to re-excite the modes. The filtering effect is therefore cancelled by this excitation process. For three experimental configurations for higher RI values, the experimental results suggest that the best configuration is composed of the tapered POF filter at the output (after) of the SPR sensor. Overall the results show that strategically placing a simple taper acting as modal filter at the output of a multimode fiber SPR sensor clearly improves its performance. The ability to extend the dynamic range to higher RI is particularly attractive because it enables operation with high RI sensing layers such as molecularly imprinted polymers [133]–[135].

Looking at the numerical results we observed that a variation of the loss intensity is different for each mode but the central wavelength of the loss deep is the same for all modes. These modes with higher loss have an intensity distribution pattern

characterized by having a large spot at the flat surface of the fiber core, as shown in Figure 5.3 in the case of the modes 42 and 50.

Calculating the sensitivity, resolution and wavelength peaks for different values of the n_{ext} using the information of Figure 5.4b and equation 3.71, as shown in Table 5.1. The comparison between the experimental (Figure 5.7) and the simulation (Figure 5.4) indicates some differences in the results. Most of the differences comes from the fact of not considering the photoresist layer in the simulations, since this layer is responsible for a shift to longer wavelengths in the experimental results.

Table 5.1 Sensitivity, resolution and range of the wavelength for the POF D-type of the mode 16.

	Sensitivity(nm/RIU)	**Resolution (RIU)**	**Range λ (nm)**
Range of n_{ext}		**POF D-type mode 16**	
[1.33,1.34]	1.90×10^{3}	5.26×10^{-5}	512-531
[1.34, 1.35]	2.10×10^{3}	4.76×10^{-5}	531-552
[1.35, 1.36]	2.30×10^{3}	4.35×10^{-5}	552-575
[1.36, 1.37]	2.80×10^{3}	3.57×10^{-5}	575-603
[1.37,1.38]	3.10×10^{3}	3.23×10^{-5}	603-675

Three experimental configurations for SPR sensor in a POF platform, have been implemented and experimentally tested. Numerical results were obtained validating the experimental data previously discussed. The configuration with a tapered POF filter at the output of the SPR sensor system exhibits a better performance in terms of sensitivity, depth of the resonance and RI range. This phenomenon is more significant for high RIs. Furthermore, it is also observed that in the standard configuration the contrast of the resonance dip rapidly decreases as the RI increases, limiting the operation range. Using the tapered POF filter at the output of the SPR sensor, however, it is observed that the resonant dip shows an overall higher contrast that is even increased for higher RI values. Therefore, the results presented clearly demonstrate the feasibility of using simple modal filtering to improve the operation range of SPR based sensors in multimode POF fiber.

Experimentally, we have tested three configurations that used a filter to remove different sets of modes from the optical field going through the sensor. Nevertheless, all sensing configurations exhibited the same resonance wavelength despite differences in the loss, which are also observed in the simulations. The differences between the experimental and the numerical results can be justified by not being able to identify exactly which modes are filtered out experimentally from the sensor. Instead, one only has information about the order of the modes that are filtered, typically whether one is filtering the higher or the lower order modes. As a result of this experimental indetermination, it is impossible to know exactly the contribution from each mode to the total output spectrum. This lack of experimental information, prevents us from knowing the exact weigh by which to combine the numerical results

obtained for each mode in order to emulate the experimental transmission and loss curves. However, the numerical results are confirmed by the experimental results since they present similar conclusions.

Chapter 6 Sensors with metamaterials

Until now we have considered only sensors composed of a thin meal film deposited on the surface of a fiber. The quintessential aspect of the film is that the real part of the permittivity of the metal must be negative to support surface plasmon. This is a common property of metals and therefore different metals, like gold, silver, coper and aluminum are normally used in SPR sensor. The differences in permittivity of several metals determine most of the characteristics of the SPR sensors, namely the loss, sensitivity, wavelength of operation, among others. Another alternative is to combine multiple layers of different metals or combining metals with other materials that have been shown to have improved sensing characteristics. The idea is that each of these multiple layers influence each other, such that they work like an effective layer with optical properties that are somewhat of an hybrid agglomeration of the optical properties of the individual materials. This is then a metamaterial with unique optical properties.

In this chapter, we define the method to determine the value of the permittivity of the metamaterial and then we use it to create a SPR sensor. Also, we study the sensitivity, resolution and operation wavelength of a D–type PCF SPR sensor with a metamaterial and also compare it with a D-type PCF SPR sensor with a silver film. We also propose a technique to calculate the thickness and the concentration of the materials of the metamaterial to have a sensor working in the desired wavelength and with the desired loss.

Metamaterials are artificial materials designed to have properties that are not found in natural materials [136]. These metamaterials are composed by multiple elements, usually metallic and dielectric components. Their properties depend not only on the characteristics of their components and their relative abundancy, but also depend on the geometry, typically arranged in repetitive patterns at sub-wavelength scales [101]. One example of a structure of a metamaterial is shown in Figure 6.1. Metamaterials gain their properties not only from their composition, but also from their structures, giving them properties capable of manipulating the light: by blocking, absorbing, improving or flexing the waves, in order to achieve benefits that go beyond what is possible with conventional materials.

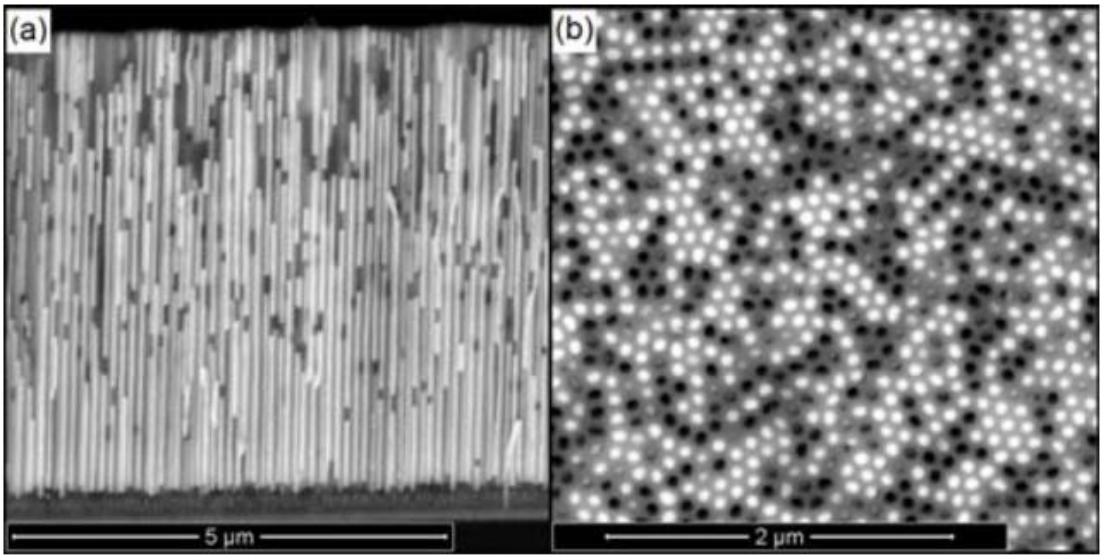

Figure 6.1 Scanning electron microscopy (SEM) images of the fabricated metamaterial: (a) cross section and (b) top view. Bright and dark spots correspond to Ag-filled and empty pores, respectively [99].

Many of the materials that have attracted significant research in optics are those exhibiting a negative permittivity, for particular wavelengths [73], [137], [138]. One of the potential applications of the negative permittivity of metamaterials is therefore the possibility of being used in SPR sensors [73], [137].

6.1 SPR sensor based in metamaterials

There is abundant work in literature that study different metallic layers to optimize SPR sensors (from controlling losses, to increasing sensitivity, among others) [62], [71], [139]. The possible combinations of material layers used are not restricted to metals. Also materials with high refractive index (HRI) can be used to control optical losses and the sensor wavelength operation range [45]. The main problem with these materials or with this combination of materials is the difficultny of controlling their fabrication (including their thickness and roughness) and consequently the control of their optical properties [140].

More recent works on SPR sensors, that combine different materials, have begun to explore the use of optical metamaterials. These artificial materials combine two or more materials to create a new artificial material which exhibits optical properties that cannot be found in naturally occurring materials and which can be designed to attain predefined performances [138]. These properties depend both on the optical properties of their constituent materials, their relative abundance and the geometry of the nano-structures used to combine them. This wide freedom available during fabrication allows to develop metamaterials with almost customized optical properties that can be used to optimize the performance of the sensor (e.g. loss, the light wavelength range, the refractive index range detection, among others) to values beyond that of conventional SPR sensors [73].

We pursue this approach and present a sensor based on SPR that combines a D-type PCF fiber with a metamaterial (Al_2O_3 - Ag). The performance of the sensor is investigated through simulations based on FEM using COMSOL Multiphysics [45]. The

sensor analysis is focused on the percentage of each constituent of the metamaterial and the layer thickness, which are the main parameters in determining it is optical properties. The numerical simulation of new sensing SPR configurations allows select the ones with the best performance to be fabricated, thus leading to a considerable economy of time and resources, when compared to an exhaustive fabrication and test of all possible designs.

6.2 Effective medium theory

Two of the most widely used effective medium approaches are the Maxwell–Garnett theory (MGT) and the Bruggeman effective medium theory (EMT) [138].

The central formula in the Maxwell–Garnett theory (MGT) as defined in [138] is:

$$\frac{\varepsilon_{meta}-\varepsilon_h}{\varepsilon_{meta}+2\varepsilon_h}=f\frac{\varepsilon_1-\varepsilon_h}{\varepsilon_1+2\varepsilon_h} \tag{6.1}$$

where ε_h is embedded in a host medium with relative permittivity ε_1 and f is the volume filling fraction of the ε_1 material in the composite. Alternatively, the effective permittivity ε_{meta} can be expressed in an explicit way as [138]:

$$\varepsilon_{meta}=\varepsilon_h\frac{1+2f\dfrac{\varepsilon_1-\varepsilon_h}{\varepsilon_1+2\varepsilon_h}}{1-f\dfrac{\varepsilon_1-\varepsilon_h}{\varepsilon_1+2\varepsilon_h}} \tag{6.2}$$

Equation 6.1 is known as the Maxwell–Garnett formula, which describes the bulk effective permittivity of a composite in terms of the permittivity of the inclusion ε_1 and the host dielectric constant ε_h. For a metal-dielectric composite, we can view the metal as the inclusion, while the dielectric component serves as the host. Although the effective permittivity in MGT can reach the permittivities of the two constituents (when the filling fraction approaches the two extreme values of f = 0 and f = 1), equation 6.1 clearly shows that MGT treats the matrix and the inclusion in an unsymmetrical manner. Therefore, before evaluating the effective parameters of a two-phase composite using MGT, one constituent has to be considered the “host” and the other the “inclusion.” This asymmetry is particularly strong when the difference in the permittivities of the two materials is large. In fact, MGT provides a reasonable estimation of the effective dielectric function only when the volume filling factor of the inclusion is substantially less than 1.

In order to evaluate the effective parameters of a composite medium without restricting the analysis only to the low-f cases, Bruggeman made a great improvement to the Maxwell–Garnett theory by finding a way to treat the two constituent materials in a symmetric fashion, thus overcoming many of the difficulties of MGT that we discussed above. Bruggeman’s EMT is, arguably, the most widely known version among a variety of mean-field theories.

We used the formula of Bruggeman as [138]:

$$f_1\frac{\varepsilon_1-\varepsilon_{meta}}{\varepsilon_1+\eta\varepsilon_{meta}}+f_2\frac{\varepsilon_2-\varepsilon_m}{\varepsilon_2+\eta\varepsilon_m}=0 \tag{6.3}$$

where ε_m is the dielectric constant of the metamaterial, ε_i, (i = 1, 2) is the refractive index of each of the two types of inclusions with volume filling-ratios of f_1 and $f_2 = 1 - f_1$, respectively, and η is the form factor (η =2 for a spherical configuration and η =1 for a cylindrical configuration).

Unlike the Maxwell–Garnett theory, the two components here are symmetrical with respect to the exchange of roles of ε_1 and ε_2. In other words, in the Effective Medium Theory (EMT) both phases are considered to be embedded in the effective medium, and there is no need to give preference to one phase over the other.

6.3 Metamaterials formed by Alumina and Silver (Al_2O_3 – Ag)

In our case, we adopt the Bruggeman EMT (BEMT) since it is more adequate when the two materials have quite distinct permittivity, rather than the MGT, which considers only materials with similar permittivity and η = 2. Other nanostructures of Al_2O_3 - Ag can also be used, including silver nanowires or nanorods immersed in an alumina matrix. In these cases, the same homogenization model can be used by replacing the form factor η with the appropriate value according to the geometry of the nanostructures. The general optical properties obtained for other metamaterials are alike and therefore we focus here on the simplest form to fabricate [73].

The complex dielectric of the metamaterial results from the combination of properties from its metal and dielectric components. As a result, the metamaterial layer can be considered as an artificial metal layer capable of supporting effective plasmonic modes. Using equation 6.3 we can calculate the complex dielectric of the metamaterial as shown in Figure 6.2, for different concentrations of Ag.

Figure 6.2 shows the real (Figure 6.2a) and imaginary (Figure 6.2b) parts of the metamaterial for the different concentrations or fill ratios of Ag and Al_2O_3, calculated using the BEMT model. Like in the case of a pure silver film, the metamaterial films with fill ratios up to 50% have a negative dielectric constant for the large majority of the spectral range considered, which is a necessary condition to support surface plasmons. In the case of a fill ratio of 50%, the metamaterial is close to an epsilon-near-zero regime, situation where the effective medium approach may have a limited validity.

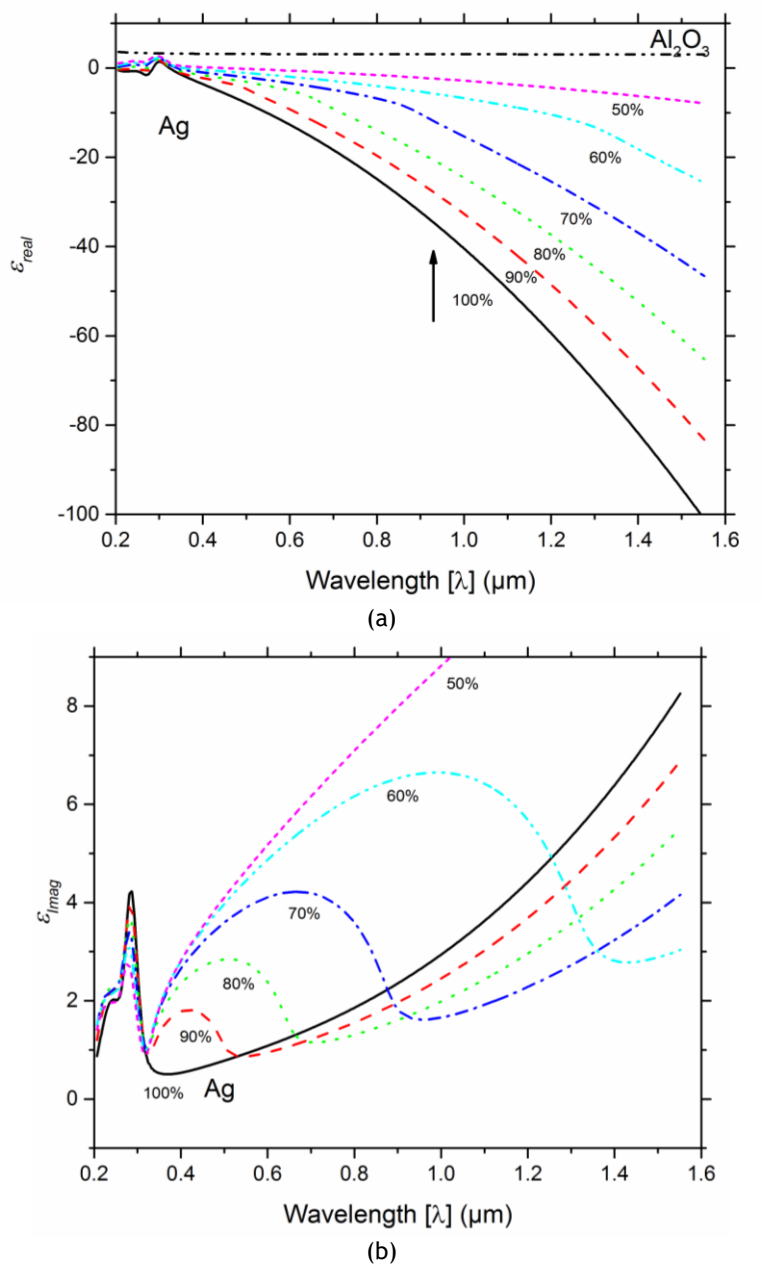

Figure 6.2 Complex dielectric (a) real part and (b) imaginary part of the metamaterial for concentrations of Ag of 100% (solid curve, corresponding to pure silver), 90% (dashed curve), 80% (dotted curve) and 70% (dash-dotted curve) 60% (dash-double dotted curve) and 50% % (small dashed curve). The equivalent curve for alumina (Al_2O_3) is also presented for reference (small dotted curve).

6.4 Proposal SPR sensor based in a metamaterial

We consider the design of an optical sensor of refractive index composed of a PCF fiber with a D-type profile, as described in Figure 6.3. The fiber is composed by a glass core with refractive index n_s, surrounded by an array of dielectric structures (corresponding to the holes in the PCF fiber) with refractive index equal to 1. The refractive index n_g is calculated using Sellmeier's equation (equation 3.25). It is assumed that the space outside the fiber is filled with the analyte medium to be studied, and having an external refractive index n_{ext}. The distance between the center of the fiber and the metamaterial layer is denoted by d - residual cladding, the

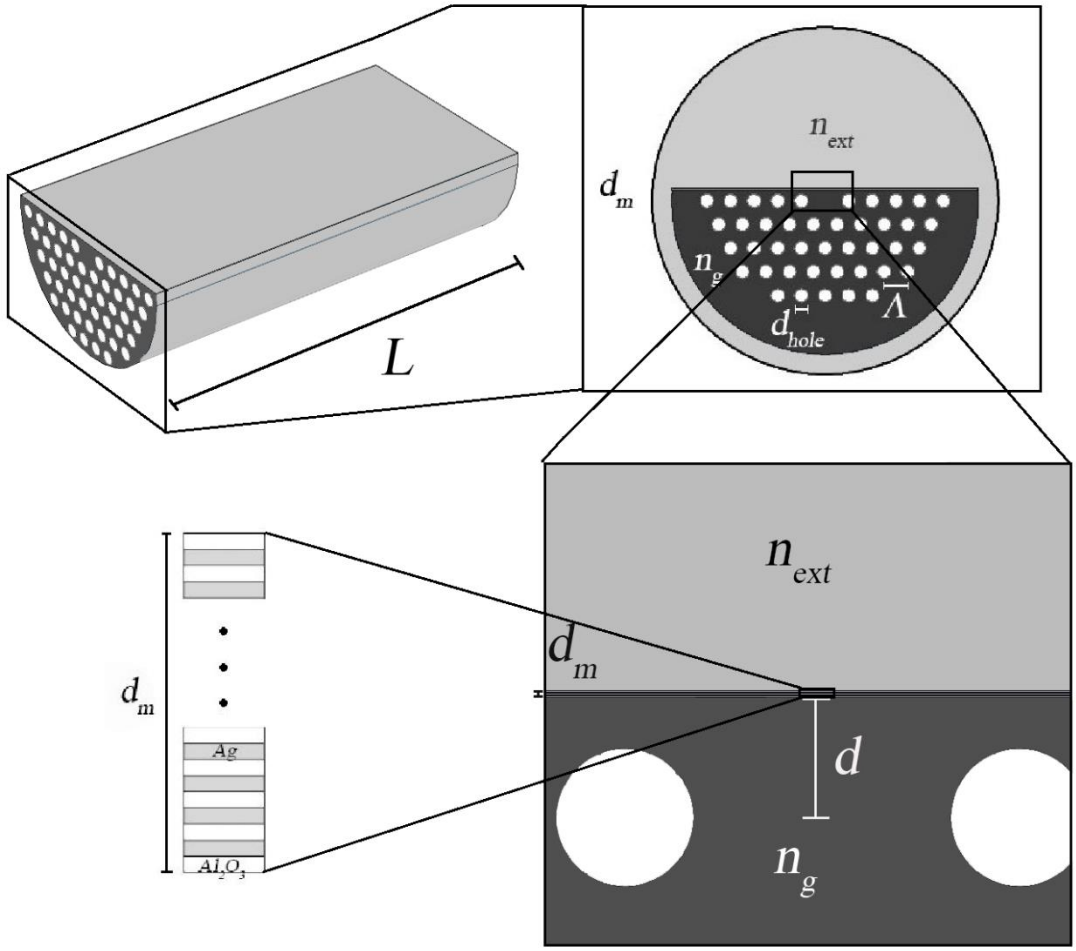

Figure 6.3 From left to right up: three dimensional representation of a section of the fiber sensor, transverse cross-section of the fiber sensor. From right to left down: detail of the structure of the surface of the sensor indicating the position metamaterial film and a scheme of the thin metal-dielectric layers that compose the metamaterial.

thickness of metamaterial layer by d_m, the diameter of the holes by d_{hole}, and the separation of the holes by Λ – pitch.

The conventional PCF is designed to confine light in the core. However, when integrated within a D-type fiber, as is the case of the design described in Figure 6.3, light is confined against the surface of the metal and thus promotes the interaction of the core mode with the external medium. The interaction of the electromagnetic modes with the external media is mediated by a metamaterial film that supports surface plasmons, which improves the sensitivity of the sensor [20]. In this sensor we replace the conventional metal with a metamaterial film composed of thin layers (sub-wavelength) of silver and alumina (see the inset of Figure 6.3).

6.4.1 Metamaterial versus pure metal layers

In this subsection we compare the conventional sensor based on a PCF D-type with a metamaterial and a metal layer (e.g. Ag) with the version based on a metamaterial with 20% of Al_2O_3 and 80% of Ag, using equation 3.73 to compute losses per mm, as function of the wavelength, for different values of the external refractive index. The

results are shown in Figure 6.4, where it is possible to identify a clear peak in attenuation, typical of the SPR, which is not only strongly affected by the change in external refractive index, but also is dramatically affected by the replacement of the metal with a metamaterial layer. Indeed, these results show a red-shift of the peak in wavelength for higher external refractive index. But what is relevant is that not only the values of the losses for metamaterials are considerably higher, amounting to 40 dB/mm (instead of 10 dB/mm obtained with a pure metal layer) but also the operation range in wavelength is around 700 nm (instead of 550 nm obtained with a pure metal layer) for n_{ext} = 1.30.

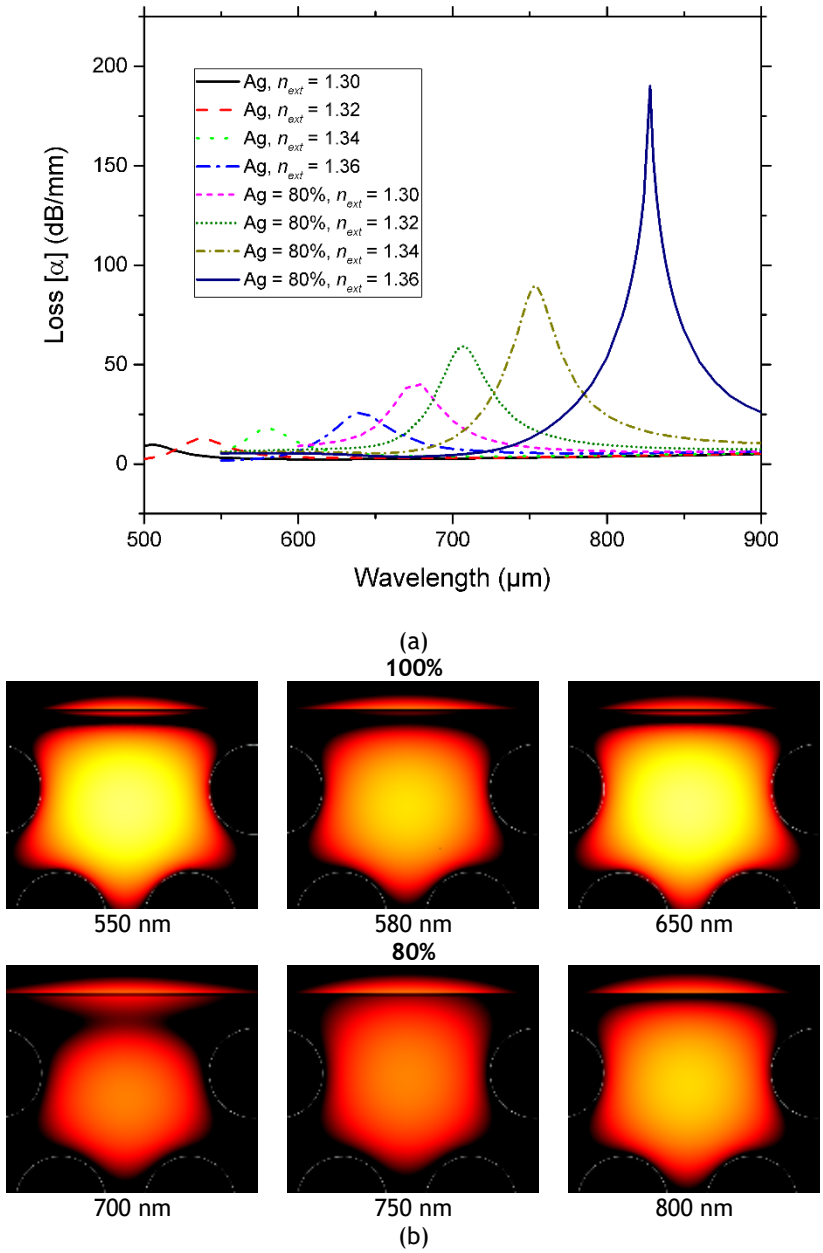

Figure 6.4 (a) Attenuation as function of wavelength for different values of the external refractive index, with two different layers, one with only Ag and the other with metamaterial with a concentration of 80% Ag and 20% Al_2O_3. (b) Distribution of the light in the region of the center of the fiber and the metal/metamaterial film for two concentrations of Ag (100% and 80%) and with 1.34 RI.

This suggests that metamaterials allow a stronger interaction between light in the fiber and the external medium at higher wavelengths, closer to the 850 nm optical

window and more adequate for integration in telecom optical fiber networks. It also follows from these results that it is possible to optimize and balance the ranges of operation of the sensor in both wavelength and external refractive index by choosing the relative concentration of the metal in the metamaterial and the layer thickness. For example, if the sensor is to work between 600 nm and 700 nm and measure refractive indexes between 1.30 and 1.32 RIU instead of 1.35 and 1.36 RIU, then it is possible to fine tune the concentration of Ag around 80% for optimal performance.

Figure 6.4b shows the distribution of the light in the region of the center of the fiber of the metal or metamaterial. The intensity of light around the metal or metamaterial and the coupling between the modes is higher in the metamaterial than the metal, as verified by a higher loss with the metamaterial than with the metal, as shown in Figure 6.4a.

Considering a spectral variation of 0.1 nm that can be accurately detected experimentally, and using equations 3.71 and 3.72, the values of the sensitivity, sensor resolution and spectral range of the refractive index sensor with the considered metamaterial, for different ranges of variation of the external refractive index are shown in Table 6.1.

Table 6.1 Sensitivity, resolution and range of the wavelength values for the refractive index optical fiber sensor based on two materials (Ag and metamaterial).

	Sensitivity (nm/RIU)		**Resolution (RIU)**		**Range λ (nm)**	
Range of n_{ext}	**Ag**	**Metamaterial**	**Ag**	**Metamaterial**	**Ag**	**Metamaterial**
[1.30,1.32]	1.75×10^{3}	2.30×10^{3}	5.88×10^{-5}	4.35×10^{-5}	500-530	670-710
[1.32,1.34]	2.00×10^{3}	2.40×10^{3}	4.76×10^{-5}	4.17×10^{-5}	530-580	710-755
[1.34,1.36]	2.80×10^{3}	3.70×10^{3}	3.57×10^{-5}	2.70×10^{-5}	580-640	755-830

In Table 6.1 we also present the equivalent results for a sensor with a layer of pure metal. Clearly, the sensor with the metamaterial outperforms its counterpart with pure metal in all parameters even though the gains in resolution are marginal. As expected from Figure 6.4, the major improvements are in terms of sensitivity (over 30%) and in wavelength operation range, especially for variation of the refractive index in the range of [1.34,1.36] where the sensor can actually operate at 830 nm

6.4.2 Loss for different concentrations of Al_2O_3 and Ag

The previous section demonstrated the best performance of metamaterial sensors when compared with their metal counterpart, and the increased freedom in designing the sensor, associated with control of the concentrations of the different materials that compose the metamaterial, as well as the layer thickness. This section addresses the characterization of the sensor in terms of the first parameter. Figure 6.5 and Table 6.2 show the light loss through the sensor as function of the wavelength for metamaterials with different concentrations of Ag – Al_2O_3. The results show a red-shift

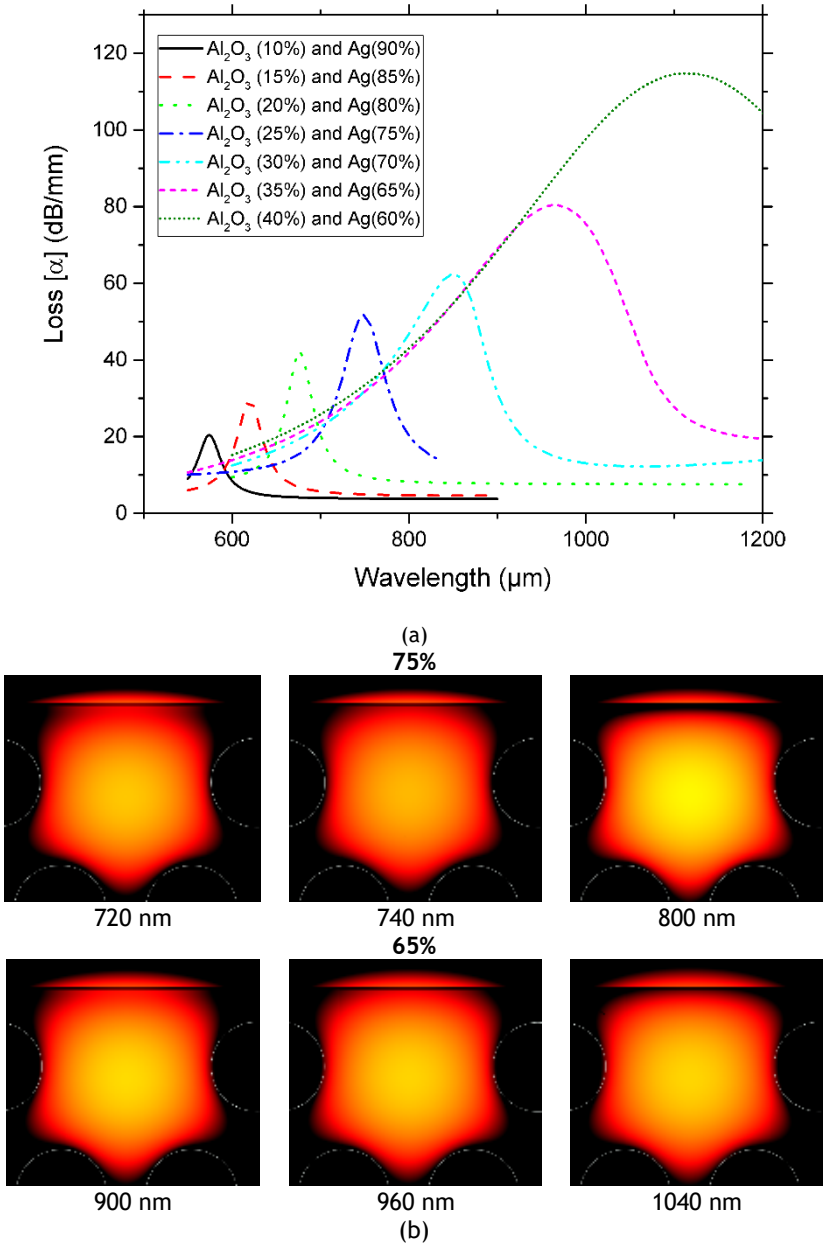

Figure 6.5 (a) Attenuation as function of wavelength for different metamaterial filling ratios for the PCF D-type configuration with n_{ext} = 1.30 RIU. (b) Distribution of light in the region of the center of the fiber and the metamaterial film for two concentrations of Ag (75% and 65%).

in wavelength of the resonance peak for decreasing concentrations of Ag similar to those reported in previous studies [73].

Figure 6.5b shows the distribution of light in the region of the center of the fiber and in the metamaterial film for two concentrations of Ag (75% and 65%). The distribution of light intensity for both concentrations and at different wavelengths are very similar but there are subtle differences when focusing our attention to the region near the metal interface: the intensity gap between the core and the exterior of the metal becomes sharper and the intensity outside increases for higher wavelengths, indicating a change in the nature of the light interaction with the plasmons. The main difference between the two concentrations is the wavelength at which this change in

light-plasmon interaction occurs, which is consistent with the resonance peaks identified in Figure 6.5a.

Table 6.2 Information about the loss peak (α_{peak}), wavelength (λ), 3dB/mm the variation of the loss ($\Delta\lambda$) low and high wavelength with variation of loss 3dB (λ_L and λ_H, respectively) information about narrow of the sensor, extracted from Figure 6.5

Concentration	α_{peak}(dB/mm)	λ (nm)	$\Delta\lambda$ (dB/mm)	λ_L (nm)	λ_H (nm)	$\lambda_H - \lambda_L$ (nm)
Al2O3 10% and Ag 90%	20.422	574	17.422	566.47	581.88	15.41
Al2O3 20% and Ag 80%	41.966	676	38.966	670.87	682.09	11.22
Al2O3 30% and Ag 70%	62.619	850	59.619	834.40	864.10	29.70
Al2O3 40% and Ag 60%	114.730	1115	111.730	1069.00	1159.91	90.91

From Table 6.2 we conclude that metamaterials with higher concentrations of Ag produce narrower resonance peaks, an effect which is especially noticeable for Ag concentration above of 70%. This puts a lower limit to the concentration of Ag, since below this value one obtains wide resonance peaks and strong losses, thus resulting in feeble optical signal and low signal to noise ratios. The best sensing performance occurs for a metamaterial with 20% of Al_2O_3 and 80% the Ag, where the resonance peak is relatively narrow and losses are not excessive. The transition between a narrow and broad resonance identifiable in the loss spectrum described in Figure 6.5a for a metamaterial with increased Al_2O_3 concentrations can be explained in terms of the imaginary part of the dielectric constant, illustrated in Figure 6.2b. For pure silver, the imaginary part for wavelengths above 0.3 microns grows monotonically, resulting in a narrow SPR resonance at lower wavelengths. For a metamaterial with higher concentrations of Al_2O_3, we notice the existence of a feature similar to a concave protuberance in the spectrum of the imaginary part of the dielectric constant, which allows more wavelengths to be near SPR resonance, thus broadening the loss peak observed in Figure 6.5a and blue shifting it.

6.4.3 Loss for different thicknesses of the metamaterial

In this subsection we address the characterization of the metamaterial sensor in terms of layer thickness. The metamaterial thickness is strongly constrained not only by fabrication limitations, but also by the validity of the homogenization model used to compute the optical properties of the metamaterial (see equation 6.3) and the fill ratio *f*) and ultimately by the physical limitations of the nanoscale components of the metamaterial to respond collectively to the optical field and behave as a single bulk synthetic optical material. For example, if we consider the layered medium chosen in this artigo it is not possible to have metamaterial layers of thicknesses of about a few atoms as it would be in the case of a pure metal. Indeed, in such case it would be impossible to pile up sufficient layers of both Ag and Al_2O_3 to obtain an intended value of relative concentration. This could however be overcome by considering other types of metamaterials, such as those composed of metal nanodisks embedded in a dielectric

matrix [73] which would be able to cover the entire range of metal and dielectric concentrations, even for layers with atomic thicknesses, by adjusting the radius and average distance between the metal disks. Then the homogenization model would still be valid but with a different value of form factor f.

Figure 6.6 describes the attenuation through the fiber as function of the wavelength for different values of thickness of the metamaterial (d_m) and shows a slight red-shift in wavelength when the thickness of the metal is increased, although for large thicknesses of the metal the shift is smaller than for short thicknesses.

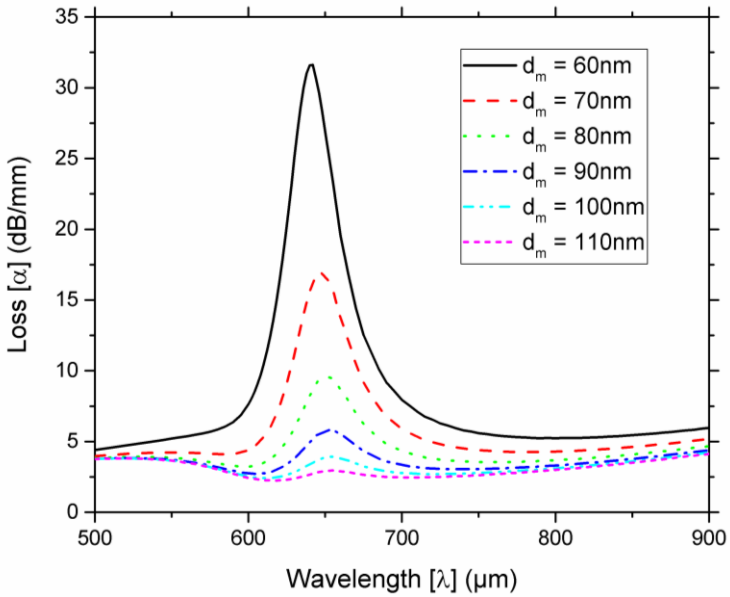

Figure 6.6 Attenuation as function of wavelength for different thicknesses of the metamaterial PCF D-type configuration fiber with n_{ext} = 1.32 RIU and Ag = 90%.

Figure 6.6 shows that the decrease of d_m produces an increase of the intensity of the loss, a phenomenon observed in pure metals [45]. This suggests that it is possible to do some fine tuning of the sensor performance (such as the operation range and the amount of losses) by adjusting the thickness of the metamaterial.

6.4.4 Optimization of the sensor

The two previous sections have shown that it is possible to improve the performance of the sensor by controlling both the concentrations of Ag or Al_2O_3 and thickness of the metamaterial. In this section we combine those results and discuss how they can be used to design a sensor with optimized performance. In particular, it was concluded that the increase in losses associated with decreasing the metal concentration could be partially compensated with an increase in layer thickness. On the other hand, both a decrease in metal concentration and an increase in layer thickness would contribute to a red shift of the peak towards 850 nm. These considerations suggest that the best design parameters to consider when optimizing the sensor performance are, on one hand, the layer thickness and, on the other, the amount of metal per area of the metamaterial film, rather than the actual concentration of metal. A good estimate of the amount of metal per area can be

obtained by the product between the thickness of the layer and the concentration of Ag in the metamaterial, designated by σ_{Ag} =%Ag × d_m.

In Figure 6.7 we have plotted the amount of attenuation of the resonance peak for different values of the product between Ag concentration and thickness. Clearly, the wide majority of these points fall along the same trend line, thus supporting our hypothesis. This shows that the relevant parameter is the total cross section between the optical field and the atoms of metal as the former crosses the layer. In other words, the losses are approximately determined by the amount of metal atoms that interact with the field per unit area and are somewhat independent of whether they are all concentrated in a single metal layer or distributed along the metamaterial. Therefore, the main effect of the metamaterial, when compared to a film of pure metal with the same amount of atoms per unit of surface (and hence with a different thickness) is to red shift the peak of the SPR resonance.

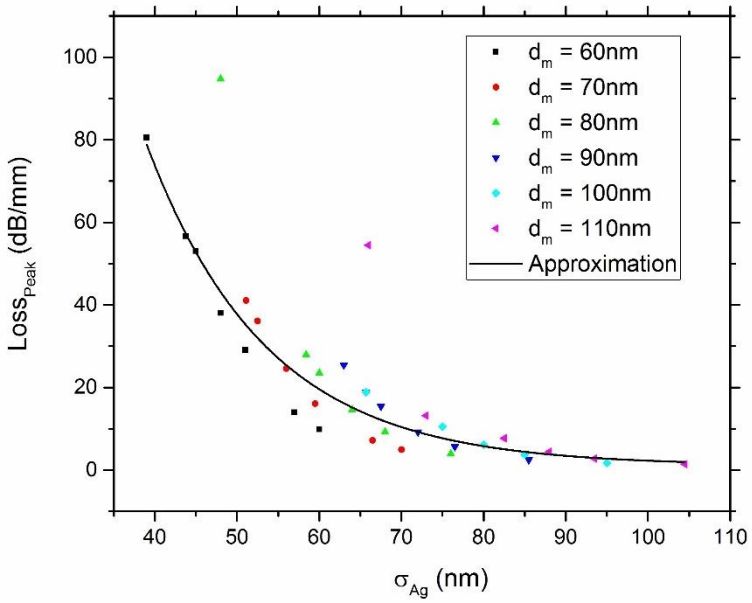

Figure 6.7 Attenuation peak as function of the relative concentration and thickness of the metamaterial with n_{ext} = 1.30 RIU.

To verify this second conclusion, we plotted in Figure 6.8 the peak wavelength as a function of σ_{Ag}. In this case, the points corresponding to different thicknesses fall on similar, yet parallel, trend lines.

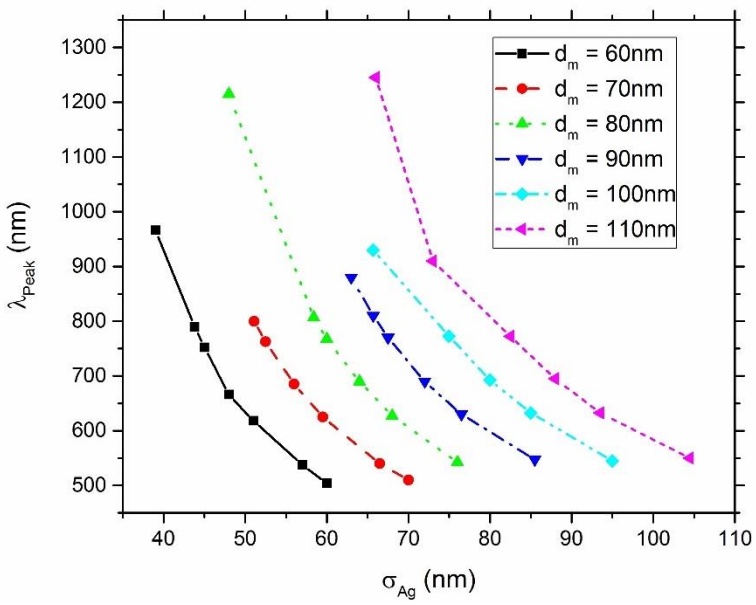

Figure 6.8 The wavelength peak of the attenuation as function of the relative concentration and thickness of the metamaterial for n_{ext} = 1.30 RIU.

The conclusions from Figure 6.7 and Figure 6.8 can now be used in the design and optimization of the sensor by allowing us to choose the thickness of the metamaterial and concentration of Ag that yield the best performance for a given spectral range of operation, as well as, for a specific range of measurement of n_{ext}. For example, to measure an external refractive index around 1.30 RIU using a sensor operating around 700 nm, it is possible to use Figure 6.8 to select a metamaterial thickness of, for instance, 70 nm corresponding to $\sigma_{Ag}\approx$55 nm and a concentration of the Ag of 79%= σ_{Ag}/d_m = 55/*70*. The level of the attenuation at the peak can be estimated from Figure 6.7 to be about 30 dB/nm. For different ranges of n_{ext}, we need to consider the effect of the external refractive index in the sensor performance as illustrated in Figure 6.4.

6.5 Conclusion

The sensor design was composed of a PCF D-type fiber with metamaterial layer, and demonstrated the possibility of controlling the losses and operation wavelength of the sensor over a wide range by changing the relative fraction of the different materials that compose the metamaterial.

From Table 6.2 we conclude that metamaterials with higher concentrations of Ag produce narrower resonance peaks, an effect which is especially noticeable for Ag concentration above 70%. This puts a lower limit to the concentration of Ag, as below this value, one obtains wide resonance peaks and strong losses, thus resulting in feeble optical signal and low signal to noise ratios. Figure 6.7 and Figure 6.8 permit to design and optimize the sensor by allowing us to choose the thickness and concentration of Ag that yield the best performance for a given spectral range of operation, as well as, for a specific range of measurement of n_{ext}.

These results indicate that the use of metamaterials provides not only a way of improving the performance of SPR sensors on optical fibers, but also to adequately control and customize the performance characteristics of the sensor. In practice, the

metamaterial works as an artificial metal with optical properties that cannot be found in natural materials and can be customized to design specifications of the sensor. The analysis of the results provides a method of optimization for choosing the best metamaterial parameters that can be applied in the engineering of these types of sensors.

Chapter 7

Singlemode sensors with wires

In previous chapters we have considered the more conventional design for SPR sensors, based on a planar metal film deposited on the surface of a fiber. Such configurations has been extensively studied in literature and their fabrication techniques are simple and well established [2]. However in the past decade, research into SPR sensors has shifted into other types of sensor design, and among them into the study of sensors based on metallic wires or introducing metallic components with circular profiles. Although more complex than planar metal films, the mode structure of the metallic wires is not too difficult to calculate, since it is mainly determined by the cylindrical geometry of the metal and is therefore very similar to the mode structure of the optical fiber itself.

In this chapter we look into a sensor design which combines a D-type fiber with a single gold wire mounted on the flat surface of the fiber, parallel to the optical axis, and we investigate how the geometrical parameters can be used to increase the sensitivity to the external refractive index. The analysis, based on simulations using a computer model built on Finite Element Method (FEM), implemented in COMSOL Multiphysics [45] focus on loss, sensitivity, resolution and operation wavelength. Once again, this approach allows us to test new sensing concepts and configurations with considerable economy of time and resources, when compared to an exhaustive fabrication and test of all possible designs.

Furthermore, in this chapter we define the method used to determine the multiple modes supported by the metallic wires. In particular, we shall focus on the relevant modes and investigate their optical properties. Based on this study, we propose a new design for a SPR sensor based on metallic wire. In this configuration the wire is incrusted in the surface of the cladding of the fiber, such that it is also in direct control with the external medium.

We have investigated the optimal radius of the wire and the best distance between the wire and the core in terms of loss and wavelength of the SPR. We tested numerically this configuration of SPR sensor in terms of the sensitivity, resolution, operation wavelength, and compared these results with the performance of a convectional SPR sensor based on a planar metallic film.

7.1 SPR sensor based in metal wire

This high interest has been supported by the development of new fabrication techniques of micro and nanoscale metallic structures, and have paved the way to the development of new devices that use the localization of surface plasmons to better control their properties and achieve higher sensing performances. These approaches include metamaterials [99], nano and micro structures with different sizes and forms [100], and their combination with other materials, in a myriad of optical devices, including optical fibers [101]. The performance of these devices based on metallic sub-micron structures depends strongly on the fine control and optimization of geometrical parameters such as the dimensions or relative positions of the components, thus promoting numerical simulations as the preferred method to explore new sensor designs in order to reduce time and development costs [20], [97].

Today's fabrication techniques offer many geometries for the metal components, ranging from wires and disks to spheres and grooved surfaces, which can be used to customize the modal dispersion of the plasmons and increase their coupling with light. In particular, it is possible to couple the modes of a step-index fiber with those of a metallic wire at certain wavelengths, when some of these modes become phase matched. Also, metallic wires support multiple modes which permit an increased number of resonant peaks [102], and result in sensors with different values of sensitivity, operation wavelength and RI detection range, among others [55], [103]. Some new fabrication techniques (like spliced-fiber with pressure-filling [104], stack-and-draw technique [105] or pressure assisted melt filling (PAMF) [106]) increased the possibility of creation of new configurations with more complex geometries allowing us to produce virtually any nano-structure on an optical fiber [28], [107].

Theoretical and experimental study of the plasmon modes on single wires have begun in the 70s [141]. Many of the studies of the metallic wires focus on the study of the two materials (Metal/Silica) [102], interacting with a singlemode fiber [105] or with photonics crystal fibers (PCF), but without studying the possibility of the creation of an SPR sensor.

SPR fiber sensors based on metallic wires can be found in the literature, for instance, Luan [142] presented a microstructured SPR sensor where the silver wire is placed on top of the fiber. Also in [74] Luan study another SPR sensor based on a wire localized inside the hollow fiber. In these two cases the wire is completely exposed, which has the drawback of reducing the robustness of the sensor. Lu [121] presented another refractive index sensor based on a grapefruit photonic crystal fiber where the holes are filled with silver wires.

7.2 Singlemode fiber sensor based in SPR with a metal wire on a D-type fiber

We consider the design of the refractive index optical sensor compounded of a D-type fiber profile with a gold wire mounted on the flat surface, and thus replacing the metallic film usually considered in literature [45]. The fiber is made up of a conventional step index fiber compounded by the core, with silica doped with 16% germanium (n_{co}), and surrounded by a pure silica cladding (n_{cl}), whose refractive

indexes were calculated using the Sellmeier equation (see equation 3.25). The effective refractive index (n_m) of gold is calculated using the Drude equation (see equation 3.30). The wire is partially embedded on the surface of the fiber to improve mechanical resistance of the device as well as the optical coupling both to the core and to the external medium (as illustrated in Figure 7.1). In the computer model, the space surrounding the fiber is filled with the analyte, characterized by an external refractive index n_{ext}. The relevant geometrical parameters are the distance between the center of the fiber and the center of the metal d, the radius of the core r_{co} and the radius of gold wire r_E.

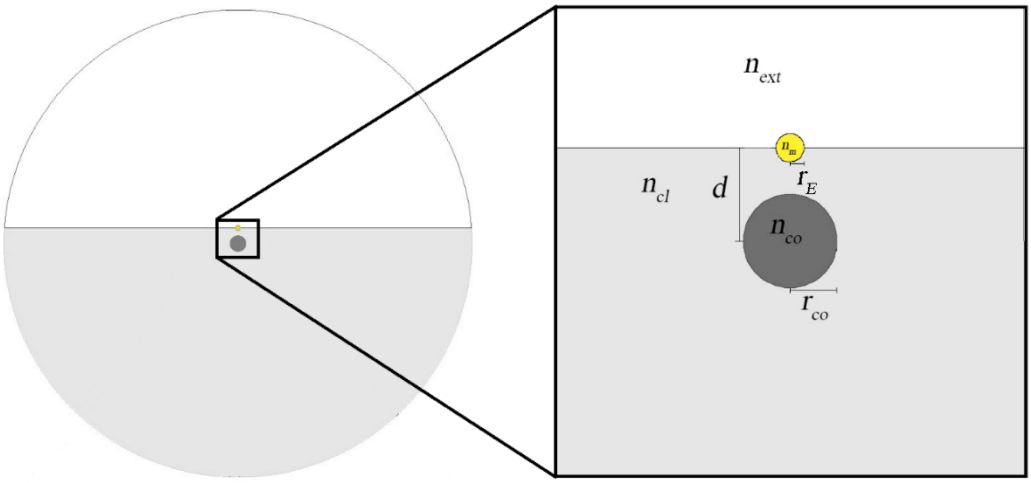

Figure 7.1 Schematic of the SPR D-type fiber with a gold wire configuration, with the inset of zoom of the core and metal wire.

The study is based on the calculation of the guided modes taking into account both the D-type fiber and the wire, referred as supermodes (SMs), since they correspond to the hybridization of the individual modes of each of the structures that compose the device taken isolated, namely the fundamental guided mode of the fiber and the plasmon modes in the metal wire. All these modes are calculated numerically by solving the wave equation for the Fourier components of the electric field (equation 3.73).

7.2.1 Description of the isolated modes and the supermodes

In this section we investigate the real and imaginary part of the refractive index of the sensor in terms of the number and characteristics of the resonance peaks, and compare the performance of the sensor with the configuration most commonly described in literature, specifically a D-type fiber covered with a metal film [45].

Figure 7.2a shows the RI real part of the plasmon modes of the wire (m = 0, 1, 2) and the fundamental mode of the optical fiber. Figure 7.2a also shows the RI imaginary part of the sensor as function of the wavelength between 600 and 950 nm. The crossing between the dispersion curves of the modes of the metal wire and the fundamental mode of the fiber are indicated by squared dots. These correspond to the peaks designated by the circular red dots in the imaginary part of the effective refractive

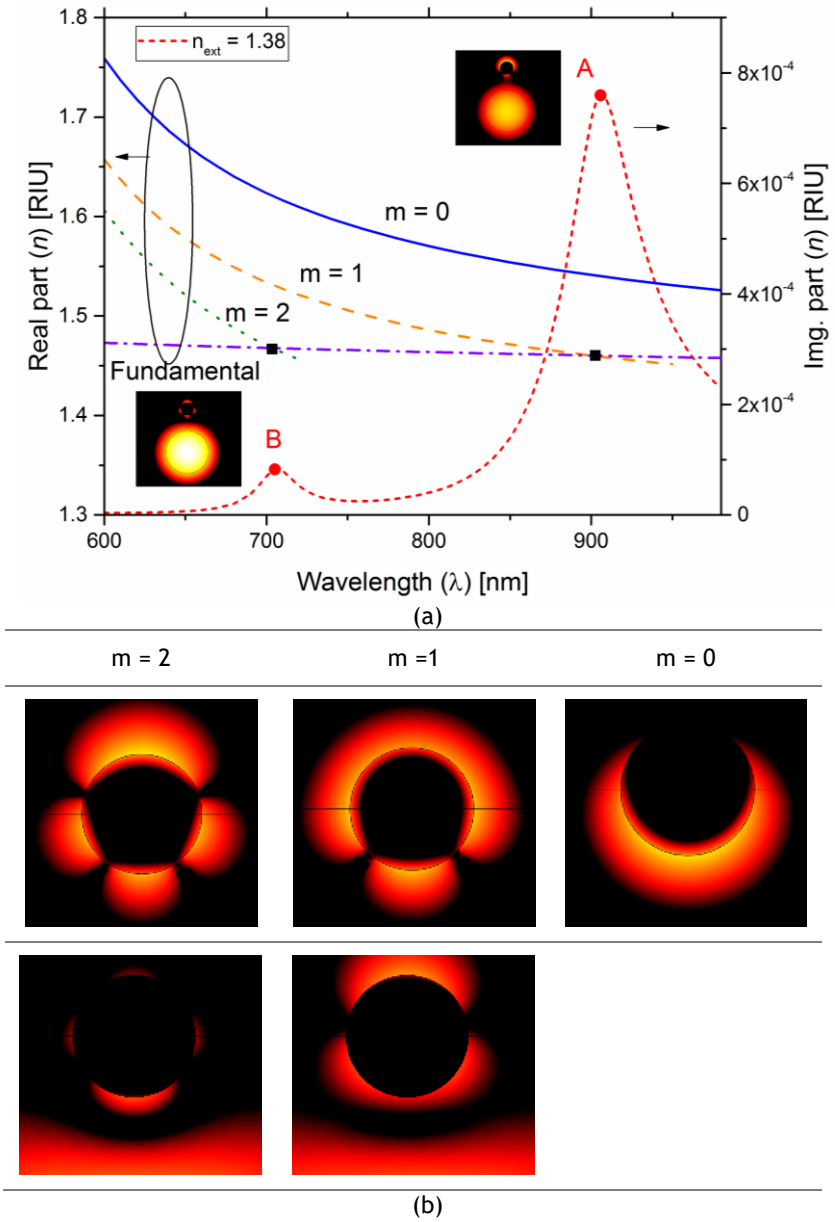

Figure 7.2 (a) Real and imaginary part of the refractive index of the sensor as function of wavelength for external refractive index of 1.38. (b) Detailed distribution of the light intensity in the metal wire for the plasmon modes of the wire (top) and the resulting modes after hybridization with the fundamental mode of the fiber (bottom).

index of the sensor (red dashed line), thus indicating a resonate coupling. The results show that only the plasmon modes of the metal wire with m = 1 and m = 2 can couple to the guided modes of the fiber and therefore participate in the sensing process. That means the two points of phase-matching (black square dots in Figure 7.2a), and the two resonance peaks (red circle dots in Figure 7.2a) indicate the existence of two supermodes (SM1 and SM2).

Figure 7.2b presents a detailed distribution of the light intensity in the metal wire for the plasmon modes of the wire and the resulting modes after hybridization with the fundamental mode of the fiber. Although the hybridization introduces a distortion in the light distribution, it preserves the dipolar and quadrupole features of the plasmon modes. An inspection of the field distribution in Figure 7.2b shows the transition between the two supermodes. They correspond to a mode with a strong

dipolar moment (peak A) and another with a strong quadrupole moment (peak B), which are illustrated in Figure 7.2b [102]. However, this coupling is not exclusive and indeed each of the supermodes results from a combination of all three modes (a guided mode and the two plasmon modes). In this work, we focus on SM1 (peak A, corresponding to a mode with a high dipolar mode) because it has a better potential for sensing due to the higher attenuation.

7.2.2 Effects of the different parameters

In literature the two main parameters considered in the study of the SPR D-type fiber sensor with a metal film are the thickness (in our proposal, corresponding to the radius of the wire) and the distance between the waveguide and the interface metal/external refractive index [1]. In the case of the sensor with a metal film, the study of the effect of these parameters and others are well detailed in literature [1]. In the case of the metal wires, some studies can be found. For example Schmidt in [102] studied the effect of the diameter of the wire embedded in silica in the SPR, while Luan in [142] positioned the wire in the external medium. However, no study considers a wire anchored between the two media, namely the cladding and the external medium, as illustrated in Figure 7.1.

Figure 7.3 presents the behavior of our sensor proposal with a metal wire anchored between the two media for different distances of the metal wire relative to the center of the core (Figure 7.3a) and for different values of the radius of the wire (Figure 7.3b). Figure 7.3a also shows the light intensity distribution along a cutplane of the sensor.

In Figure 7.3a it is possible to observe that the intensity of the loss is reduced for larger distances between the wire and the core, which is similar to the effect observed in SPR D-type fiber sensors based on metallic films [45] when increasing the distance between the core and the film. For the second peak (SM1), the values of d shorter than 2 μm imply an excess of losses that limit a practical sensor, so we fix d = 2 μm, which yields a value of loss similar to those found in literature [143].

The results in Figure 7.3b show a stronger shift in wavelength of the supermode with dipolar moment (SM1) for larger wire radius, especially when compared with the smaller wavelength shift observed for the supermode with quadripolar moment (SM2), resulting in a higher sensitivity for supermode SM1. Comparing the shifts in wavelength of the second peak (SM1) produced by changes of external refractive index in wires with different radius, it is possible to conclude that the best sensitivities are obtained for r_E =300 nm. Therefore, the radius of the gold wire was set to be r_E = 300 nm, which is compatible with the current fabrication techniques [14, 18].

To identify the advantages of the metallic wire, we compare the performance of our sensor with an analogous design also based on a D-type fiber but with a metal film with 45 nm of thickness mounted on the flat surface. Indeed, in literature, the metal films of these type of sensors range from 45 nm to 60 nm, depending on the fabrication techniques and whether combine metal or other types of coupling layers, to further boost performance [1], [143]. We have chosen the value of 45 nm to gauge the improvement in sensing performance of our proposal against the best performing sensor with a film without coupling layers [45], [143]. Both the reference sensor and

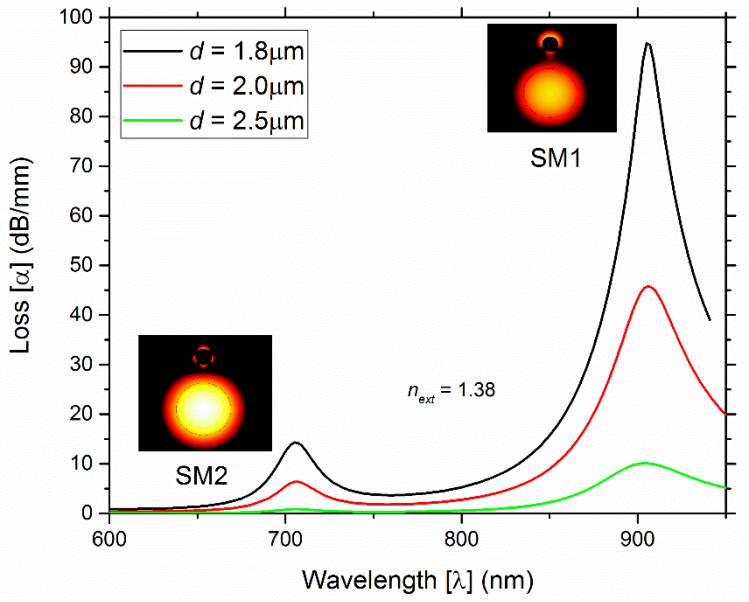

Figure 7.3 Attenuation curves as a function of wavelength for different distances between the center of the metal with the center of the fiber core (a) and for different radius of the metal (b). In the inset of Figure 7.3a, it is also shown the intensity of the electric field distribution along a cutplane of the sensor, corresponding to the supermodes of the two peaks (SM2 and SM1).

our proposal consider d = 2 μm and r_{co} = 1 μm. For these structural parameters and for n_{ext} = 1.38 the wire supports three modes in the spectral range between 600 and 1000 nm and with two SMs, as shown in Figure 7.3 [102].

7.2.3 Resolution, sensitivity and operation range

We can calculate the Attenuation as a function of the wavelength for different values of the external refractive index considering the propagation of light through a fiber length of L = 1 mm, as shown in Figure 7.4. The figure shows the comparison between the attenuation curves as function of wavelength for two configurations of sensors, one with the metal wire (as described in Figure 7.1) and another where the

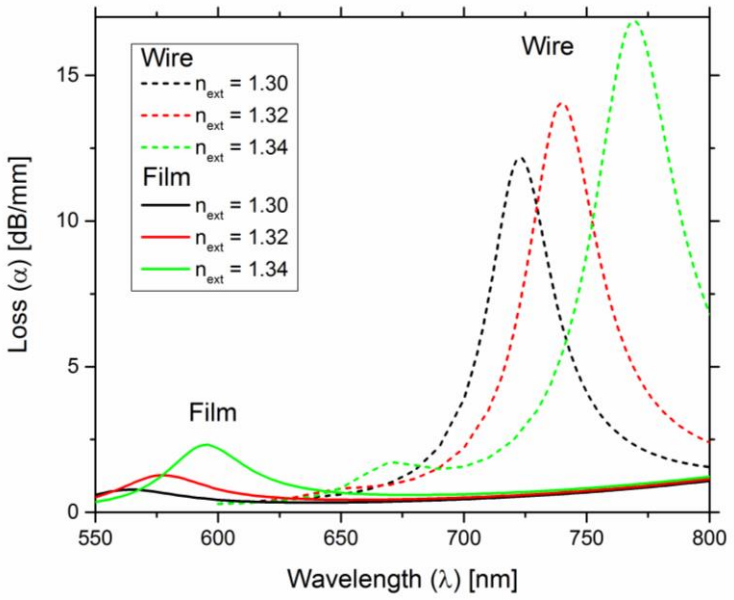

(a)

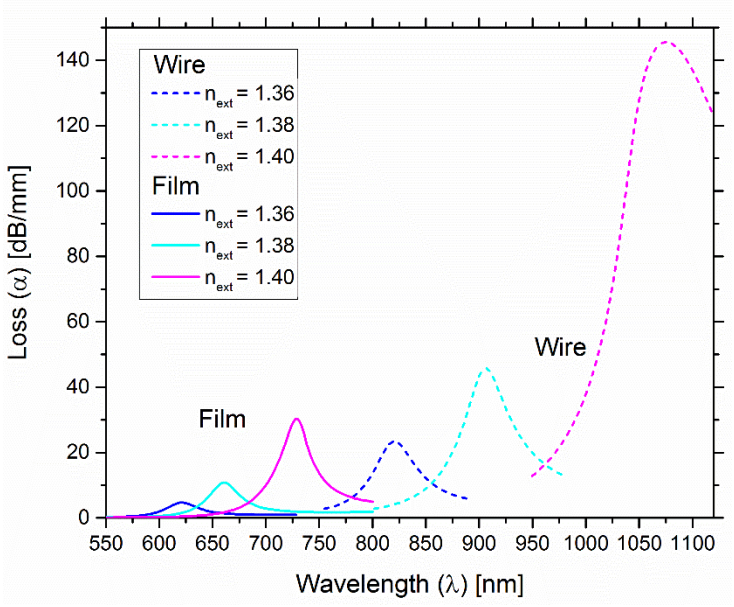

(b)

Figure 7.4 Comparison between the attenuation curves as function of wavelength for two configurations of sensors, one with the metal wire (dotted curves) (as described in Figure 7.1) and another where the wire is replaced by a metal layer/film with 45 nm of thickness (solid curves). The external refractive index varies between 1.30 and 1.34 in Figure 7.4a and between 1.36 to 1.40 in Figure 7.4b.

wire is replaced by a metal layer/film with 45 nm of thickness, for different ranges of the external refractive index, 1.30 to 1.34 and 1.36 to 1.40, shown in Figure 7.4a and Figure 7.4b, respectively.

In Figure 7.4a the results show that the sensor with the metal layer only supports one resonant peak for this spectral range, whereas the sensor with the metal wire supports two, both of which can be strongly shifted in wavelength by a change in the external refractive index. For the peak in the right, this shift is complemented by an increase in the losses for higher refractive indexes. Figure 7.4b shows that for external refractive indexes above 1.36 these effects are even stronger, indicating better

sensitivities. Figure 7.4 also indicates that the design with the metallic wire provides a stronger coupling (higher losses) between the plasmons modes with the external medium and the fundamental mode than the design with a metallic film. In both cases, the fine tuning of the amount of losses can be done by varying the spacing between the metal and core, as shown before in [45] for the metal film and in Figure 7.3b for the metal wire.

The values of sensitivity, sensor resolution and spectral operation range for the two designs are presented in Table 7.1, for different intervals of external refractive index.

Table 7.1 Sensitivity, resolution and range of wavelength values for the refractive index optical fiber sensors based on two forms of metal inclusions (film with 45 nm of thickness and wire with 300 nm of radius).

	Sensitivity (nm/RIU)		Resolution (RIU)		Range λ (nm)	
Range of n_{ext}	Film	Wire	Film	Wire	Film	Wire
[1.30,1.32]	700	891	1.4×10^{-5}	1.1×10^{-5}	560-580	720-740
[1.32,1.34]	900	1437	1.1×10^{-5}	7.0×10^{-6}	580-600	740-770
[1.34,1.36]	1300	2562	7.7×10^{-6}	3.9×10^{-6}	600-620	770-820
[1.36,1.38]	2000	4287	5.0×10^{-6}	2.3×10^{-6}	620-660	820-900
[1.38,1.40]	3200	8437	3.1×10^{-6}	1.2×10^{-6}	660-720	900-1070

The sensitivity and the resolution were computed using equations 3.71 and 3.72, respectively, and assuming that it is possible to detect experimentally a spectral variation of 0.01 nm. The results clearly show that the sensor with the metallic wire with 300 nm of radius outperforms its counterpart with a metallic film with 45 nm of thickness in all situations, as expected from Figure 7.4.

7.3 Conclusion

The results in this chapter reinforce a new trend in the field of SPR sensors that claim that replacing a metal film with a nanoscale metal structure can increase tremendously the sensitivity of the sensor, not only by increasing the shift of the plasmon resonance wavelength when the external refractive index changes, but also the amount of losses that are also increased. The main advantage of nanoscales metal structures is that they can support several plasmon modes which are strongly dependent on the geometry and therefore are more dramatically affected by changes in the boundary conditions of the field. Also, by carefully controlling the geometrical parameters of the metal structure, such as size, it is possible to improve the phase/dispersion matching between plasmon modes in the metal and the guided modes in the fiber, producing a stronger coupling between them. As a result, the supermodes that are produced by the hybridization of the plasmon and guides modes,

are strongly dependent on the external refractive index, which in turn ensures a dramatic increase of the sensitivity of the sensor, relative to more conventional configurations.

In particular, and comparing the configurations of Table 7.1, for the low values of the external refractive index, for example n_{ext} = [1.30, 1.32], the metallic wire D-type fiber sensor showed a higher performance, enhancing the sensitivity from 700 to 892 nm/RIU, when compared with metallic film. For higher values of the external refractive index (n_{ext} = [1.38, 1.40]) our sensor presents a sensitivity of 8437 nm/RIU, that compares with the 3200 nm/RIU obtained for the sensor based on the metal film, and about 1.4 times better than the results obtained in reference [143] using Bk7, where a sensitivity of 6000 nm/RIU was obtained. In terms of resolution, the design based on the wire presents better values in all ranges, when compared with the metal film configuration.

Finally, and as shown in Figure 7.2, the multiple modes supported by the metallic wire permit to develop several sensors for different wavelengths of operation by using distinct modes of resonance.

Chapter 8 Multimode sensors with wires

Throughout this thesis we have systematically investigated the main aspect and design features that can contribute to an improvement in performance of SPR fiber sensors. We started in **Erro! A origem da referência não foi encontrada.** with the most basic and well studied configuration of this type of sensors, namely a sensor composed of a thin film deposited on the side of a single mode fiber, and investigated how the thickness of this film can be optimized. Then, in **Erro! A origem da referência não foi encontrada.** we have shown that is possible in a multimode fiber to introduce another important degree of freedom: the choice of the optical mode used for sensing. In a multimode fiber the total sensitivity of the device results from average of the distinct sensitivity of each of the modes supported by the fiber. In the previous chapter, we have replaced the thin metal film in a singlemode fiber with a metal wire, which can support multiple plasmonic modes. Again we have shown the importance of selecting a specific mode to increase the sensor performance, but this time we have looked into a choice of the most appropriated plasmonic mode. In this chapter we combined the results of previous chapters and investigate a device that can support both multiple optical and plasmonic modes.

Indeed when we look into the research reported in literature of the strong coupling between the optical mode guided in the core of the fiber and the SPR modes supported by the metal nanostructures that compose the sensors, we notice that much of the focus is on the search for the geometry of the metal nanostructures that favor this coupling and most only consider singlemode fibers. However, little has been investigated in how to manipulate the nature of the guided modes to improve the sensing performance, for example using higher order modes in a multimode core rather than the fundamental mode supported by single mode fibers.

The study of the distribution of light in a multimode fiber and the contribution of individual modes in the SPR effect has been not yet studied, because there is little work in filtering particular modes in a multimode fiber. Fontana developed a theoretical model to determine the distribution of light in a multimode fiber, but the study is applied only in a few modes [127]. Mao *et al*. studied the modes found in a multimode fiber SPR sensor and observed that, for different external refractive indexes, all the modes presented a similar change in characteristic wavelength and only a variation occurred in the amplitude of the loss. As a result, the calculation of the sensitivity was performed for only one mode, since all the other modes presented similar values [144]. Cennamo *et al*. reached the same conclusion in the numerical simulation [109]. The problems with the numerical study of a multimode fiber SPR

sensor are the large dimension of the model (core and film of the metal have hundreds of μm), and the size of the elements in the mesh need to be at least 10 times inferior of the wavelength of the sensor (a few nm), that means, very small size elements and a fairly large number of them [45]. These two characteristics in conjunction are not easy to simulate with the FEM, since it requires a lot of computing time and memory to perform the study. One solution is to optimize the mesh so that the small elements are located only in the important areas. The problem with this approach is an increase of the computation of error.

The singlemode fiber SPR sensor with a metallic wire was presented in the previous chapter and we have shown that the confined nature of the plasmon modes in nanowires could provide a stronger coupling between light and the plasmons. Based on those results shows on **Erro! A origem da referência não foi encontrada.**, we investigate, in this chapter, the occurrence of multiple modes found in a plastic and silica multimode optical fiber and the effect of the SPR in some modes of interest. To our knowledge, the study of a multimode fiber with a metallic wire to form an SPR fiber sensor has not been studied yet. We also compare the sensitivity, resolution and the wavelength range when using the fundamental mode or other higher mode.

8.1 Optimization of modal sensitivity in nanowire SPR multimode sensor

In this section, we investigate some modes of interest found in a multimode fiber, which in conjunction with a metallic wire are able to form an SPR sensor. We also compare the sensitivity, resolution and the wavelength range of the SPR sensors when using the fundamental mode or another higher mode of the multimode fiber.

8.1.1 Design parameters

We consider a D-Type, step-index core multimode fiber, where a wire of gold (radius ≈ 300 nm), parallel to the core, is deposited [105]. The fiber arrangement is shown in Figure 8.1.

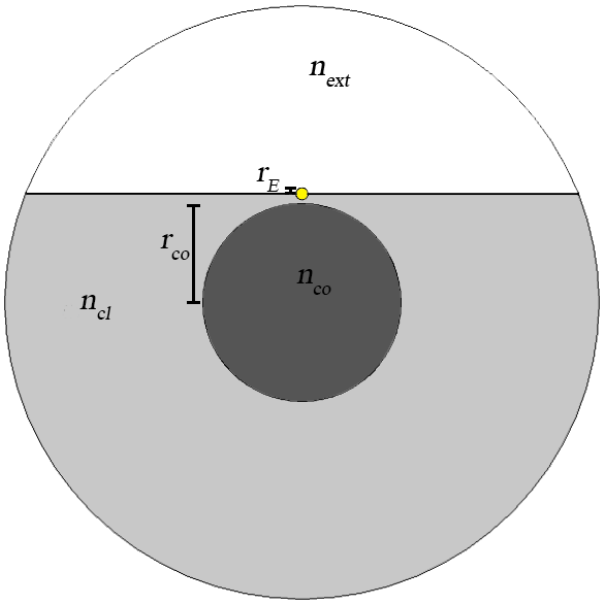

Figure 8.1 Schematic of the proposed SPR D-type multimode fiber.

The fiber structure is composed by a core (silica doped with 16% GeO_2) with refractive index n_{co} and by a cladding (pure SiO_2) with refractive index n_{cl}, both calculated using the Sellmeier equation 3.25. The complex refractive index of the wire (gold) is denoted by n_m and is obtained from the Drude model of equation 3.30. The distance between the center of the core and the center of the wire is d. The radius of the core is r_{co}, the radius of the wire is r_E and the refractive index of external medium is n_{ext}.

8.1.2 SPR in the multimode fiber

Using equation 3.36 with the parameters d = 5.5 μm, r_E = 300 nm, r_{co} = 5 μm and n_{ext} = 1.34, it is possible to obtain Figure 8.2. This figure shows the loss as function of wavelength for different modes found in the multimode fiber. The modes are named accordingly with the direction of the incident beam (p or s), number of rings and the number of spots in the core border. For example, in Figure 8.2, the red dashed line is mode $M_{P,3,5}$. Also Figure 8.2 shows also the distribution of the light and the loss of six modes found in the multimode fiber. From left to right the modes go from the fundamental mode to the chosen higher order modes.

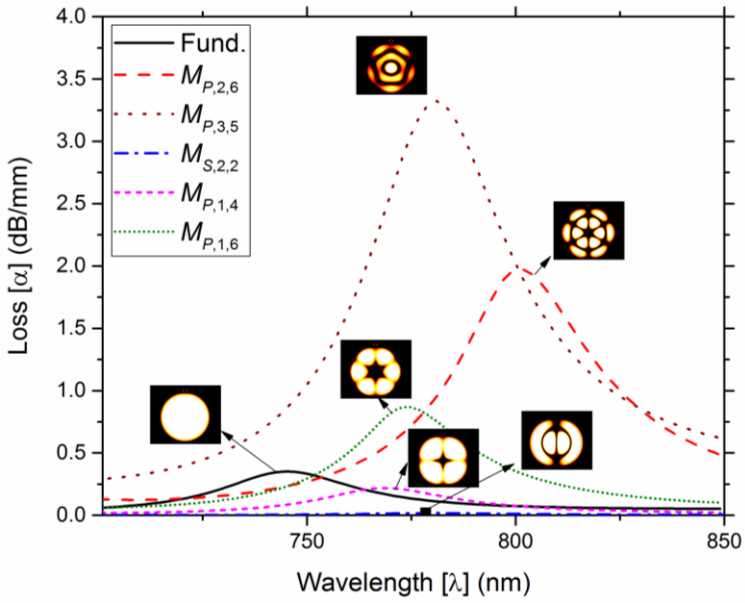

Figure 8.2 Attenuation as a function of wavelength for different modes. The distribution of light intensity for each different mode is also presented.

These light distributions show that for higher order modes, the effect of the wire in the light distribution is more noticeable due to the break of symmetry. For example, mode $M_{P,3,5}$ shows clearly a break in the symmetry of the light spot. This symmetry break can produce an increase or a decrease in the RIU detection due to the different energy that reaches the external medium. Also, we can observe that higher order modes with a *p*-polarized (M_P) present a higher magnitude of loss and a shift to longer wavelengths when compared with the fundamental mode. The mode with a *s*-polarized (M_S) has a very low loss, but maintains a shift to the right when compared with the fundamental mode.

8.2 Sensitivity of two modes in the SPR multimode fiber

In this section, we study the fundamental mode and $M_{P,3,5}$ mode, considering only one mode is propagated in the fiber at a certain time. Figure 8.3 shows the attenuation as function of the wavelength for different values of external RI.

Figure 8.3a shows the behavior of the sensor for the fundamental and the $M_{P,3,5}$ modes. Figure 8.3b is a magnification of Figure 8.3a for the fundamental mode. In this case, the resonance occurs when the effective refractive index of the wire is equal to the effective refractive index of the fiber [107]. Mode $M_{P,3,5}$ has a maximum of loss of 9.5 dB/mm and the max loss of the fundamental mode is 0.62 dB/mm. In wavelength: the shift of the sensor from 1.30 to 1.38 RI is 725 to 950 nm and 710 to 850 nm for the $M_{P,3,5}$mode and for the fundamental mode, respectively. In both parameters of measurement (loss and wavelength shift) mode $M_{P,3,5}$ presents better characteristics. Figure 8.3c represents the distribution of light intensity for the mode $M_{P,3,5}$ and the fundamental mode.

Other parameters of comparison are the sensitivity, the resolution and operation range of the detection of the sensor. The sensitivity and resolution can be calculated using equation 3.71 and equation 3.72, respectively. The minimum value of the

experimental detection considered was 0.01 nm. Using theses equations and the information extracted from Figure 8.3a and Figure 8.3b we can build Table 8.1 showing the sensitivity, resolution and range of wavelength for different values of the n_{ext}.

Table 8.1 shows a better sensitivity, resolution and wavelength range for the mode $M_{P,3,5}$. The sensitivity for the [1.36, 1.38] range of n_{ext} for the fundamental mode is 3110 nm/RIU, while for mode $M_{P,3,5}$ is 5340 nm/RIU. To our knowledge, this configuration presents one of the highest values for sensitivity found in literature, for the considered RI range, using sensing configurations based on SPR fiber sensors with a metal wire or film [107], [145].

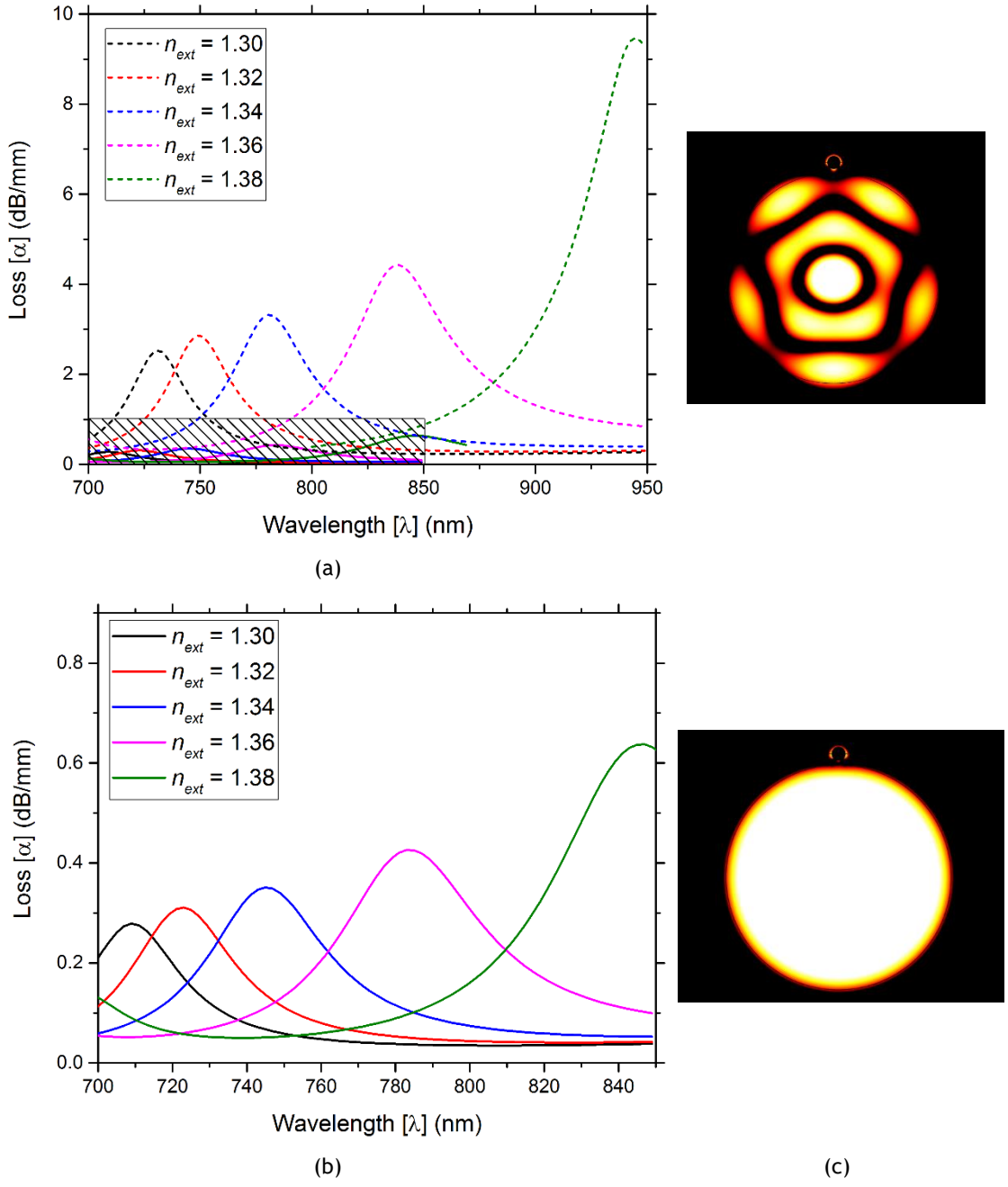

Figure 8.3 Attenuation as function of wavelength for different values of the external refractive index for: (a) the fundamental mode (solid line) and the $M_{P,3,5.}$ (dashed line), (b) magnification of the fundamental mode behavior. (c) The distribution of light intensity for the $M_{P,3,5}$ mode and the fundamental mode.

Table 8.1 Sensitivity, resolution and wavelength range for the fundamental and $M_{P,3,5}$ modes

	S(nm/RIU)		Resolution (RIU)		λ Range (nm)	
Range of n_{ext}	Fundamental	$M_{P,3,5}$	Fundamental	$M_{P,3,5}$	Fundamental	$M_{P,3,5}$
[1.30, 1.32]	680	910	1.47×10^{-5}	1.10×10^{-5}	700-720	731-750
[1.32, 1.34]	1120	1580	8.93×10^{-6}	6.33×10^{-6}	720-745	750-780
[1.34, 1.36]	1930	2860	5.18×10^{-6}	3.50×10^{-6}	745-780	780-840
[1.36, 1.38]	3110	5340	3.22×10^{-6}	1.87×10^{-6}	780-850	840-945

The challenge of this configuration is to cancel the noise caused by the multiple modes that propagate in the core, which originates a low sensitivity and low loss. Considering Cennamo *et al*. work in [109] it is possible to filter a group of modes, which in our work will result in a sensor with increased performance, better sensitivity, resolution and operation wavelength range.

8.3 Conclusion

The techniques more common to improve or to optimize the characteristics of the SPR sensors are focused on the optimization of geometric parameters, like the distance between core and the metal or the external medium, thickness of metal, type of materials to generate the SPR, structure of the sensor, type of overlayer, among others. In most of these cases, the fundamental mode is always present. The results in this work show a new approach to optimize an SPR sensor, using the selection of higher order modes in a multimode fiber. The higher order modes have characteristics that can increase the interaction of the external medium with the waveguide (core), because more optical power is localized in the core boundaries, at the same time the metal wire change the conventional distribution of light in the multimode fiber.

This new approach permits to enhance the performance of the sensor by increasing the sensitivity, resolution and operation wavelength range. Comparing the results of Table 8.1, the $M_{P,3,5}$ mode showed a higher performance when compared with the fundamental mode, enhancing the sensitivity from 680 to 910 nm/RIU for n_{ext} = [1.30, 1.32] and from 3110 to 5340 nm/RIU for n_{ext} = [1.36, 1.38]. In terms of resolution, the design based on the wire also presents better values in all ranges, showing a value of 1.87×10^{-6} for n_{ext} = [1.36, 1.38]. The challenge of this approach is the required filtering to select the appropriate modes to enhance the sensor operation.

Chapter 9 SPR sensor with wires for simultaneous measurement of refractive index and temperature

The previous chapters have pursued the optimization of SPR sensors in optical fibres by exploring the coupling between light and plasmonic modes in different ways. However one aspect has remained constant: SPR sensors are sensitive mainly to refractive index of an external medium. Not surprisingly, many of the SPR sensors designs targeted at measuring other physical, chemical or biological parameters are based on finding ways for these parameters to affect the refractive index of a test medium. Therefore, these SPR sensors measure a wide variety of parameters indirectly.

However, one must not think that plasmons are only responsive to changes in the optical properties of materials in the vicinity of the metal surface, since the electrical characteristics of metals can also be altered by factors such as temperature. Indeed, in real SPR sensors the measurement of refractive index is affected by the temperature of the external medium, which may heat or cool down the metal, altering the density of conduction electrons and ultimately changing the resonance conditions between light and the plasmons. For most metals, this is a secondary effect but that can still introduce readout errors in the values of the refractive index. The solution to this problem is to measure simultaneously and independently both the external refractive index and the temperature, and use the latter to calibrate dynamically the former. In other words, to correct the measurement of refractive index by incorporating information about the temperature.

In most situations the measurement of temperature is done using sensing principles other than SPR. On the other hand, a recent trend in the field of optical sensing is the attempt to integrate multiparameter sensing in a single device. However, most of these are not constituted by a single sensor that measure different parameters but rather a sequential or parallel combination of multiple sensors, each targeting a single parameter. This is the same type of solution used in more sophisticated SPR sensors to discount the impact of temperature from the measurements of refractive index, as previously mentioned.

In this chapter we use the know-how acquired throughout this thesis to address these issues and propose a design of a single fiber sensor that measures simultaneously

and independently refractive index and temperature using SPR as sensing principle. In more detail, we developed a sensor combining several metallic wires that exhibit resonance peaks in different wavelengths. We show that one of these peaks is practically only sensitive to the refractive index whereas the other practically only responds to changes in temperature. This is achieved by allowing one wire to be partially incrusted at the surface of the fiber cladding and in direct contact with the external medium (this wire is responsible for the measurement of the external refractive index), while the other wires are completely inside the fiber cladding (this set of wires is responsible for the measurement of temperature). We follow the approach detailed in Chapter 7 to investigate the coupling between the wires modes and the single mode fiber for our SPR sensor, by studying the impact of the wire radius and distance between the wire and the core in the sensor attenuation and on the wavelength of resonance and ultimately in the sensor performance.

In this chapter we continue to use the method to determine the multiples modes in the metallic wires with different peaks of resonance in different wavelengths, to measure in each peak two parameters: the external refractive index and the temperature. We have improved the method to define multiple peaks with multiple wires.

9.1 Introduction of the SPR sensor for measurement of temperature

In the past years, there has been much research in the development of refractive index sensors based on surface plasmon resonances (SPR) because of their high sensitivity [1]. SPR sensors use the excitation of a charge-density oscillation (i.e., surface-plasmon wave) along the metal-dielectric interface by p-polarized light, which satisfies certain resonance conditions dependent on the geometric and optical properties of the components and of the analyte medium [25], [115], [146]. This type of sensor is also used as a biosensor, and consists in one ligand layer, immobilized over the metal, and the analyte flows across it; the changes in the refractive index of the solution allow to characterize the analyte [33]. These sensors can also be adapted to measure other parameters, such as temperature [28] and pressure [147], typically by including components whose size and optical properties strongly depend on each of the desired physical parameter [148]. One of the challenges remaining is the development of simple sensing configurations that can measure simultaneously more than one parameter, such as refractive index and temperature. In fact, the influence of temperature in changing the dimensions and optical properties of the components of the sensor has many times been considered to be an engineering problem that limits the operation of the sensor. For this reason, there is a necessity to have simultaneous measurement of temperature and refractive index.

Sensors based on SPR are notorious for having high sensitivity to variations of refractive index, but the direct impact of temperature changes on the modal structures of surface plasmons results from a combination of a small change in the optical properties and the thermal expansion of the metal. These produces very small wavelength shifts in the plasmon resonances when compared with those produced by

changes in the refractive index. One solution is to use separate sensors to do independent measurement of refractive index and of temperature, using distinct sensing principles. Temperature measurements are usually based on sensor components that have large thermo-optical or thermal expansion coefficients, usually interferometric in nature and including optical fiber gratings, such as fiber Bragg gratings (FBGs) and long-period fiber gratings (LPGs), as well as, multimode interference and high-birefringence fiber loop mirrors [149], [150].

In SPR sensors, variations of temperature change many of the properties of the fiber (via thermo-optic effect) and of the metal (via phonon–electron scattering along with electron–electron scattering), thus affecting wavelength interrogation, and therefore the sensitivity. In sensors supporting localized SPR, thermal expansion of the different materials may alter dimensions and even further affect the operation of the RI sensor [151].

In this chapter we address two main challenges: First to measure simultaneously temperature and refractive index of the analyte medium; Second, to have plasmon resonances that present strong dependency to just one of the physical parameters under analysis and thus separate their measurement. In our proposal, we consider a fiber sensor combining multiple metal wires and supporting several SPR resonances, that allows us to use two wavelengths to measure both temperature and refractive index simultaneously.

9.2 Consideration of temperature in the calculation

In **Erro! A origem da referência não foi encontrada.** we presented the equation of Sellmeier and the model of Drude for the characterization of the materials in our sensor, and considering the temperature does not change. In this section, we explain the temperature model and the contributions from the thermo-optic effect in the fiber and in the sensing layer. The calculations are done in two steps: first, we calculate the optical properties of the different materials for a given temperature, including the contributions of the phonon–electron scattering and the electron–electron scattering in the case of the metal, and second, we use these values in a computer model based on FEM and implemented in COMSOL to determine the solutions of the electromagnetic field equations, corresponding to the optical modes of the sensor.

9.2.1 Sellmeier equation with temperature variation

We consider a fiber core of pure silica with a 16% doped GeO_2-SiO_2 glass and the cladding is made out of pure silica. The dependence of the refractive index with wavelength of pure silica and *X* doped with GeO_2-SiO_2 glass follows the Sellmeier relation according to equation 3.25. The values of these parameters are represented in Table 3.1. The effect of temperature in the fiber is defined using the thermo-optic coefficient (1.28×10^{-5} K) [88], [151].

9.2.2 Drude model with temperature variation.

In describing the optical properties of the metal and its dependence on the temperature we adopted the model by Alabastri in [152]. The complex and frequency-

dependent dielectric function of any metal can be appropriately represented by the Drude-Lorentz formula as function of the frequency (ω):

$$\varepsilon_r(\omega,T) = 1 - \frac{\Omega_p(T)^2}{\omega[\omega - i\Gamma_t(T)]} + \sum_{j=1}^{k} \frac{f_j \omega_p^2}{(\omega_j^2 - \omega^2) - i\omega\Gamma_j} \tag{9.1}$$

where the first and second term takes into account the contribution from the conduction electrons. The influence of the temperature (T) is included in the parameters $\Gamma_t(T)$ and $\Omega_p(T)$, which correspond to the total collision frequency and plasma frequency, respectively. The third term describes the interband absorption where k is the number of oscillators with frequency ω_j, strength f_j, and lifetime $1/\Gamma_j$, defined by the damping of each oscillator (Γ_j). The values of these parameters for gold are shown in Table 9.1 and are based in the Lorentz-Drude model [87].

Table 9.1 Values of the Lorentz-Drude Model parameters in electron volts [87].

Strength (f_j)	f_0	f_1	f_2	f_3	f_4	f_5
Au	0.760	0.024	0.010	0.071	0.601	4.384
Damping (Γ_j^{α})	Γ_0	Γ_1	Γ_2	Γ_3	Γ_4	Γ_5
Au	0.0529	0.241	0.345	0.870	2.494	2.214
Frequency (ω_j^{α})	-	ω_1	ω_2	ω_3	ω_4	ω_5
Au	-	0.415	0.830	2.969	4.304	13.32

The plasma frequency at ambient temperature is defined by:

$$\Omega_p = \sqrt{f_0}\,\omega_p = \sqrt{f_0}\sqrt{\frac{m^*}{4\pi N e^2}} \tag{9.2}$$

where N, m^* and e represent the density, the effective mass and the charge of the electrons, respectively, f_0 is the oscillator strength (Table 9.1). The plasma frequency varies with temperature due to volumetric effects according to:

$$\Omega_p(T) = \Omega_p[1 + \gamma_e(T - T_0)]^{-1/2} \tag{9.3}$$

where γ_e = 14.2×10^{-6} per K is the expansion coefficient of the metal (Au) and T_0 = 293.12 K is the room temperature, which is considered as the reference temperature.

The total collision frequency is given by

$$\Gamma_t(T) = \Gamma_0 + \Gamma(T) - \Gamma(T_0) \tag{9.4}$$

where Γ_0 is the damping coefficient (Table 9.1) and $\Gamma(T)$ is the dependence of the collision frequency at the temperature, which depends on two factors: phonon–electron scattering and electron–electron scattering. Their respective contributions are Γ_{cp} and Γ_{ce}.

SPR sensor with wires for simultaneous measurement of refractive index and temperature

The phonon–electron scattering can be modeled by using the Holstein model of phonon-electron scattering [152]:

$$\Gamma_{cp}(T) = \Gamma_0 \left[\frac{2}{5} + 4 \left(\frac{T}{T_D} \right)^5 \int_0^{T_D/T} \frac{z^4 dz}{e^z - 1} \right] \tag{9.5}$$

where T_D = 170 K is the Debye temperature.

The electron–electron scattering frequency is modeled according to the model proposed by Lawrence, based on the Born approximation and on the Thomas–Fermi screening of the Coulomb interaction [152]. The corresponding result can be obtained in terms of the Fermi energy (E_F) of the metal electrons as:

$$\Gamma_{ce}(T) = \frac{1}{6} \pi^4 \frac{\Gamma \Delta}{h E_F} \left[\left(k_B T \right)^2 + \left(\frac{h\omega}{4\pi^2} \right)^2 \right] \tag{9.6}$$

where Γ = 0.55 is a constant, giving the average over the Fermi surface of the scattering probability, Δ = 0.77 is the fractional Umklapp scattering, E_F = 5.53 eV is the Fermi energy, h is Planck's constant and k_B is Boltzmann's constant. Thus equation 3.25 using the thermo-optic coefficient (1.28×10^{-5} K) optical parameter, together with (9.1)– (9.6), completely represents the temperature-dependent dielectric constant of the metal. Apart from its dielectric constant, the thermal expansion of metal film, is also important. It should be noted that for the calculation of thermal expansion of the film one should not use the linear thermal-expansion coefficient ($\alpha = 1.42\times10^{-5}$) of the bulk material. Since the wire may only expand into the normal direction, one has to employ a corrected thermal-expansion coefficient α' for the expansion of the film thickness. The corresponding expression is

$$\alpha' = \alpha \frac{(1+\mu)}{(1-\mu)} \tag{9.7}$$

where μ = 0.44 is the Poisson number of metal. Since μ has a value in the vicinity of 0.3, α' is almost twice the usual thermal-expansion coefficient α, which indicates the importance of this correction [151].

9.3 Plasmonic measurement of refractive index and temperature based on a D-type fiber sensor with gold wires

We consider the design of a refractive index optical sensor composed of a D-type fiber profile with a gold wire mounted on the flat surface, thus replacing the metallic film usually considered in literature [45]. Three extra metal wires are implanted in the fiber cladding (as illustrated in Figure 9.1). The fiber consists in a conventional step index fiber compound by the core with silica doped with 16% germanium (n_{co}) and surrounded by a pure silica cladding (n_{cl}). The top metal wire is partially embedded on the surface of the fiber cladding, to improve mechanical resistance of the device as well as optical coupling to both the core and the external medium, and this is the external wire, with radius r_E. The other three metal wires are placed around the core,

embedded in the cladding to increase the sensitivity to temperature and not exposed to the external medium. These are the internal wires, with the radius of each wire being r_I. In the computer model, the space surrounding the fiber set is filled with the analyte, referred as the external refractive index n_{ext}. The relevant geometrical parameters are: the distance between the center of the fiber and the center of the external wire and the internal wires defined as d and d_I, respectively and the radius of the fiber core r_{co}.

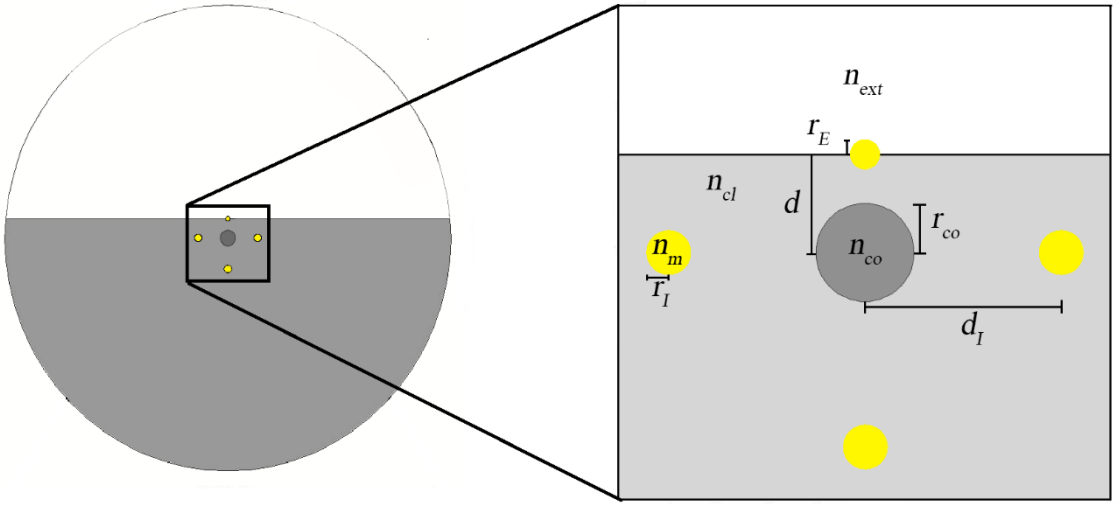

Figure 9.1 Schematic of the proposed SPR D-type fiber.

The metal wire on the surface of the fiber (external wire) is in direct contact with the analyte and therefore supports surface plasmon modes that are primarily sensitive to changes in the external refractive index. On the other hand, the remaining wires (internal wires) support surface plasmon modes that are influenced mainly by changes in temperature, through their dependency on the optical properties of the metal.

The spectral characteristics of the plasmon modes supported on the external metal wire and the associated resonance are determined mainly by the wire radius (r_E) and the boundary conditions imposed by the refractive index of the external medium. A second plasmon resonances is supported by the remaining internal wires, which depends mainly on their radius (r_I), but also on their relative positions and distances to core of the fiber. These three wires support more than one plasmon mode with distinct sensitivities to temperature. One of the plasmon modes is selected accordingly, to optimize the sensor performance. In terms of spectral features observed in the imaginary part of the effective refractive index of the fiber sensor, we are able to obtain two resonance peaks, the first peak is used to measure the external refractive index and the second to measure the temperature.

9.3.1 Study of sensor behavior as function of the external refractive index variation

In this section we study the behavior of the external refractive index sensor in terms of sensitivity and resolution. In this study we have not considered the effect of temperature, hence the results correspond only to the reference temperature. The

sensor parameters used were = 2 μm, r_{co} = 1 μm, the radius of the external gold wire is r_E = 300 nm.

Figure 9.2a shows the real part of the effective refractive index of the modes supported by the wires and the fundamental mode of the fiber in the range between 600 to 1000 nm. In this spectral range there are three modes for the external wire (identified with $\underline{m_E}$ = 0, 1 and 2, depending on the dipole moment of the modes, respectively with null, dipolar and quadripolar modes), which intercept the fundamental mode of the fiber at two points (black squares in Figure 9.2a). Notice that the mode of the external wire with m_E = 0 does not couple with the fundamental mode of the fiber, due to poor phase matching conditions, and it is necessary to work with modes with higher *m*. Also, it is necessary to choose the radius of the internal wires (r_I) such that the corresponding resonances do not overlap with those associated with the modes supported by the external wire. This produces a spectral separation of the different resonances, which facilitates their independent measurement. In particular, we have chosen r_I = 500 nm, that supports two modes in the spectral range between 600 to 1000 nm (identified with m_I = 2 and 3, and corresponding to modes with quadripolar and hexapolar moments, respectively), as shown in Figure 9.2. This solution also intercepts the fundamental mode in two points (blue triangles in Figure 9.2a).

Figure 9.2a also shows the imaginary part of the effective refractive index of the sensor (green dotted curve), which presents four resonances (green circles). At points A and C, they correspond to the resonant coupling between the fundamental mode of the fiber and the modes with m_E = 2 and m_E = 1, and at points B and D they correspond to the resonant coupling between the fundamental mode of the fiber and the modes with m_I = 3 and m_I = 2, respectively. The amplitude of the peaks selected for sensing can be optimized by the distance between the internal wires and the fiber core, therefore controlling the intensity of the coupling between the fundamental mode and each of the internal wire modes. In our case, this optimization resulted in the value d_I = 4 μm. The characteristics of the resonance point D are studied in more detail in the next section. Figure 9.2b and Figure 9.2c show the distribution of light intensity in the fiber for the resonant wavelengths and illustrates the transition in their characteristics.

In all four cases presented, we clearly identify the contribution from the fundamental mode of the fiber, which determines the distribution of light at the center, while the main differences occur near the wires. At wavelengths near resonance A, the external wire supports a quadrupole mode (m_E = 2), while the modes in the internal wires present six intensity modes in the border of the metal, indicating a predominant hexapolar mode (m_I = 3). Near resonance B, the character of the mode near the external wire transits to a strong dipolar moment. Resonances C and D

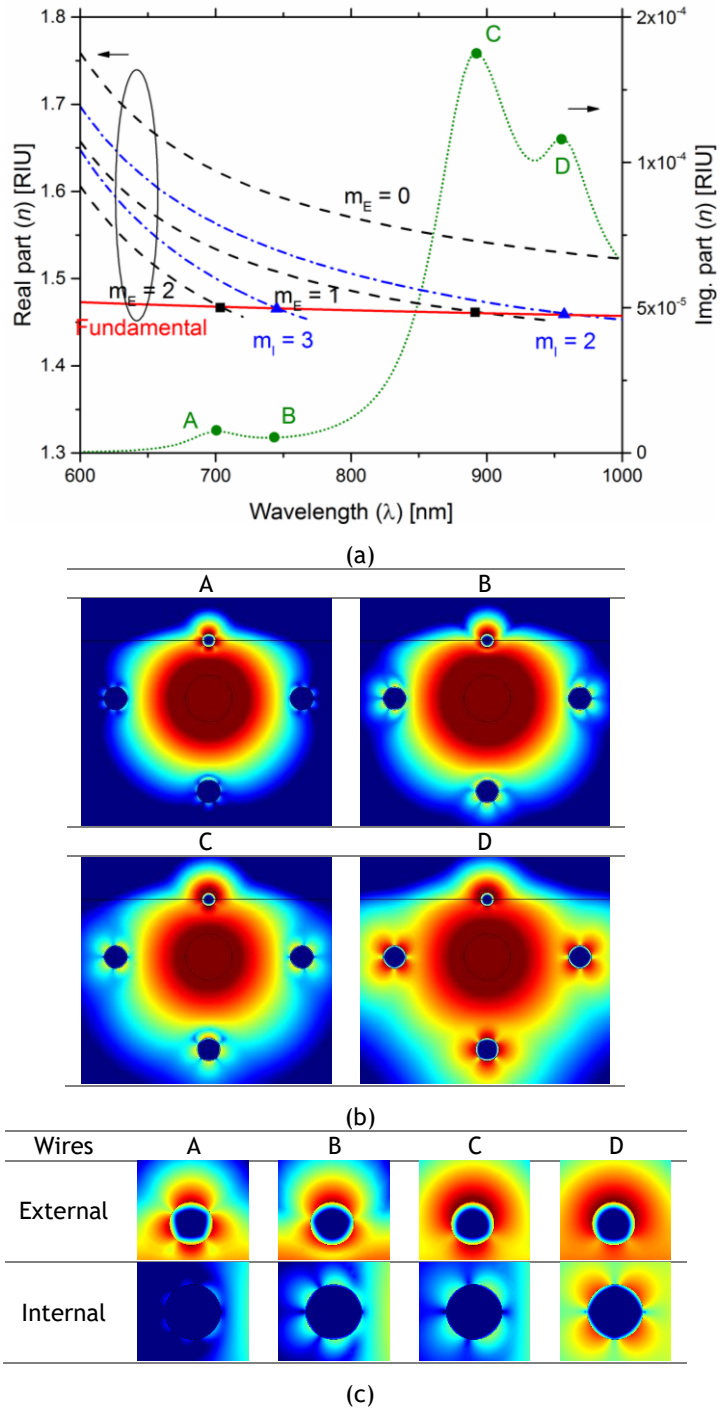

Figure 9.2 (a) Real part (solid line) and imaginary part (dot line) of the refractive index of the sensor as a function of wavelength for external refractive index of 1.38. Also, we represent the dispersion curves of the metal wires for the external modes, m_E (dashed line) and for the internal modes, m_I (dashed-dot line). The crossings between the dispersion curves of the modes in the metal wires and the fundamental mode of the fiber are indicated by square and triangle dots created by the external wire (RI) and the internal wires (*T)*, respectively and these points are represented by the circular green circles in the imaginary part of the effective refractive index of the sensor (green dot line). (b) Distribution of light intensity in the sensor in the referred points. (c) Detail of the distribution of light intensity near the external and the left internal wire in Figure 9.2b.

correspond to an intensity distribution with strong dipolar moment near the external wire and strong quadripolar moment near the internal wires. There is however a

significant difference in the light distribution of these resonances: while for resonance C the electric field between the internal wires and the core changes sign, for resonance D the sign is preserved. This is similar to the even and odd plasmon modes produced by the coupling of surface plasmons located at opposite surfaces of a thin metal film [153]. The practical difference between these two resonances is that while resonance C is very sensitive to changes in the refractive index, resonance D is mainly sensitive to temperature.

Figure 9.3 shows the attenuation as a function of wavelength for different values of external refractive index, with a constant temperature, calculated according to (equation 3.36). The sensitivity (*S*) and the resolution (*R*) of the sensor are expressed in Table 9.2 and were obtained assuming that it is possible to detect experimentally a spectral variation of 0.1 nm, using the data in Figure 9.3 and equations 3.71 and 3.72.

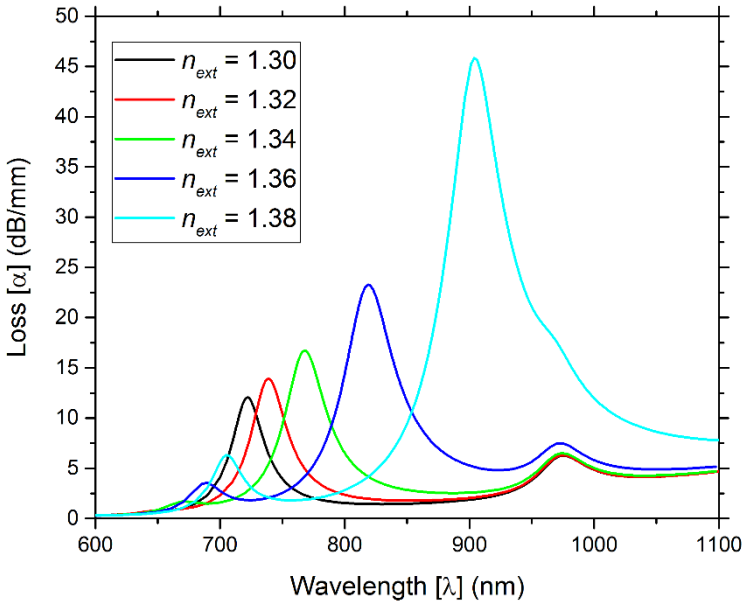

Figure 9.3 Attenuation as function of wavelength for different values of external refractive index with four metallic wires, for d = 2 µm. The range of external refractive index is from 1.30 to 1.38. In the curve for n_{ext}=1.38, the two peaks with higher wavelengths are partially overlapped, which makes at extremely difficult to measure the central wavelength for the weaker peak, and therefore limits the range of operation of the sensor.

The sensitivity and resolution show a good sensor performance when compared with other fiber sensors based on SPR in metal wires. For instance, Luan [142] presented a refractive index sensor where a silver wire is placed on top of the fiber, achieving a sensitivity of 2700 nm/RIU in the wavelength range from 698 to 728 nm for n_{ext} = 1.33 to 1.34. Although such a sensitivity value is slightly better than in our sensor, it results from the wire being completely exposed, which has the drawback of reducing the robustness of the sensor. Lu [121] presented another refractive index sensor based on a grapefruit photonic crystal fiber where the holes are filled with silver wires with a radius of 300 nm, reaching a sensitivity of 2400 nm/RIU for a variation of the external refractive index between 1.33 and 1.335 RIU, for a wavelength of 635-650 nm, respectively.

Table 9.2 Sensitivity, resolution and range of the wavelength values for the refractive index optical fiber sensor.

	Sensitivity (nm/RIU)	Resolution (RIU)	Range λ (nm)
Range of n_{ext}	External wire r_m = 300 nm		
[1.30,1.32]	687.5	1.45×10^{-5}	720-740
[1.32,1.34]	1375	7.27×10^{-6}	740-770
[1.34, 1.36]	2437.5	4.10×10^{-6}	770-820
[1.36,1.38]	4062.5	2.46×10^{-6}	820-900

When comparing the results of this chapter (Table 9.2) with those obtained in Chapter 7, we notice that they are not as good in terms of refractive index sensitivity, because some of the design parameters are different. Indeed, in this chapter the main concern has been with the development of multiparameter measurement using the plasmonic modes, rather then optimizing the sensing performance to a single parameter (such as the refractive index). As a result, it was necessary to find a compromise between performance and parameter independence, and our choice was to sacrifice part of the former in benefit of the later.

9.3.2 Optimization of the sensor

Figure 9.3 shows the attenuation of the guided mode per unit of length as a function of wavelength for different values of external refractive index, which presents three main peaks. The first, for low wavelengths is very weak and has little use for sensing (λ_{P1}). The second peak is the most intense and shifts towards longer wavelengths with increasing external refractive index (λ_{P2}), whereas the third at a higher wavelength remains unchanged (λ_{P3}). This peak however is much weaker than the second, a problem which can be overcome either by changing the number of internal wires, or by decreasing the distance between the core and internal wires. Another possibility is to lower the intensity of the second peak by changing the distance of the core to the external wire.

Increasing the number of internal wires can increase this loss peak. However, structures with a larger number of wires can be more difficult the fabricate so, we propose a second approach to increase the third peak, by reducing the distance between the metal and the internal wires. Figure 9.4a shows the results for the attenuation if the distance between internal wires and the core is reduced to 1 μm. The reduction of this distance alters the coupling strength between the modes and, in turn, not only shifts the central wavelength of the peaks but also changes their relative amplitudes. However, the dependent character of the second peak (and independent character of the third) on the external refractive index is preserved. The analysis also shows that the range of measurement of RI of this sensor configuration is between 1.30 and 1.38, and is mainly determined by the geometry and dimensions of the components

(specially the metal wires). For higher values of RI, the second and third peaks overlap and it is hard to separate them in the spectrum. This problem can be resolved by increasing the radius of the internal wires. Figure 9.4b shows the attenuation as function of the wavelength when the radius of the internal wires is 550 nm. This new radius changes only the third peak of resonance, from 975 nm to 1025 nm, when compared with Figure 9.3. The first and second peaks maintain the same loss magnitude and wavelength resonance.

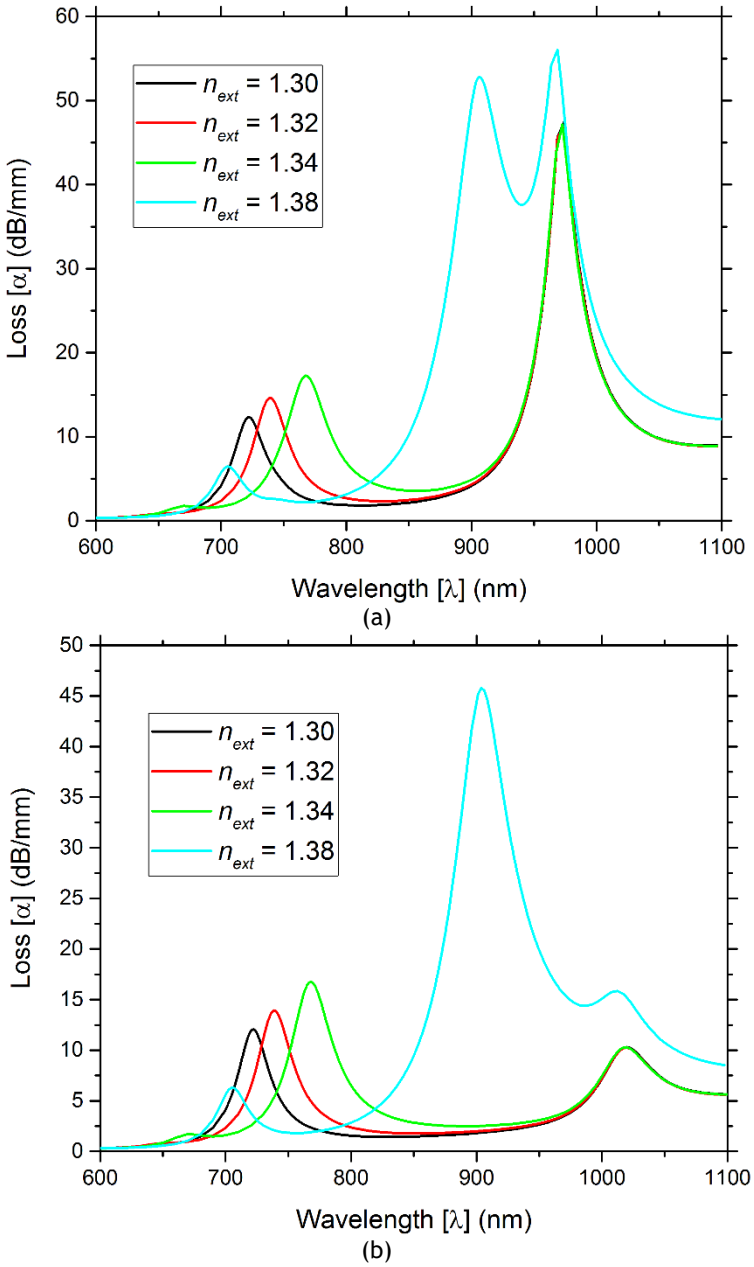

Figure 9.4 Attenuation as a function of wavelength for different values of external refractive index D-type for d = 2 μm, (a) d_l = 3 μm (the distance between the internal wires and the core) and r_l = 500 nm (radius of the internal wires) and for (b) d_l = 4 μm and r_l = 550 nm. The external refractive index varies from 1.30 to 1.38.

Using different parameters, like the number of wires, the radius of the internal and external wires and the different distance between the core and the internal and external wires, it is possible to optimize the sensor. Our proposal for the sensing configuration considers four wires (one external and three internal) localized

symmetrically around the core, whose results are presented in Figure 9.2, Figure 9.3 and Figure 9.4 and with chosen configuration are the d = 2.5 μm, d_I = 4 μm, r_E = 300 nm (the radius of the external wire) and r_I = 500 nm (the radius of the internal wires). With this configuration and parameters, the sensor displays two main peaks with similar amplitude, as well as, a fair peak separation, within a range of detection between 1.30 and 1.34 (but not for 1.38).

9.3.3 Study of the sensor behavior as a function of temperature

In this section we present the behavior of the third peak as a function of temperature. Also, we consider the ambient temperature and the effects of the temperature in the properties of the materials, to be modeled according to equation 9.1.

Figure 9.5 shows the attenuation as a function of wavelength for different values of temperature. The peak on the left corresponds to the second peak (λ_{P2}) observed in the previous figures, while the peak on the right corresponds to the third peak (λ_{P3}). The central wavelength of the peak on the left (which is strongly dependent on the external RI) practically does not change with the temperature. Instead, the peak on the right (which is almost independent on the external RI) exhibits a shift toward longer wavelengths for higher temperatures.

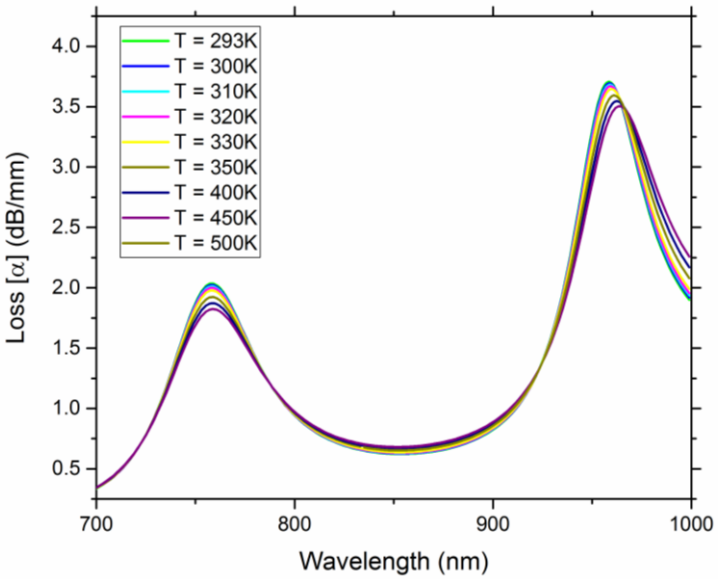

Figure 9.5 Attenuation as a function of wavelength for different values of temperature sensor D-type. The external refractive index is 1.34 RIU. The configuration is d = 2.5 μm, d_I = 4 μm, r_E = 300 nm (the radius of the external wire) and r_I = 500 nm (the radius of the internal wires).

The sensitivity of the temperature sensor is calculated according to:

$$S(\lambda) = \frac{\Delta\lambda_{peak}}{\Delta T} \tag{9.8}$$

where ΔT is the variation in temperature, and, using the data from Figure 9.5, we obtain a sensitivity to changes in temperature of 3 pm/K for the peak on the left and the 30 pm/K for the peak on the right. Although the sensitivity to changes in

temperature of the latter peak is smaller than other temperature sensors based in SPR found in the literature, it should be noted that in those cases the measurement of temperature is assisted by other sensing principles (including thermal expansion of interferometric components), whereas in our case the process is purely plasmonic. Luan [107] used a microstructured optical fiber with a thin layer of silver deposited on the internal surface of one hole, which is then filled with a large thermo-optic coefficient liquid as a sensing medium. This configuration obtained a temperature sensor with high sensitivity of 6.18 nm/K for wavelengths from 838 to 943 nm and with a variation of the temperature from 26 ºC to 43 ºC (which represents a variation of the refractive index of the thermo-optic coefficient liquid from 1.41 to 1.42). Sensors without this type of components have less sensitivity (up to 70 pm/K) [154]. Our configuration is very versatile in the sense that changing geometrical parameters (such as the wire radius or the distance between the wires and the core), the number of wires, among others, it is possible to customize the operation at parameters of the sensor, including the range of measurement of the refractive index or the reference wavelength of the sensor. This characteristic surpasses the limitations of other proposals that are dependent on the specific properties of a test fluid [28], [107].

Table 9.3, summarizes the sensitivity coefficients of the two peaks, for refractive index (K_n) and temperature (K_T), taken from the information presented in Figure 9.3 and Figure 9.5.

Table 9.3 Sensitivity coefficients of the two peaks for refractive index and temperature.

	K_n	K_T
$\Delta\lambda_{P2}$	2093.1nm/RIU	3.4pm/K
$\Delta\lambda_{P3}$	0	27.3pm/K

The dual response of the two sensing peaks as a function of the variation of the wavelength sensor in terms of RI and temperature, allows writing a conditioned system of two equations for Δn and ΔT, given in matrix form as:

$$\begin{bmatrix} \Delta n \\ \Delta T \end{bmatrix} = \frac{1}{K_{\lambda_{P3},T} K_{\lambda_{P2},n}} \begin{bmatrix} K_{\lambda_{P2},n} & K_{\lambda_{P3},n} \\ K_{\lambda_{P2},T} & K_{\lambda_{P3},T} \end{bmatrix} \begin{bmatrix} \Delta\lambda_{P2} \\ \Delta\lambda_{P3} \end{bmatrix} \tag{9.9}$$

where $K_{\lambda_{P2},n}$, $K_{\lambda_{P2},T}$ and $K_{\lambda_{P3},T}$, the matrix elements, are the sensitivity coefficients of the two peaks as a function of the refractive index and temperature, respectively, and represented in Table 9.3.

$$\begin{bmatrix} \Delta n \\ \Delta T \end{bmatrix} = \frac{1}{57.14} \begin{bmatrix} 2093.1 & 0 \\ 3.4 & 27.3 \end{bmatrix} \begin{bmatrix} \Delta\lambda_{P2} \\ \Delta\lambda_{P3} \end{bmatrix} \tag{9.10}$$

This callibration matrix allows us to determine the temperature and refractive index unequivocally, by processing the signals retrieved from the two peaks.

The values of the elements of the calibration matrix presented in Table 9.3 show that it is strongly diagonaly dominant, and therefore a well conditioned matrix, which will introduce low numerical errors when used to obtain the values of the RI and temperature from the data obtained experimentally. This comes from the dependence

of each peak to a specific sensing parameter (RI or temperature) thus reducing the crosstalk between them.

9.4 Conclusion

These results pave the way for a new type of optical sensors that measure simultaneously different parameters, including temperature and refractive index, via plasmonic response, which explores both new geometries and other materials that can further improve sensing performances.

We have demonstrated a sensor based in a D-type fiber using SPR with multiple wires that allows the simultaneous measurement of temperature and refractive index, by direct manipulation of the properties of the surface plasmon resonances supported by the wires. In particular, this sensor presents two main measurement peaks, each one resulting from a particular plasmon resonance, and mainly dependent on just one of the two parameters measured, which facilitates the sensor calibration and promotes more accurate measurements. Indeed, in our sensor proposal we verified that one peak is very sensitive to the RI (4000 nm/RIU) and slightly responsive to temperature (3 pm/K), whereas the other peak is only sensitive to temperature, specifically with a sensitivity of 30 pm/K and no response to changes to the refractive index. Also, this sensor proposal presents good performance parameters, including intensity of loss, range of operation and spectral localization of the resonance peaks.

The optimization of the sensor parameters can be done with the variation of the radius of the gold wires, number of the internal wires, distance between wires in the core and distance between the external wire and the core, among other parameters.

We have also shown the possibility of manipulating the supermodes in the wires to obtain a refractive index range detection between 1.30 to 1.38, with a clear distinction of the two measurement peaks, while maintaining the same sensitivity to both parameters (refractive index and temperature). Moreover, we also demonstrated that changing the same geometric parameters also allows to customize the sensor to measure in other ranges or to operate with other specifications, like the magnitude and range of wavelength variation of the loss peaks, among others.

Unlike other proposals in literature that rely on the changes in refractive index produced by variations of temperature in reference materials [107] or that use the change of dimensions produced by the thermal expansion of interferometric components [155], our sensor design relies on the changes produced on the modal characteristics of the plasmons resulting from changes in the population of free electrons, associated with the variation of the temperature. This approach allows us to use the direct dependence of the plasmon resonances on temperature to measure this parameter. On the other hand, the combination of wires with distinct natures (specifically, external wires in contact with the exterior medium, and internal wires that are shielded from the changes in the external refractive index), that support plasmons resonances in distinct spectral regions, allows us to combine the measurement of multiple parameters. To our knowledge, this has not yet been described in literature and could, in principle, be extended to even more parameters.

SPR sensor with wires for simultaneous measurement of refractive index and temperature

In short, we presented a sensor configuration capable of simultaneous measurements the temperature and refractive index of the analyte medium, using plasmon resonances that present strong dependency to just one of the measurements and thus separate their measure. This work also has the aims to stimulate research into the development of novel multiple parameters sensors, that use the direct manipulation of the plasmon resonances as sensing principle.

Chapter 10 Conclusions and outlook

Today's optical sensors have moved away from the simplicity of the early days, into higher degrees of sophistication and increasing performance. In particular, fiber optical sensors relay on newer sensing principles, such as plasmonics, and integrate many components at a nanoscale, from metal and dielectric structures. With the development of newer artificial materials, such as metamaterials, this complexity will increase even further, resulting in newer and innovative sensing designs, many of which are still not feasible, using existing fabrication techniques, or are extremely expensive and hard to produce, which implies that an exhaustive experimental test of these designs is neither efficient nor wise in terms of resource management. In this thesis we have used simulation tools to overcome these for optimize exiting sensing designs and even to test novel sensing concepts. In particular, we showed how to combine optical fiber technologies with metallic films and wires into optical fiber sensors, allowing a synergy between the light transported in the silica fibers and plasmon excitations supported by the metal structures, to measure the properties of some external medium, typically the refractive index but also the temperature.

Many of these new ideas arise from the possibility to control the structure of the fiber at a nanoscale, introducing for example nanowires or metamaterials, composed of a mixture of metal and dielectrics, at scales inferior to both the wavelength of light and the typical dimensions of optical fibers and their core. Although this challenge is being solved by the constant improvements of fabrication techniques, it is not a lesser challenge from the point of view of simulation, as it requires to model systems with distinct materials casted into many components, with dimensions that can vary over one or even two orders of magnitude. Moreover, at very small scales, the behavior of light and the optical properties of matter can be quite different from those experienced at the human and everyday scale. For example, surface plasmons become strongly localized. The idea is precisely to use these micro and nanoscale behaviors to improve sensing.

Let us go back to the questions raised in the introduction:

- Is this simulation approach effective in modelling different SPR D-Type fiber configurations?
- How do the results of the simulations compare with the experimental data?
- How can we engineer the interactions between light and plasmons to improve sensing performance?
- What kind of microstructures and new materials can be incorporated in the sensors to help boost sensing performance?

- Can we integrate the characteristics of different SPR sensors measuring distinct quantities in a single sensor?

Throughout this thesis we hope to have shown that:

- This simulation approach can be used to model different SPR D-type sensors, by studying different types of fibers, materials, structures, modes, among others.
- Simulations provide an easy and quick way of exploring the physical principles in optical sensing and optimize them, while providing results which are in good agreement with experimental data, as shown in **Erro! A origem da referência não foi encontrada.**.
- Changing the modes in the fiber and in the metallic wires improves characteristics of the sensor like sensitivity, resolution, operational wavelength and loss.
- The SPR sensor based in conventional PCF D-type fiber presented slightly better sensitivity when compared with the conventional D-type fiber, but it is possible to increase the performance of the PCF D-type fiber sensor by changing the inner structure, as proposed in **Erro! A origem da referência não foi encontrada.**. Also, when we use a new material, like metamaterial permitted a SPR sensor with a specific intensity of the loss and operation range of wavelength, that caused a variation in the sensitivity and resolution, but better than the conventional SPR D-type with gold.
- A complete understanding and control of the physical properties of the plasmons allow us to extend the current concept of SPR sensors, which today are basically extremely sensitive refractive index sensors, into genuine multiparameter SPR sensors, that can use SPR to measure directly both refractive index and temperature, and perhaps in the near future even more parameters.

10.1 Sensors with thin materials films

In **Erro! A origem da referência não foi encontrada.** we showed that the COMSOL Multiphysics can be used to test and optimize, computationally, a sensing configuration with high accuracy and considerable economy of time and resources.

It was also possible to demonstrate the benefits of using COMSOL to improve the performance of refractive index SPR D-type optical fiber sensors. The optimization of the sensors can be performed through the variation of the metal thickness, the distance of the metal to the center of the fiber and by the use of a high refractive index layer. We concluded the metal thickness changes all the characteristics of the sensors studied in this thesis, such as sensitivity, resolution, operation wavelength and also loss intensity, and the optimal relation of loss and sensitivity is when the thickness of the metal is between 45 nm and 65 nm. The distance *d* only changes the loss intensity. Finally, the high refractive index overlayer alters the sensor operation wavelength, smaller thicknesses of the overlayer (20 nm to 30 nm) is the recommended choice to allow light to reach the external medium. We also studied different positions

for the air holes in the fibers and we verified that the corresponding variation in the sensor characteristics, which allowed us to optimize the singlemode SPR sensor.

A few SPR sensor configurations have been tested, showing that the conventional SPR D-type sensor can be optimized in sensitivity, resolution, intensity of loss, operation wavelength. Comparing the conventional SPR D-type sensor with the PCF D-type sensor, we have:

- The SPR PCF D-type sensor was implemented with an increase in the sensitivity of 600 nm/RIU, in the range of the n_{ext} = [1.36,1.37] RIU, a redshift of 75 nm of the peak of resonance, but with a decrease in the intensity of loss.
- By removing holes in the SPR PCF D-type sensor we optimized the former results and increased the sensitivity of the sensor by 1800 nm/RIU, in the range of the n_{ext} = [1.36,1.38] RIU, with a high intensity of the loss and with a redshift of the 150 nm of the peak of resonance.
- The use of a high refractive index overlayer allows us to shift the operation wavelength to 900 nm and the sensitivity of the sensor to 6783 nm/RIU in the range of n_{ext} = [1.367,1.390] RIU.

The SPR conventional D-type sensor with a overlayer presents a good sensitivity for low values of n_{ext}, but for high values of n_{ext} the proposes SPR PCF D-type sensor present a sensitivity highest of the 8000 nm/RIU in the range of n_{ext} = [1.38,1.39] RIU. That means different configurations, with different parameters, present different SPR sensor characteristics, which can be quickly determined by using COMSOL Multiphysics for SPR sensor optimization.

In **Erro! A origem da referência não foi encontrada.**, we showed the numerical and experimental behavior of the SPR POF D-type sensor and compared the respective results. In particular, the sensitivity of the POF D-type sensor is similar to the conventional D-type sensor presented in the previous chapter. The numerical simulation show multiple modes are found and can be coupled with the plasmonic mode. The multiple modes have different intensities of loss and we concluded that the higher order modes presented a bigger loss since they have a bigger interaction with the external medium than the lower order modes. This effect can be verified in the experimental study, when we used a filter before or after the sensor head.

The numerical and experimental results were similar. The differences is on the utilization or not of the photoresist, the number or modes used in the study, among others.

In **Erro! A origem da referência não foi encontrada.** we showed a SPR D-type sensor with a thin metamaterial and this sensor presents an improvement to the conventional SPR D-type sensor with a thin gold film. We also presented a method to optimize the sensor, dependent on the concentration of Al_2O_3 and Ag and on the thickness of the metamaterial.

10.2 Sensors with wires

Chapter 7 and **Erro! A origem da referência não foi encontrada.** showed the metallic wires can be used for SPR sensors. The principal characteristics of the wires are the generation of multiple plasmonic modes. These plasmonic modes generate SPR

in different wavelengths, which allow the possibility of wavelength multiplexing for measuring different physical parameters. The SPR D-type sensor has the external wire localized between the cladding and the external medium, for the optimal compromise between detection and robustness.

In Chapter 7 a singlemode SPR D-type wire sensor was studied. This sensor presented an increase in the sensitivity of 2200 nm/RIU in the range of n_{ext} = [1.36,1.38] RIU, a redshift of 250 nm of the peak of resonance (from 625 nm to 825 nm) and an increase of the loss intensity when compared with the conventional SPR D-type fiber. This sensor can be improved by using different plasmonic modes that present a different sensitivity.

In **Erro! A origem da referência não foi encontrada.** a multimode SPR D-type wire sensor was studied. In this case the plasmonic modes can be combined with different multimode presented in the fiber to produce SPR at different wavelengths with different characteristics. Therefore, the sensitivity of the sensor also depends on the studied mode. In the range of n_{ext} = [1.36,1.38] RIU we had:

- The fundamental mode has a sensitivity of 3110 nm/RIU and an operation range from 780-850 nm.
- The mode $M_{p3,5}$ presented a sensitivity of 5340 nm/RIU and an operation range from 840-945 nm.

The $M_{p3,5}$ mode presented a performance comparable with the SPR D-type fiber sensor, with a overlayer and the SPR PCF D-type sensor. Again, appropriate filtering is necessary to select a mode or a set of specific modes to create the optimized sensors.

10.3 Simultaneous measurement of refractive index and temperature

Finally, **Erro! A origem da referência não foi encontrada.** we showed a SPR D-type sensor with multiple wires that combined the knowledge of the previous chapters to make a sensor that measure simultaneously refractive index and temperature. Indeed, in our sensor proposal, we verified that one peak is very sensitive to the RI (4000 nm/RIU) and slightly responsive to temperature (3 pm/K), whereas the other peak is only sensitive to temperature (30 pm/K), and practically no response to changes to the refractive index. This configuration also permitted individual control of the localization of the SPR wavelengths of the refractive index and temperature to improve of the sensor control.

10.4 Outlook

In this thesis we have started from one of the current paradigms of optical fiber sensors, namely those based on SPR, and asked the fundamental question: how can we improve their performance, using changes in the more custom designs that can be implemented, using fabrication techniques already existing or foreseeable in the near future. The idea was to adopt an engineering approach and to rethink the existing technology and understand how it can be improved. Using numerical simulations, we have systematically examined the different aspects that influence sensor performance, from the nature of the optical and plasmonic modes supported in these

sensors, to the influence of the optical properties of materials, and the geometry of the sensor components. We have inclusively looked into metamaterials as a way to develop artificial materials with customized properties that can overcome the limitations offered by natural ones. This approach has allowed to push further the performance of fundamental design of SPR based optical fiber sensors and even propose new concepts, such as the multiparameter SPR sensor. It is clear that the idea of multiparameter SPR sensing must be further developed. Temperature is an important parameter to be added to the measurement of refractive index, since it is determinant to the calibration of the sensor itself. However, other parameters could in principle also be considered. Also, it is clear that coupling plasmons in different metal structures can result in a collective response that is much more complex and perhaps interesting for sensing than single plasmon modes. There is clearly still more to be explored, since this thesis has only started to graze the surface of this topic and initial results are promising.

However, after almost four years and as we finish this thesis it is clear that the limits of SPR sensing technology can be pushed even further. Indeed, if fabrication techniques allow to reduce the size of the metallic nanowires even further not only we can make the localized surface plasmons more sensitive to parameters such as the refractive index and temperature, but also to other parameters such as external electromagnetic fields. Furthermore, in metal structures with sizes of a few nanometers the plasmon modes start to gain a quantum and nonlinear character and the models used to describe them must be reviewed. This paves the way for new concepts in sensing and a challenge to develop adequate numerical models.

Bibliography

[1] B. Lee, S. Roh, and J. Park, "Current status of micro- and nano-structured optical fiber sensors," *Opt. Fiber Technol.*, vol. 15, no. 3, pp. 209–221, Jun. 2009.

[2] S. Roh, T. Chung, and B. Lee, "Overview of the Characteristics of Micro- and Nano-Structured Surface Plasmon Resonance Sensors," *Sensors*, vol. 11, no. 12, pp. 1565–1588, Jan. 2011.

[3] B. Liedberg, C. Nylander, and I. Lunstrom, "Surface plasmon resonance for gas detection and biosensing," *Sensors and Actuators*, vol. 4, pp. 299–304, 1983.

[4] B. Liedberg, C. Nylander, and I. Lundström, "Biosensing with surface plasmon resonance — how it all started," *Biosens. Bioelectron.*, vol. 10, no. 8, pp. i–ix, Jan. 1995.

[5] R. C. Jorgenson and S. Yee, "A fiber optic chemical sensor based on surface plasmon resonance," *Sensors Actuators B Chem.*, vol. 12, no. 3, pp. 213–220, 1993.

[6] R. Slavík, J. Homola, and E. Brynda, "A miniature fiber optic surface plasmon resonance sensor for fast detection of staphylococcal enterotoxin B," *Biosens. Bioelectron.*, vol. 17, no. 6–7, pp. 591–595, Jun. 2002.

[7] J. Čtyroký, J. Homola, and M. Skalský, "Modelling of surface plasmon resonance waveguide sensor by complex mode expansion and propagation method," *Opt. Quantum Electron.*, vol. 29, no. 2, pp. 301–311, 1997.

[8] B. Lee, S. Roh, H. Kim, and J. Jung, "Waveguide-based surface plasmon resonance sensor design," in *Photonic Fiber and Crystal Devices: Advances in Materials and Innovations in Device Applications III*, 2009, vol. 7420, p. 74200C.

[9] M. a Kaliteevski, V. V Nikolaev, and R. a Abram, "Calculation of the Mode Structure of Multilayer Optical Fibers Based on Transfer Matrices for Cylindrical Waves," *Opt. Spectrosc.*, vol. 88, no. 5, pp. 792–795, 2000.

[10] X. D. Hoa, M. Tabrizian, and A. G. Kirk, "Rigorous Coupled-Wave Analysis of Surface Plasmon Enhancement from Patterned Immobilization on Nanogratings," *J. Sensors*, vol. 2009, pp. 1–7, 2009.

[11] Y. Al-Qazwini, P. T. Arasu, and A. S. M. Noor, "Numerical investigation of the performance of an SPR-based optical fiber sensor in an aqueous environment using finite-difference time domain," in *2011 2nd International Conference on Photonics*, 2011, vol. 13, no. 7, pp. 1–4.

[12] M. Hautakorpi, M. Mattinen, and H. Ludvigsen, "Surface-plasmon-resonance sensor based on suspended-core microstructured optical fiber," in *OECC/ACOFT 2008 - Joint Conference of the Opto-Electronics and Communications Conference and the Australian Conference on Optical Fibre Technology*, 2008, vol. 16, no. 12, pp. 1–2.

[13] J. Homola, "Surface Plasmon Resonance Sensors for Detection of Chemical and Biological Species," *Chem. Rev.*, vol. 108, no. 2, pp. 462–493, Feb. 2008.

[14] A. Otto, "Excitation of nonradiative surface plasma waves in silver by methode of frustrated total reflection," *Z. Phys.*, vol. 216, no. 4, pp. 398–410, 1968.

[15] E. Kretschmann and H. Raether, "Radiative Decay of Non Radiative Surface Plasmons Excited by Light," *Zeitschrift für Naturforsch. A*, vol. 23, no. 12, pp. 2135–2136, Jan. 1968.

[16] J. R. Sambles, G. W. Bradbery, and F. Yang, "Optical excitation of surface plasmons: An introduction," *Contemp. Phys.*, vol. 32, no. 3, pp. 173–183, May 1991.

[17] F. Villuendas and J. Pelayo, “Optical Fibre Device for Chemical Sensing Based on Surface Plasmon Excitation,” *Sensors Actuators A Phys.*, vol. 423, no. 1–3, pp. 1142–1145, 1990.

[18] M. Piliarik and J. Homola, “SPR Sensor Instrumentation,” in *Surface Plasmon Resonance Based Sensors*, Springer S., vol. 4, 2006, pp. 95–116.

[19] M. Piliarik and J. Homola, “Surface plasmon resonance (SPR) sensors: approaching their limits?,” *Opt. Express*, vol. 17, no. 19, pp. 16505–16517, Sep. 2009.

[20] D. F. Santos, A. Guerreiro, and J. M. Baptista, “SPR Microstructured D-Type Optical Fiber Sensor Configuration for Refractive Index Measurement,” *IEEE Sens. J.*, vol. 15, no. 10, pp. 5472–5477, Oct. 2015.

[21] J. Homola, I. Koudela, and S. S. Yee, “Surface plasmon resonance sensors based on diffraction gratings and prism couplers: sensitivity comparison,” *Sensors Actuators B Chem.*, vol. 54, no. 1–2, pp. 16–24, Jan. 1999.

[22] L. De Maria, M. Martinelli, and G. Vegetti, “Fiber-optic sensor based on surface plasmon interrogation,” *Sensors Actuators B Chem.*, vol. 12, no. 3, pp. 221–223, Apr. 1993.

[23] E. Klantsataya, P. Jia, H. Ebendorff-Heidepriem, T. Monro, and A. François, “Plasmonic Fiber Optic Refractometric Sensors: From Conventional Architectures to Recent Design Trends,” *Sensors*, vol. 17, no. 1, p. 12, Dec. 2016.

[24] H. Chen, S. Li, G. An, J. Li, Z. Fan, and Y. Han, “Polarization Splitter Based on d-Shaped Dual-Core Photonic Crystal Fibers with Gold Film,” *Plasmonics*, vol. 10, no. 1, pp. 57–61, Feb. 2015.

[25] Z. Tan, X. Hao, Y. Shao, Y. Chen, X. Li, and P. Fan, “Phase modulation and structural effects in a D-shaped all-solid photonic crystal fiber surface plasmon resonance sensor,” *Opt. Express*, vol. 22, no. 12, p. 15049, Jun. 2014.

[26] M. Tian, P. Lu, L. Chen, C. Lv, and D. Liu, “All-solid D-shaped photonic fiber sensor based on surface plasmon resonance,” *Opt. Commun.*, vol. 285, no. 6, pp. 1550–1554, Mar. 2012.

[27] E. K., T. Gorman, H. Ademgil, S. Haxha, G. Robinson, and J. Oliver, “A Novel Compact Photonic Crystal Fibre Surface Plasmon Resonance Biosensor for an Aqueous Environment,” in *Photonic Crystals - Innovative Systems, Lasers and Waveguides*, InTech, 2012.

[28] N. Luan, R. Wang, W. Lv, Y. Lu, and J. Yao, “Surface Plasmon Resonance Temperature Sensor Based on Photonic Crystal Fibers Randomly Filled with Silver Nanowires,” *Sensors*, vol. 14, no. 9, pp. 16035–16045, Aug. 2014.

[29] M. Skorobogatiy, “Microstructured and Photonic Bandgap Fibers for Applications in the Resonant Bio- and Chemical Sensors,” *J. Sensors*, vol. 2009, pp. 1–20, 2009.

[30] K. Matsubara, S. Kawata, and S. Minami, “Multilayer system for a high-precision surface plasmon resonance sensor,” *Opt. Lett.*, vol. 15, no. 1, p. 75, Jan. 1990.

[31] J. S. Yuk and K. Ha, “Analysis of Immunoreactions on Protein Arrays by Using Wavelength-Interrogation-Based Surface Plasmon Resonance Sensors,” *Korean Phys. Soc.*, vol. 45, no. 4, pp. 1104–1108, 2004.

[32] L.-M. Zhang and D. Uttamchandani, “Optical chemical sensing employing surface plasmon resonance,” *Electron. Lett.*, vol. 24, no. 23, p. 1469, 1988.

[33] R. Verma and B. D. Gupta, “A novel approach for simultaneous sensing of urea and glucose by SPR based optical fiber multianalyte sensor,” *Analyst*, vol. 139, no. 6, p. 1449, 2014.

[34] R. K. Verma and B. D. Gupta, “Theoretical modelling of a bi-dimensional U-shaped surface plasmon resonance based fibre optic sensor for sensitivity enhancement,” *J. Phys. D. Appl. Phys.*, vol. 41, no. 9, p. 95106, May 2008.

[35] N. Cennamo, D. Massarotti, R. Galatus, L. Conte, and L. Zeni, “Performance Comparison of Two Sensors Based on Surface Plasmon Resonance in a Plastic Optical Fiber,” *Sensors*, vol. 13, no. 1, pp. 721–735, Jan. 2013.

[36] C. Nylander, B. Liedberg, and T. Lind, “Gas detection by means of surface plasmon resonance,” *Sensors and Actuators*, vol. 3, pp. 79–88, 1982.

[37] J. M. Brockman, B. P. Nelson, and R. M. Corn, “Surface plasmon resonance imaging measurements of ultrathin organic films.,” *Annu. Rev. Phys. Chem.*, vol. 51, no. 1, pp. 41–63, Oct. 2000.

[38] B. Sun, X. Wang, and Z. Huang, “Study on intensity-modulated surface plasmon resonance array sensor based on polarization control,” in *2010 3rd International*

Conference on Biomedical Engineering and Informatics, 2010, no. Bmei, pp. 1599–1602.

[39] H. Moayyed, I. T. Leite, L. Coelho, J. L. Santos, A. Guerreiro, and D. Viegas, "Analysis of phase interrogation of SPR fiber optic sensors with characteristics tailored by the application of different metal-dielectric overlays," in *23rd International Conference on Optical Fibre Sensors*, 2014, vol. 9157, p. 91575E.

[40] A. A. Kruchinin and Y. G. Vlasov, "Surface plasmon resonance monitoring by means of polarization state measurement in reflected light as the basis of a DNA-probe biosensor," *Sensors Actuators B Chem.*, vol. 30, no. 1, pp. 77–80, Jan. 1996.

[41] X. Chen, "SPR sensor by method of electro-optic phase modulation and polarization interferometry," *Chinese Opt. Lett.*, vol. 10, p. S12401, 2012.

[42] W. J. H. Bender, R. E. Dessy, M. S. Miller, and R. O. Claus, "Feasibility of a Chemical Microsensor Based on Surface Plasmon Resonance on Fiber Optics Modified by Multilayer Vapor Deposition," *Anal. Chem.*, vol. 66, no. 7, pp. 963–970, 1994.

[43] J. Homola and R. Slavik, "Fibre-optic sensor based on surface plasmon resonance," *Electron. Lett.*, vol. 32, no. 5, p. 480, 1996.

[44] O. Frazão, J. M. T. Baptista, and J. L. Santos, "Recent Advances in High-Birefringence Fiber Loop Mirror Sensors," *Sensors*, vol. 7, pp. 2970–2983, 2007.

[45] D. F. Santos, A. Guerreiro, and J. M. Baptista, "Numerical investigation of a refractive index SPR D-type optical fiber sensor using COMSOL multiphysics," *Photonic Sensors*, vol. 3, no. 1, pp. 61–66, Aug. 2013.

[46] M.-H. Chiu, C.-H. Shih, and M.-H. Chi, "Optimum sensitivity of single-mode D-type optical fiber sensor in the intensity measurement," *Sensors Actuators B Chem.*, vol. 123, no. 2, pp. 1120–1124, May 2007.

[47] S.-F. Wang, M.-H. Chiu, and R.-S. Chang, "Numerical simulation of a D-type optical fiber sensor based on the Kretchmann's configuration and heterodyne interferometry," *Sensors Actuators B Chem.*, vol. 114, no. 1, pp. 120–126, Mar. 2006.

[48] N. Cennamo, D. Massarotti, L. Conte, and L. Zeni, "Low Cost Sensors Based on SPR in a Plastic Optical Fiber for Biosensor Implementation," *Sensors*, vol. 11, no. 12, pp. 11752–11760, Dec. 2011.

[49] A. J. C. Tubb, F. P. Payne, R. B. Millington, and C. R. Lowe, "Single-mode optical fibre surface plasma wave chemical sensor," *Sensors Actuators B Chem.*, vol. 41, no. 1–3, pp. 71–79, Jun. 1997.

[50] D. Monzón-Hernández and J. Villatoro, "High-resolution refractive index sensing by means of a multiple-peak surface plasmon resonance optical fiber sensor," *Sensors Actuators B Chem.*, vol. 115, no. 1, pp. 227–231, May 2006.

[51] Ó. Esteban, F. B. Naranjo, N. Díaz-Herrera, S. Valdueza-Felip, M. C. Navarrete, and A. González-Cano, "High-sensitive SPR sensing with Indium Nitride as a dielectric overlay of optical fibers," *Sensors Actuators, B Chem.*, vol. 158, no. 1, pp. 372–376, 2011.

[52] M. Iga, A. Seki, and K. Watanabe, "Gold thickness dependence of SPR-based hetero-core structured optical fiber sensor," *Sensors Actuators B Chem.*, vol. 106, no. 1, pp. 363–368, Apr. 2005.

[53] M. Erdmanis, D. Viegas, M. Hautakorpi, S. Novotny, J. L. Santos, and H. Ludvigsen, "Comprehensive numerical analysis of a surface-plasmon-resonance sensor based on an H-shaped optical fiber," *Opt. Express*, vol. 19, no. 15, p. 13980, Jul. 2011.

[54] H. Suzuki, M. Sugimoto, Y. Matsui, and J. Kondoh, "Effects of gold film thickness on spectrum profile and sensitivity of a multimode-optical-fiber SPR sensor," *Sensors Actuators B Chem.*, vol. 132, no. 1, pp. 26–33, May 2008.

[55] A. Hassani and M. Skorobogatiy, "Design criteria for microstructured-optical-fiber-based surface-plasmon-resonance sensors," *J. Opt. Soc. Am. B*, vol. 24, no. 6, pp. 1423–1429, Jun. 2007.

[56] B.-H. Liu, Y.-X. Jiang, X.-S. Zhu, X.-L. Tang, and Y.-W. Shi, "Hollow fiber surface plasmon resonance sensor for the detection of liquid with high refractive index.," *Opt. Express*, vol. 21, no. 26, pp. 32349–57, 2013.

[57] J. Homola and M. Piliarik, "Surface Plasmon Resonance (SPR) Sensors," in *Surface Plasmon Resonance Based Sensors*, J. Homola, Ed. Berlin, Heidelberg: Springer Berlin Heidelberg, 2006, pp. 45–67.

[58] A. K. Sharma and B. D. Gupta, "Fibre-optic sensor based on surface plasmon resonance with Ag–Au alloy nanoparticle films," *Nanotechnology*, vol. 17, no. 1, pp. 124–131, Jan.

2006.
[59] M. Kanso, S. Cuenot, and G. Louarn, “Sensitivity of Optical Fiber Sensor Based on Surface Plasmon Resonance: Modeling and Experiments,” *Plasmonics*, vol. 3, no. 2–3, pp. 49–57, Sep. 2008.
[60] C. Ronot-Trioli, A. Trouillet, C. Veillas, and H. Gagnaire, “Monochromatic excitation of surface plasmon resonance in an optical-fibre refractive-index sensor,” *Sensors Actuators A Phys.*, vol. 54, no. 1–3, pp. 589–593, Jun. 1996.
[61] Y. S. Dwivedi, A. K. Sharma, and B. D. Gupta, “Influence of Design Parameters on the Performance of a Surface Plasmon Sensor Based Fiber Optic Sensor,” *Plasmonics*, vol. 3, no. 2–3, pp. 79–86, Sep. 2008.
[62] A. K. Sharma and B. D. Gupta, “Comparison of Performance Parameters of Conventional and Nano-plasmonic Fiber Optic Sensors,” *Plasmonics*, vol. 2, no. 2, pp. 51–54, Jun. 2007.
[63] A. K. Sharma and G. J. Mohr, “Theoretical understanding of an alternating dielectric multilayer-based fiber optic SPR sensor and its application to gas sensing,” *New J. Phys.*, vol. 10, no. 2, p. 23039, Feb. 2008.
[64] R. K. Verma, A. K. Sharma, and B. D. Gupta, “Surface plasmon resonance based tapered fiber optic sensor with different taper profiles,” *Opt. Commun.*, vol. 281, no. 6, pp. 1486–1491, Mar. 2008.
[65] R. K. Verma, A. K. Sharma, and B. D. Gupta, “Modeling of Tapered Fiber-Optic Surface Plasmon Resonance Sensor With Enhanced Sensitivity,” *IEEE Photonics Technol. Lett.*, vol. 19, no. 22, pp. 1786–1788, Nov. 2007.
[66] S.-F. Wang, M.-H. Chiu, J.-C. Hsu, R.-S. Chang, and F.-T. Wang, “Theoretical analysis and experimental evaluation of D-type optical fiber sensor with a thin gold film,” *Opt. Commun.*, vol. 253, no. 4–6, pp. 283–289, Sep. 2005.
[67] M. H. Chiu and C. H. Shih, “Searching for optimal sensitivity of single-mode D-type optical fiber sensor in the phase measurement,” *Sensors Actuators, B Chem.*, vol. 131, no. 2, pp. 596–601, May 2008.
[68] R. Slavík, J. Homola, J. Čtyroký, and E. Brynda, “Novel spectral fiber optic sensor based on surface plasmon resonance,” *Sensors Actuators B Chem.*, vol. 74, no. 1–3, pp. 106–111, Apr. 2001.
[69] R. Slavik, J. Homola, and J. Čtyroký, “Miniaturization of fiber optic surface plasmon resonance sensor,” *Sensors Actuators B Chem.*, vol. 51, no. 1–3, pp. 311–315, Aug. 1998.
[70] M. Piliarik, J. Homola, Z. Maníková, and J. Čtyroký, “Surface plasmon resonance sensor based on a single-mode polarization-maintaining optical fiber,” *Sensors Actuators, B Chem.*, vol. 90, no. 1–3, pp. 236–242, Apr. 2003.
[71] A. K. Sharma and B. D. Gupta, “On the performance of different bimetallic combinations in surface plasmon resonance based fiber optic sensors,” *J. Appl. Phys.*, vol. 101, no. 9, p. 93111, May 2007.
[72] J. Čtyroky□, J. Homola, and M. Skalsky□, “Tuning of spectral operation range of a waveguide surface plasmon resonance sensor,” *Electron. Lett.*, vol. 33, no. 14, p. 1246, 1997.
[73] I. T. Leite, P. Fernandes, A. Hierro-rodríguez, J. M. Teixeira, P. A. S. Jorge, and A. Guerreiro, “Analysis of a fibre-optic sensor design based on SPR in nanowire metamaterial films,” *23rd Int. Conf. Opt. Fibre Sensors*, vol. 9157, no. 4, pp. 1–4, 2014.
[74] N. Luan and J. Yao, “High Refractive Index Surface Plasmon Resonance Sensor Based on a Silver Wire Filled Hollow Fiber,” *IEEE Photonics J.*, vol. 8, no. 1, pp. 1–9, Feb. 2016.
[75] G. Nemova and R. Kashyap, “Theoretical model of a planar integrated refractive index sensor based on surface plasmon-polariton excitation,” *Opt. Commun.*, vol. 275, no. 1, pp. 76–82, Jul. 2007.
[76] Y. Y. Shevchenko and J. Albert, “Plasmon resonances in gold-coated tilted fiber Bragg gratings.,” *Opt. Lett.*, vol. 32, no. 3, pp. 211–213, 2007.
[77] A. Hassani and M. Skorobogatiy, “Surface plasmon resonance-like integrated sensor at terahertz frequencies for gaseous analytes,” *Opt. Express*, vol. 16, no. 25, p. 20206, Dec. 2008.
[78] R. Saikia *et al.*, “Fiber-Optic pH Sensor Based on SPR of Silver Nanostructured Film,” in *AIP Conference Proceedings*, 2009, vol. 1147, no. 1, pp. 249–255.
[79] C. R. Zamarreño, M. Hernáez, I. Del Villar, C. Fernandez-Valdivielso, F. J. Arregui, and

I. R. Matias, “Optical fiber pH sensor fabrication by means of indium tin oxide coated optical fiber refractometers,” *Phys. status solidi*, vol. 7, no. 11–12, pp. 2705–2707, Nov. 2010.

[80] S. K. Mishra and B. D. Gupta, “Surface plasmon resonance based fiber optic pH sensor utilizing Ag/ITO/Al/hydrogel layers,” *Analyst*, vol. 138, no. 9, p. 2640, Nov. 2013.

[81] K. F. Bohren and D. R. Huffman, *Absorption and Scattering of Light by Small Particles*. 2004.

[82] L. Novotny and B. Hecht, *Principles of Nano-Optics (second edition)*, Cambridge. Cambridge, 2012.

[83] J. F. Schenck, “The role of magnetic susceptibility in magnetic resonance imaging: MRI magnetic compatibility of the first and second kinds,” *Med. Phys.*, vol. 23, no. 6, p. 815, 1996.

[84] F. A. Hopf and G. I. Stegeman, *Applied classical electrodynamics*, vol. 1: Linear. Krieger Pub Co; Reprint edition, 1985.

[85] P. G. Etchegoin, E. C. Le Ru, and M. Meyer, “An analytic model for the optical properties of gold,” *J. Chem. Phys.*, vol. 125, no. 16, p. 164705, Oct. 2006.

[86] K. Oughstun and N. Cartwright, “On the Lorentz-Lorenz formula and the Lorentz model of dielectric dispersion: addendum,” *Opt. Express*, vol. 11, no. 21, pp. 2791–2, 2003.

[87] A. D. Rakić, A. B. Djurišić, J. M. Elazar, and M. L. Majewski, “Optical properties of metallic films for vertical-cavity optoelectronic devices,” *Appl. Opt.*, vol. 37, no. 22, pp. 5271–5283, Aug. 1998.

[88] J. W. Fleming, “Dispersion in GeO_2–SiO_2 glasses,” *Appl. Opt.*, vol. 23, no. 24, p. 4486, 1984.

[89] I. H. Malitson, F. V. J. Murphy, and W. S. Rodney, “Refractive index of synthetic sapphire,” *Josa*, vol. 48, no. 1, pp. 72–73, 1958.

[90] T. Ishigure, E. Nihei, and Y. Koike, “Optimum refractive-index profile of the graded-index polymer optical fiber, toward gigabit data links.,” *Appl. Opt.*, vol. 35, no. 12, pp. 2048–2053, Apr. 1996.

[91] P. B. Johnson and R. W. Christy, “Optical constants of the noble metals,” *Phys. Rev. B*, vol. 6, no. 12, pp. 4370–4379, 1972.

[92] A. W. Snyder and J. D. Love, *Optical Waveguide Theory*. Boston, MA: Springer US, 1984.

[93] N. Catarino, Diana, Viegas, “Sensing Devices Based on Micro-Optic Tecnology,” Faculdade de Ciências da Universidade do Porto, 2010.

[94] S. A. Maier, *Plasmonics: Fundamentals and Applications*, vol. 1, no. 8. Boston, MA: Springer US, 2007.

[95] H. Suzuki, M. Sugimoto, Y. Matsui, and J. Kondoh, “Effects of gold film thickness on spectrum profile and sensitivity of a multimode-optical-fiber SPR sensor,” *Sensors Actuators B Chem.*, vol. 132, no. 1, pp. 26–33, May 2008.

[96] R. K. Verma, A. K. Sharma, and B. D. Gupta, “Surface plasmon resonance based tapered fiber optic sensor with different taper profiles,” *Opt. Commun.*, vol. 281, no. 6, pp. 1486–1491, Mar. 2008.

[97] P. Uebel, M. a Schmidt, H. W. Lee, and P. S. J. Russell, “Polarisation-resolved near-field mapping of a coupled gold nanowire array,” *Opt. Express*, vol. 20, no. 27, p. 28409, Dec. 2012.

[98] J.-L. Tang, S.-F. Cheng, W.-T. Hsu, T.-Y. Chiang, and L.-K. Chau, “Fiber-optic biochemical sensing with a colloidal gold-modified long period fiber grating,” *Sensors Actuators B Chem.*, vol. 119, no. 1, pp. 105–109, Nov. 2006.

[99] I. T. Leite *et al.*, “Exciting the optical response of nanowire metamaterial films on the tip of optical fibres,” *Phys. status solidi - Rapid Res. Lett.*, vol. 7, no. 9, pp. 664–667, Sep. 2013.

[100] W. Q. Hu, E. J. Liang, P. Ding, G. W. Cai, and Q. Z. Xue, “Surface plasmon resonance and field enhancement in #-shaped gold wires metamaterial,” *Opt. Express*, vol. 17, no. 24, p. 21843, Nov. 2009.

[101] I. T. Leite *et al.*, “Ag-nanowire metamaterials: spectral reflectance analysis and homogenization models,” in *8th Iberoamerican Optics Meeting and 11th Latin American Meeting on Optics, Lasers, and Applications*, 2013, vol. 8785, p. 8785FL.

[102] M. A. Schmidt and P. S. Russell, “Long-range spiralling surface plasmon modes on metallic nanowires,” *Opt. Express*, vol. 16, no. 18, p. 13617, Sep. 2008.

[103] B. Shuai, L. Xia, Y. Zhang, and D. Liu, "A multi-core holey fiber based plasmonic sensor with large detection range and high linearity," *Opt. Express*, vol. 20, no. 6, pp. 5974–5986, Mar. 2012.

[104] H. W. Lee *et al.*, "Pressure-assisted melt-filling and optical characterization of Au nanowires in microstructured fibers," *Opt. Express*, vol. 19, no. 13, pp. 12180–12189, Jun. 2011.

[105] H. K. Tyagi *et al.*, "Plasmon resonances on gold nanowires directly drawn in a step-index fiber," *Opt. Lett.*, vol. 35, no. 15, pp. 2573–2575, Aug. 2010.

[106] C. Jain, A. Tuniz, K. Reuther, T. Wieduwilt, M. Rettenmayr, and M. A. Schmidt, "Micron-sized gold-nickel alloy wire integrated silica optical fibers," *Opt. Mater. Express*, vol. 6, no. 6, pp. 1790–1799, Jun. 2016.

[107] N. Luan, C. Ding, and J. Yao, "A Refractive Index and Temperature Sensor Based on Surface Plasmon Resonance in an Exposed-Core Microstructured Optical Fiber," *IEEE Photonics J.*, vol. 8, no. 2, pp. 1–8, Apr. 2016.

[108] R. Otupiri, E. K. Akowuah, and S. Haxha, "Multi-channel SPR biosensor based on PCF for multi-analyte sensing applications," *Opt. Express*, vol. 23, no. 12, pp. 15716–15727, Jun. 2015.

[109] N. Cennamo *et al.*, "Modal Filtering for Optimized Surface Plasmon Resonance Sensing in Multimode Plastic Optical Fibers," *IEEE Sens. J.*, vol. 15, no. 11, pp. 6306–6312, Nov. 2015.

[110] D. Felipe Santos, A. Guerreiro, and J. Manuel Baptista, "Simultaneous plasmonic measurement of refractive index and temperature based on a D-type fiber sensor with gold wires," *IEEE Sens. J.*, vol. 17, no. 8, pp. 1–1, Apr. 2017.

[111] M. Benounis, N. Jaffrezic-Renault, J. P. Dutasta, K. Cherif, and A. Abdelghani, "Study of a new evanescent wave optical fibre sensor for methane detection based on cryptophane molecules," *Sensors Actuators, B Chem.*, vol. 107, no. 1 SPEC. ISS., pp. 32–39, 2005.

[112] F. M. Araújo, L. a Ferreira, J. L. Santos, and F. Farahi, "Temperature and strain insensitive bending measurements with D-type fibre Bragg gratings," *Meas. Sci. Technol.*, vol. 12, no. 7, pp. 829–833, 2001.

[113] O. Frazao, P. Jorge, J. M. Baptista, and J. L. Santos, "Optical refractometer based on a Hi-Bi D-type fiber loop mirror," in *2008 IEEE Sensors*, 2008, pp. 957–960.

[114] M.-H. Chiu, S.-F. Wang, and R.-S. Chang, "D-type fiber biosensor based on surface-plasmon resonance technology and heterodyne interferometry," *Opt. Lett.*, vol. 30, no. 3, p. 233, Feb. 2005.

[115] J. Homola, H. B. Lu, G. G. Nenninger, J. Dostálek, and S. S. Yee, "A novel multichannel surface plasmon resonance biosensor," *Sensors and Actuators, B: Chemical*, vol. 76, no. 1–3. pp. 403–410, Jun-2001.

[116] P. Uebel, "Metal filled optical fibers - photonics and plasmonics on the nanoscale," Friedrich-Alexander-Universität Erlangen-Nürnberg Metal, 2013.

[117] D. Christensen and D. Fowers, "Modeling SPR sensors with the finite-difference time-domain method," *Biosens. Bioelectron.*, vol. 11, no. 6–7, pp. 677–684, 1996.

[118] T. a Birks, J. C. Knight, and P. S. J. Russell, "Endlessly single-mode photonic crystal fiber," *Opt. Lett.*, vol. 22, no. 13, p. 961, 1997.

[119] S. M. Kuo, Y. W. Huang, S. M. Yeh, W. H. Cheng, and C. H. Lin, "Liquid crystal modified photonic crystal fiber (LC-PCF) fabricated with an SU-8 photoresist sealing technique for electrical flux measurement," *Proc. IEEE Int. Conf. Micro Electro Mech. Syst.*, vol. 19, no. 19, pp. 803–806, Sep. 2010.

[120] S.-J. Park *et al.*, "Nanosilver Colloids-Filled Photonic Crystal Arrays for Photoluminescence Enhancement," *Nanoscale Res. Lett.*, vol. 5, no. 10, pp. 1590–1595, Oct. 2010.

[121] Y. Lu *et al.*, "Grapefruit Fiber Filled with Silver Nanowires Surface Plasmon Resonance Sensor in Aqueous Environments," *Sensors*, vol. 12, no. 12, pp. 12016–12025, Aug. 2012.

[122] N. Luan, R. Wang, W. Lv, and J. Yao, "Surface plasmon resonance sensor based on D-shaped microstructured optical fiber with hollow core," *Opt. Express*, vol. 23, no. 7, p. 8576, Apr. 2015.

[123] J. Homola, "Present and future of surface plasmon resonance biosensors," *Anal. Bioanal. Chem.*, vol. 377, no. 3, pp. 528–539, Oct. 2003.

[124] H.-Y. Lin, W.-H. Tsai, Y.-C. Tsao, and B.-C. Sheu, "Side-polished multimode fiber biosensor based on surface plasmon resonance with halogen light," *Appl. Opt.*, vol. 46, no. 5, p. 800, Feb. 2007.
[125] N. Cennamo, L. Coelho, A. Guerreiro, P. A. S. Jorge, and L. Zeni, "SPR sensors in POF: a new experimental configuration for extended refractive index range and better SNR," in *23rd International Conference on Optical Fibre Sensors*, 2014, vol. 9157, p. 915759.
[126] J. Homola, S. S. Yee, and G. Gauglitz, "Surface plasmon resonance sensors: review," *Sensors Actuators B Chem.*, vol. 54, no. 1–2, pp. 3–15, Jan. 1999.
[127] E. Fontana, "A novel gold-coated multimode fiber sensor," *IEEE Trans. Microw. Theory Tech.*, vol. 50, no. 1, pp. 82–87, 2002.
[128] R. Jha, R. K. Verma, and B. D. Gupta, "Surface Plasmon Resonance-Based Tapered Fiber Optic Sensor: Sensitivity Enhancement by Introducing a Teflon Layer Between Core and Metal Layer," *Plasmonics*, vol. 3, no. 4, pp. 151–156, Dec. 2008.
[129] V. M. Muñoz-Berti *et al.*, "Low cost plastic optical fiber sensor based on surface plasmon resonance," in *Fourth European Workshop on Optical Fibre Sensors*, 2010, vol. 7653, p. 765327.
[130] Y. Jin and A. M Granville, "Polymer Fiber Optic Sensors – A Mini Review of their Synthesis and Applications," *J. Biosens. Bioelectron.*, vol. 7, no. 1, pp. 1–11, 2016.
[131] R. Galatus, N. Cennamo, and E. Voiculescu, "Optimal Design of D-Type Plastic Fibers for Best Sensitivity of SPR Sensors," *Adv. Eng. Forum*, vol. 8–9, pp. 563–573, Jun. 2013.
[132] N. Cennamo and L. Zeni, "Bio and Chemical Sensors Based on Surface Plasmon Resonance in a Plastic Optical Fiber," in *Optical sensors - New developments and practical applications*, InTech, 2014, pp. 119–140.
[133] N. Cennamo, G. D'Agostino, R. Galatus, L. Bibbò, M. Pesavento, and L. Zeni, "Sensors based on surface plasmon resonance in a plastic optical fiber for the detection of trinitrotoluene," *Sensors Actuators B Chem.*, vol. 188, pp. 221–226, Nov. 2013.
[134] A. M. Shrivastav, S. K. Mishra, and B. D. Gupta, "Fiber optic SPR sensor for the detection of melamine using molecular imprinting," *Sensors Actuators B Chem.*, vol. 212, pp. 404–410, Jun. 2015.
[135] N. Cennamo, L. De Maria, G. D'Agostino, L. Zeni, and M. Pesavento, "Monitoring of Low Levels of Furfural in Power Transformer Oil with a Sensor System Based on a POF-MIP Platform," *Sensors*, vol. 15, no. 4, pp. 8499–8511, Apr. 2015.
[136] R. S. Kshetrimayum, "A brief intro to metamaterials," *IEEE Potentials*, vol. 23, no. 5, pp. 44–46, 2004.
[137] D. F. Santos, A. Guerreiro, and J. M. Baptista, "SPR optimization using metamaterials in a D-type PCF refractive index sensor," *Opt. Fiber Technol.*, vol. 33, pp. 83–88, Jan. 2017.
[138] W. Cai and V. Shalaev, *Optical Metamaterials*, Springer., vol. 10, no. 6011. New York, NY: Springer New York, 2010.
[139] K.-S. Lee, J. M. Son, D.-Y. Jeong, T. S. Lee, and W. M. Kim, "Resolution Enhancement in Surface Plasmon Resonance Sensor Based on Waveguide Coupled Mode by Combining a Bimetallic Approach," *Sensors*, vol. 10, no. 12, pp. 11390–11399, Dec. 2010.
[140] P. R. West, S. Ishii, G. V. Naik, N. K. Emani, V. M. Shalaev, and A. Boltasseva, "Searching for better plasmonic materials," *Laser Photon. Rev.*, vol. 4, no. 6, pp. 795–808, Nov. 2010.
[141] C. a. Pfeiffer, E. N. Economou, and K. L. Ngai, "Surface polaritons in a circularly cylindrical inferface: Surface plasmons," *Phys. Rev. B*, vol. 10, no. 8, pp. 3038–3051, 1974.
[142] N. Luan and J. Yao, "Surface Plasmon Resonance Sensor Based On Exposed-Core Microstructured Optical Fiber Placed With A Silver Wire," *IEEE Photonics J.*, vol. 8, no. 1, pp. 1–8, Feb. 2016.
[143] J. Dostálek *et al.*, "Surface plasmon resonance biosensor based on integrated optical waveguide," *Sensors Actuators B Chem.*, vol. 76, no. 1–3, pp. 8–12, Jun. 2001.
[144] P. Mao *et al.*, "Design and optimization of surface plasmon resonance sensor based on multimode fiber," *Opt. Quantum Electron.*, vol. 47, no. 6, pp. 1495–1502, Jun. 2015.
[145] L. Coelho, J. M. M. M. de Almeida, J. L. Santos, R. A. S. Ferreira, P. S. André, and D. Viegas, "Sensing Structure Based on Surface Plasmon Resonance in Chemically Etched Single Mode Optical Fibres," *Plasmonics*, vol. 10, no. 2, pp. 319–327, Apr. 2015.

[146] G. An, S. Li, W. Qin, W. Zhang, Z. Fan, and Y. Bao, "High-Sensitivity Refractive Index Sensor Based on D-Shaped Photonic Crystal Fiber with Rectangular Lattice and Nanoscale Gold Film," *Plasmonics*, vol. 9, no. 6, pp. 1355–1360, Dec. 2014.

[147] A. Belahmar and A. Chouiyakh, "Investigation of Surface Plasmon Resonance and Optical Band Gap Energy in Gold / Silica Composite Films Prepared by RF-Sputtering," *Nanosci. Technol.*, vol. 2, no. 2, pp. 81–84, 2016.

[148] Y. Zhao, Z.-Q. Deng, and H.-F. Hu, "Fiber-Optic SPR Sensor for Temperature Measurement," *IEEE Trans. Instrum. Meas.*, vol. 64, no. 11, pp. 3099–3104, Nov. 2015.

[149] T. Hu, Y. Zhao, and A. ning Song, "Fiber optic SPR sensor for refractive index and temperature measurement based on MMF-FBG-MMF structure," *Sensors Actuators, B Chem.*, vol. 237, pp. 521–525, 2016.

[150] C. Gouveia, G. Chesini, C. M. B. Cordeiro, J. M. Baptista, and P. A. S. Jorge, "Simultaneous measurement of refractive index and temperature using multimode interference inside a high birefringence fiber loop mirror," *Sensors Actuators B Chem.*, vol. 177, pp. 717–723, Feb. 2013.

[151] A. K. Sharma and B. D. Gupta, "Influence of temperature on the sensitivity and signal-to-noise ratio of a fiber-optic surface-plasmon resonance sensor," *Appl. Opt.*, vol. 45, no. 1, pp. 151–161, Jan. 2006.

[152] A. Alabastri *et al.*, "Molding of Plasmonic Resonances in Metallic Nanostructures: Dependence of the Non-Linear Electric Permittivity on System Size and Temperature," *Materials (Basel).*, vol. 6, no. 11, pp. 4879–4910, Oct. 2013.

[153] J. Homola and M. Piliarik, "Surface Plasmon Resonance (SPR) Sensors," in *Springer Ser Chem Sens Biosens*, vol. 4, 2006, pp. 45–67.

[154] T. Srivastava, R. Das, and R. Jha, "Highly Sensitive Plasmonic Temperature Sensor Based on Photonic Crystal Surface Plasmon Waveguide," *Plasmonics*, vol. 8, no. 2, pp. 515–521, Jun. 2013.

[155] Feng Xiao, D. Michel, Guangyuan Li, Anshi Xu, and K. Alameh, "Simultaneous Measurement of Refractive Index and Temperature Based on Surface Plasmon Resonance Sensors," *J. Light. Technol.*, vol. 32, no. 21, pp. 4169–4173, Nov. 2014.